Desert dust exerts a substantial longwave radiative forcing missing from climate models

Jasper F. Kok[1,*], Ashok. K. Gupta[1], Amato T. Evan[2], Adeyemi A. Adebiyi[3], Samuel Albani[4], Yves Balkanski[5], Ramiro Checa-Garcia[6], Peter R. Colarco[7], Douglas Hamilton[8], Yue Huang[1], Akinori Ito[9], Martina Klose[10], Longlei Li[11], Natalie M. Mahowald[11], Ron L. Miller[12], Vincenzo Obiso[13], Carlos Pérez García-Pando[13,14], Adriana Rocha Lima[15], Jessica Wan[2]

[1]Department of Atmospheric and Oceanic Sciences, University of California, Los Angeles, CA 90095, USA
[2]Scripps Institution of Oceanography, University of California, San Diego, CA 92093
[3]Department of Life and Environmental Sciences, University of California, Merced, CA, 95344, USA
[4]Department of Environmental and Earth Sciences, University of Milano-Bicocca, Milano, Italy
[5]Laboratoire des Sciences du Climat et de l'Environnement, CEA-CNRS-UVSQ-UPSaclay, Gif-sur-Yvette, France
[6]Royal Netherlands Meteorological Institute, De Bilt, the Netherlands
[7]Atmospheric Chemistry and Dynamics Laboratory, NASA Goddard Space Flight Center, Greenbelt, MD 20771, USA
[8]Marine, Earth, and Atmospheric Science, North Carolina State University, Raleigh, NC, 27606
[9]Yokohama Institute for Earth Sciences, JAMSTEC, Yokohama, Kanagawa 236-0001, Japan
[10]Institute of Meteorology and Climate Research Troposphere Research, Karlsruhe Institute of Technology (KIT), Karlsruhe, Germany
[11]Department of Earth and Atmospheric Sciences, Cornell University, Ithaca, NY, 14850, USA.
[12]NASA Goddard Institute for Space Studies, New York NY10025 USA
[13]Barcelona Supercomputing Center (BSC), 08034 Barcelona, Spain
[14]ICREA, Catalan Institution for Research and Advanced Studies, 08010 Barcelona, Spain
[15]Department of Physics, University of Maryland, Baltimore County, 1000 Hilltop Circle, Baltimore, MD, 21250, USA
[*]Corresponding author: jfkok@ucla.edu

This paper has been submitted to Nature Climate Change.

Abstract

Historical increases in desert dust have affected climate by perturbing Earth's energy balance, including through interactions with longwave radiation that remain poorly quantified. Here, we use a data-driven analytical model to estimate the global dust longwave direct radiative effect (DRE). Our results align with observational estimates of longwave radiative effects, constraining the present-day global longwave DRE to +0.25 ± 0.06 Wm^{-2} (90% confidence interval). Climate models underestimate the longwave DRE by approximately a factor of two because they underestimate super coarse dust and neglect dust scattering of longwave radiation. We also show that increased dust since preindustrial times generated a positive longwave direct radiative forcing peaking at +0.14 ± 0.07 Wm^{-2} in the 1980s, modestly enhancing greenhouse warming. Because this warming is largely missing from current climate models, incorporating it could reduce biases in net aerosol forcing, refine climate sensitivity estimates, and improve projections of future climate change.

Introduction

Atmospheric dust levels have increased substantially since pre-industrial times[1-3]. Indeed, a recent reconstruction based on ice core records and other sedimentary archives estimated that global dust loading is now 55 ± 30 % higher than in pre-industrial times[4]. This raises the possibility that dust has exerted a substantial radiative forcing on the climate system, either amplifying or offsetting greenhouse warming depending on its net effect on Earth's energy budget. However, current climate models do not capture this historical increase in dust[4], and thus the associated radiative forcing is missing from projections of future climate change and estimates of climate sensitivity[5,6]. Accurately quantifying dust's radiative forcing is therefore essential to improve climate models and enhance the reliability of climate change projections.

One especially poorly constrained component of dust radiative forcing is due to changes in the heating effect that dust exerts by scattering and absorbing longwave (LW) radiation emitted from the lower atmosphere and the surface[7-11]. Dust itself normally emits LW radiation to space at a lower brightness temperature because it is situated higher in the atmosphere, causing net radiative cooling of the atmosphere and net heating at the surface and the top-of-atmosphere (TOA). These effects are most important for radiation with wavelengths in the "atmospheric window" around 8 - 14 μm in which a cloud-free atmosphere is relatively transparent. Outside of this window, the atmosphere is opaque to radiation due to absorption by water vapor and other greenhouse gases, such that the addition of another source of extinction has a negligible effect on the TOA spectral flux[12].

Climate model calculations of the resulting perturbation to Earth's energy balance - the LW direct radiative effect (DRE) - range between approximately 0.1 to 0.25 Wm^{-2} [7,8] (Table S1). This large uncertainty is a consequence of substantial biases and uncertainties in model simulations, including in the LW optical properties[13], size distribution[14], and altitude[15,16] of dust. In addition, most radiative transfer schemes used in global climate models do not account for the scattering of LW radiation[12,17], which previous work suggests accounts for approximately half of the total LW DRE[7,12,18]. Moreover, many models underestimate, or even omit, the contribution of super coarse dust (with diameter $D > 10$ μm), which might account for up to a third of the LW DRE[19]. It is therefore likely that climate models underestimate the LW DRE[7,9,12].

Current climate models are thus poorly suited to determine the radiative forcing from changes in the LW DRE of dust since pre-industrial times. This is because they inadequately represent the LW DRE and fail to capture the historical increase in desert dust. Here, we first quantify the dust LW DRE using a data-driven analytical model that accounts for LW scattering and integrates observational constraints on dust optical properties, abundance (including super coarse dust), and longwave radiative effects. This observationally constrained approach substantially reduces the uncertainty relative to climate model results (Table S1), yielding a global mean LW DRE at TOA of 0.25 ± 0.06 W/m^2 (90% confidence interval). By combining this result with the historical increase in dust[4], we obtain the corresponding dust LW direct radiative forcing (DRF), which we find peaked at $+0.14 \pm 0.07$ Wm^{-2} in the 1980s, and which has therefore slightly enhanced greenhouse warming.

Data-driven analytical model of dust longwave direct radiative effects. In developing an analytical model for the dust LW DRE and DRF, we considered the key factors influencing the TOA LW DRE, as detailed below (also see Methods and Extended Data Fig. 1). First, the LW DRE depends in a near-linear fashion on the atmospheric abundance of dust[18], which is most strongly constrained by remote sensing data of dust aerosol optical depth (DAOD) in the shortwave (SW) spectrum[20]. Second, the LW DRE depends on the highly uncertain[13] optical properties (mass extinction efficiency, single-scattering albedo, and asymmetry parameter) of dust in the LW spectrum. Third, the LW DRE depends on the dust size distribution because coarse dust (diameter $2.5 < D < 10$ μm) and super coarse dust likely contribute over 80% of the LW DAOD[10,19] (Table S2). Fourth, the dust LW DRE generally increases with the height of the dust layer[18,21]. This is because higher dust layers are generally colder than the surface, so when they absorbs and emit longwave radiation, they emit at a lower temperature than the surface would. This reduces outgoing radiation to space, thereby enhancing the dust LW DRE. Fifth, the dust LW DRE decreases with the absorptivity in the atmospheric window between the dust layer and the surface, as stronger atmospheric absorption reduces the LW radiative flux received by the dust layer. Finally, the dust LW DRE also decreases with the atmospheric absorptivity above the dust layer because absorption or downward scattering of upwelling LW radiation by dust will have no influence on the TOA energy budget if that upwelling LW radiation would have been absorbed by overlying greenhouse gases or clouds anyways. As such, optically thick clouds (i.e., with LW optical depth >> 1) overlying a dust layer essentially eliminate the dust LW DRE, whereas clouds below a dust layer only slightly reduce the LW DRE[12,18].

To adequately account for all these factors that determine the LW DRE, and thus the DRF, we use a data-driven analytical model (Fig. S1) that quantifies the effect of dust on the TOA LW radiative flux in the absence of clouds (clear sky). We drive this model with atmospheric and surface properties from reanalysis meteorology[22], the dust refractive index sampled from various observational studies[13], and joint observational-modeling constraints of the properties and abundance of dust with diameters up to 100 μm from the DustCOMM data set[23]. We propagate the various experimental, observational, and modeling uncertainties in these data sets through a bootstrap procedure, which yields many realizations (1,000) of the LW DRE. We then apply observational estimates of the top-of-atmosphere LW DRE per unit of shortwave (~550 nm) optical depth in clear-sky conditions[21,24] - the LW DRE efficiency (DREE) - to eliminate the subset (~half) of bootstrap simulations that are statistically inconsistent with these observations. The closure we thus achieve between the "bottom-up" calculation of the LW DRE by the analytical model and the "top-down" constraints from in situ and satellite data (Extended Data Fig. 2) provides confidence in our results.

The spatiotemporal pattern of the LW direct radiative effect efficiency (DREE). We find that our analytical model can reproduce, within the uncertainties, the spatiotemporal pattern of satellite observations of the LW DREE (Figs. 1, 2a). Both model and satellite observations indicate that the LW DREE is largest in summer, when the temperature difference between the surface and the dust layer is greatest (Fig. S2), in part because of high surface temperatures and in part because stronger convection carries dust to higher altitudes (Fig. S3). We further find that the LW DREE is higher close to source regions, where the particle size distribution is coarsest, resulting in greater LW radiative effects per unit SW DAOD (Table S2). The LW DREE generally decreases away from source regions, because temperatures over oceans and forests are more moderate than over deserts and because dust becomes finer during transport as coarse particles are preferentially removed by gravitational settling[19].

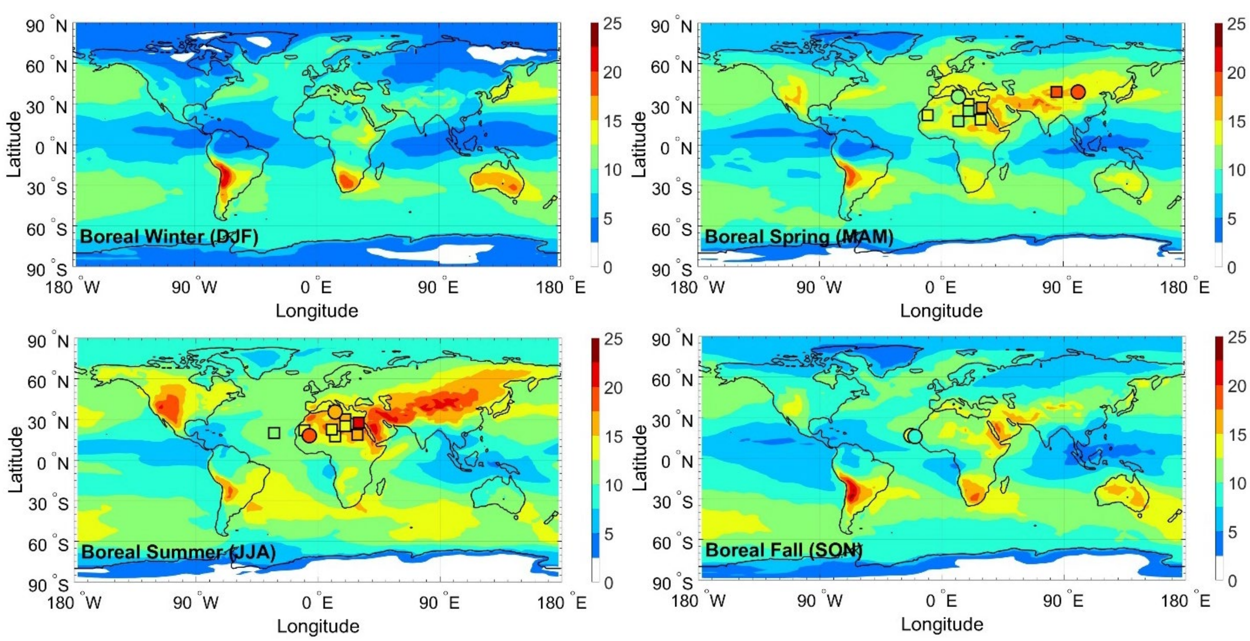

Fig. 1: The spatial and seasonal patterns of the top-of-atmosphere clear-sky longwave (LW) direct radiative effect efficiency (DREE). The predictions of a data-driven analytical model largely match the magnitude and variability of observational estimates (units of $\mathrm{Wm^{-2}}\tau_{SW}^{-1}$) based primarily on in-situ measurements (colored circles) and satellite data (colored squares). Both the data-driven model and the

observations indicate a range of the clear-sky LW DREE of approximately 5 to 20 $Wm^{-2}\tau_{SW}^{-1}$. The LW DREE is largest close to dust source regions (primarily deserts), where the dust size distribution is coarsest, and in summer and spring, when the surface is warmest and the dust is at greatest altitude because of stronger convection. The data used in all panels represents the diurnally and seasonally averaged LW DREE (see Methods).

The analytical model shows substantially better agreement against LW DREE observations than six different global model simulations. Indeed, the analytical model largely matches the magnitude of the LW DREE observations (bias of -1.0 Wm^2), explains approximately half of the variance in the observations ($R^2 = 45\%$), and is statistically consistent with those observations (reduced chi square value of $\chi_\nu^2 = 0.59$) (Fig. 2a). In contrast, global model simulations underestimate the LW DREE by approximately a factor of 2 and explain on average less than a quarter of the variance in observations (Fig. 2b, Table S3).

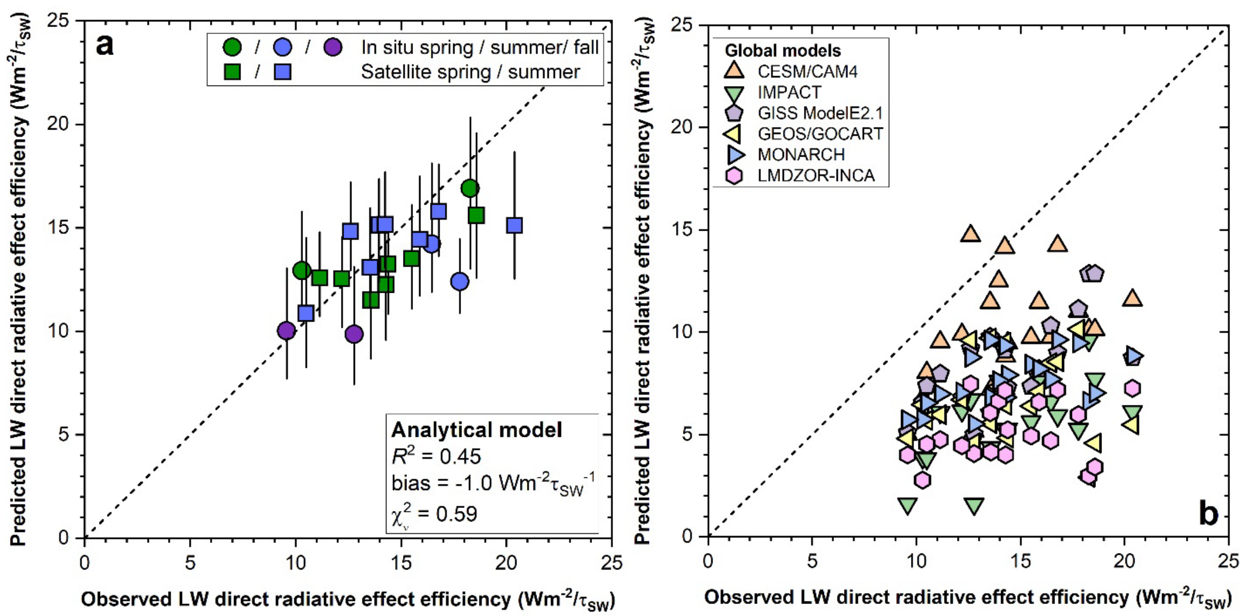

Fig. 2: Comparison between model predictions and observational estimates of clear-sky longwave (LW) direct radiative effect efficiency (DREE). (**a**) The data-driven analytical model reproduces both the magnitude (bias = -1.0 $\mathrm{Wm}^{-2}\tau_{SW}^{-1}$) and the seasonal and spatial variability (R^2 = 0.45) of observational estimates, agreeing with most observational estimates within the uncertainties (reduced chi squared $\chi_\nu^2 = 0.85$). (**b**) In contrast, global model simulations substantially underestimate the LW DREE observations, with a bias of -4 to -9 $\mathrm{Wm}^{-2}\tau_{SW}^{-1}$ (Table S3). This low bias likely occurs because models neglect LW scattering and underestimate super coarse dust. Horizontal error bars are not shown to avoid cluttering the figure but are assumed to equal 2 $\mathrm{Wm}^{-2}\tau_{SW}^{-1}$ (see Methods). The data shown represents the diurnally and seasonally averaged LW DREE (see Methods).

Observationally constrained annual global mean LW DRE. We obtained the global and annual mean clear-sky LW DRE at TOA by integrating over space and time. We find that the clear-sky LW DRE equals 0.32 ± 0.08 Wm^{-2} (90% CI), which is consistent with recent radiative transfer modeling results[25]. Given that the dust SW DAOD is 0.03 ± 0.01[19,20,23,26], this result implies a global mean clear-sky LW DRE per unit SW DAOD of 11 ± 5 Wm^{-2}.

We converted the clear-sky to the all-sky LW DRE, which is more relevant to Earth's energy balance and climate, by using an ensemble of global model simulations of the ratio of the all-sky to the clear-sky LW DRE (see Methods and Figs. S1, S4). We find that the annual mean all-sky LW DRE (Fig. 3a) is of the order of several Wm^{-2} close to the dust source regions, where LW DAOD (Fig. 3b) is largest. Because arid source regions have low cloud cover, the annually averaged reduction of the TOA LW DRE by clouds is modest (~10-20%) near most source regions, but larger (~40-60%) for dust transported far from source regions (e.g., over oceans), where cloud cover is usually higher (Fig. 3c). This anti-correlation of dust and cloud cover causes the reduction of dust LW radiative effects by clouds to be substantially smaller than the factor of ~2 reduction in the SW radiative effect of most other aerosol species[27]. Indeed, accounting for the effects of clouds on the LW DRE at TOA reduces the global DRE by ~20%, yielding an all-sky LW DRE of 0.25 ± 0.06 Wm^{-2} (Fig. 4a).

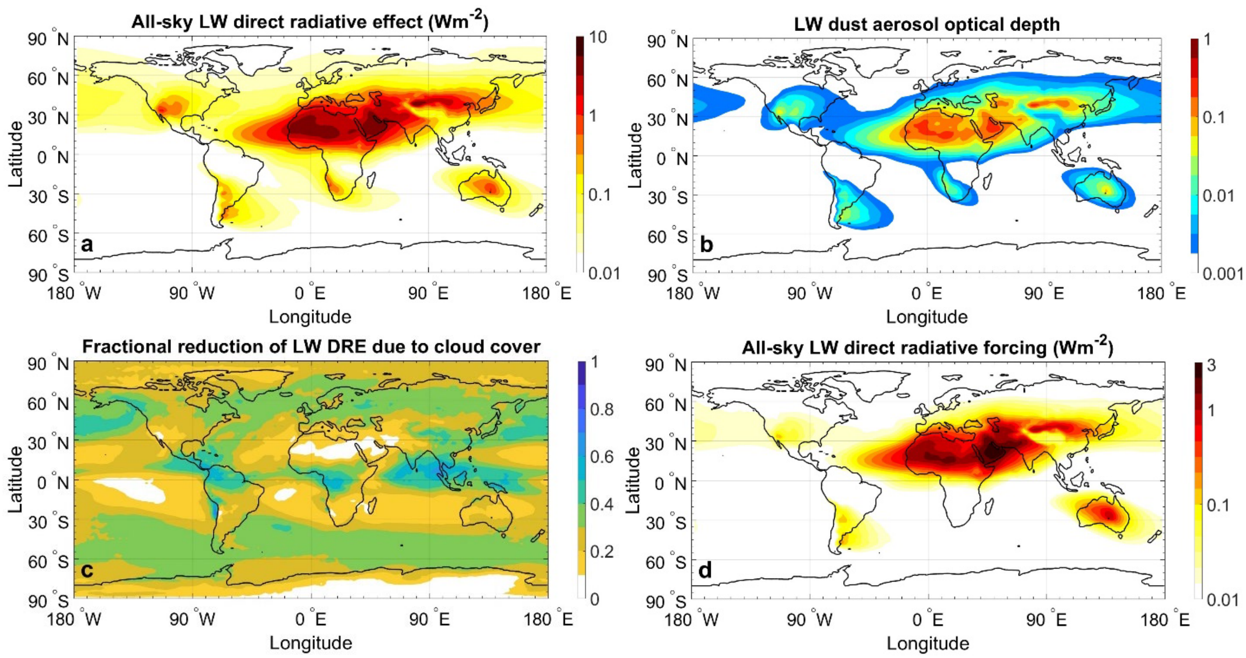

Fig. 3: Spatial pattern of LW direct radiative effects and forcing. The top-of-atmosphere (TOA) LW direct radiative effect (DRE) for all-sky conditions (**a**) is driven by extinction of LW radiation, as quantified by the annually averaged LW dust aerosol optical depth (DAOD) (**b**). The LW DRE is mitigated by the effects of clouds (**c**). Because of the historical increase in dust[4], the LW DRE has increased as well, generating a direct radiative forcing in the modern climate (1981-2000) relative to the pre-industrial climate (1851-1870) of several Wm^{-2} close to major source regions (**d**). The LW DRE, DAOD, and DRF were obtained from our data-driven analytical model (see Methods) and the fractional reduction of the LW DRE by clouds was obtained from an ensemble of global model simulations (see

Methods and Fig. S4). All panels represent annually averaged results; seasonally averaged results are shown in Figs. S9 and S10.

Why global models underestimate the LW DRE. A compilation of 22 global model results shows an all-sky LW DRE of 0.13 (90% confidence interval: 0.09 to 0.22) Wm^{-2} (Table S1). Global models thus underestimate the global mean LW DRE by approximately a factor of two (Fig. 4a), in addition to inadequately capturing the spatiotemporal variability of LW direct radiative effects (Fig. 2b and Table S3).

A critical contributor to this poor performance is that most global models neglect the effects of LW scattering, which is not included in most radiative transfer schemes used in global models[28]. This omission is problematic because scattering accounts for approximately half of the LW DAOD [51% (16 to 60%)] and an even larger fraction of the LW DRE [57 (21 to 66) %] (Fig. 4a). Scattering is thus somewhat more effective than absorption in generating a top-of-atmosphere radiative effect; indeed, we find that the global LW DREs generated per unit LW DAOD due to scattering and due to absorption are 33 ± 7 and 26 ± 7 $Wm^{-2}\tau_{LW}^{-1}$, respectively (Fig. S5). This larger efficiency of scattering in reducing the outgoing longwave radiation (OLR) occurs because 28 ± 3 % of scattering interactions result in down-scattering (Fig. S6), which reduces OLR. In contrast, because a material's absorptivity scales both its absorption and its emission of LW radiation, per Kirchhoff's law, the effect of dust absorption of LW radiation is tempered by co-occurring emission of LW radiation, albeit at a lower temperature.

Another factor that likely contributes to model underestimation of the LW DRE is the underestimation of coarse and super coarse dust[7,9,14]. The ability of dust to interact with LW radiation in the atmospheric window generally increases with particle diameter[29], with coarse ($2.5 \leq D < 10$ μm) and super coarse ($D \geq 10$ μm) dust respectively accounting for approximately 60 and 25% of the LW extinction[19] (Table S2). Correspondingly, a large fraction of the LW DRE is produced by coarse (~65%) and super coarse (~20%) dust (Fig. 4a and Table S2). However, many models substantially underestimate the concentration of coarse and (especially) super coarse dust[14,30,31], with many models even omitting super coarse dust[23], contributing to the model underestimation of the LW DRE (Fig. 4a).

Addressing the model biases in the dust LW DRE thus requires remedying the underestimation of super coarse dust[14] and accounting for the scattering of LW radiation[12]. This former problem can be partially addressed by implementing recent parameterizations that account for the observation that the emission flux of super coarse dust is much greater than most models simulate[30,32-34]. However, models also appear to underestimate the lifetime of super coarse dust, such that improved descriptions of the effects of turbulence[35], dust asphericity[36], dust orientation[37], and small-scale convection[38] on dust settling might be needed to better account for the observed prevalence of super coarse dust further from source regions[19].

Models also need to account for the contribution of scattering to the LW DRE. Some previous modeling studies have tried to do so by simply scaling up the radiative effect due to LW absorption[7-9,17]. However, this approach neglects the spatiotemporal variability of the fractional contribution of scattering to the LW DRE (Fig. S7). This variability arises primarily because the radiative perturbation from LW absorption depends strongly on the temperature contrast between the dust layer and the surface: absorbed radiation is re-emitted at the dust layer's colder temperature rather than the warmer surface temperature, leading to a net reduction in outgoing longwave radiation. In contrast, the radiative effect from LW scattering is largely independent of temperature contrast and thus of dust layer altitude. Consequently, the relative contribution of LW scattering to the LW DREE and thus the DRE (Fig. S7) is greater when the temperature difference between dust and the surface is smaller (Fig. S2), which typically occurs when dust is lower in the atmosphere (Fig. S3). This causes LW scattering to make a greater contribution to the LW DREE in winter than in summer and close to source regions than far from source regions (Fig. S7).

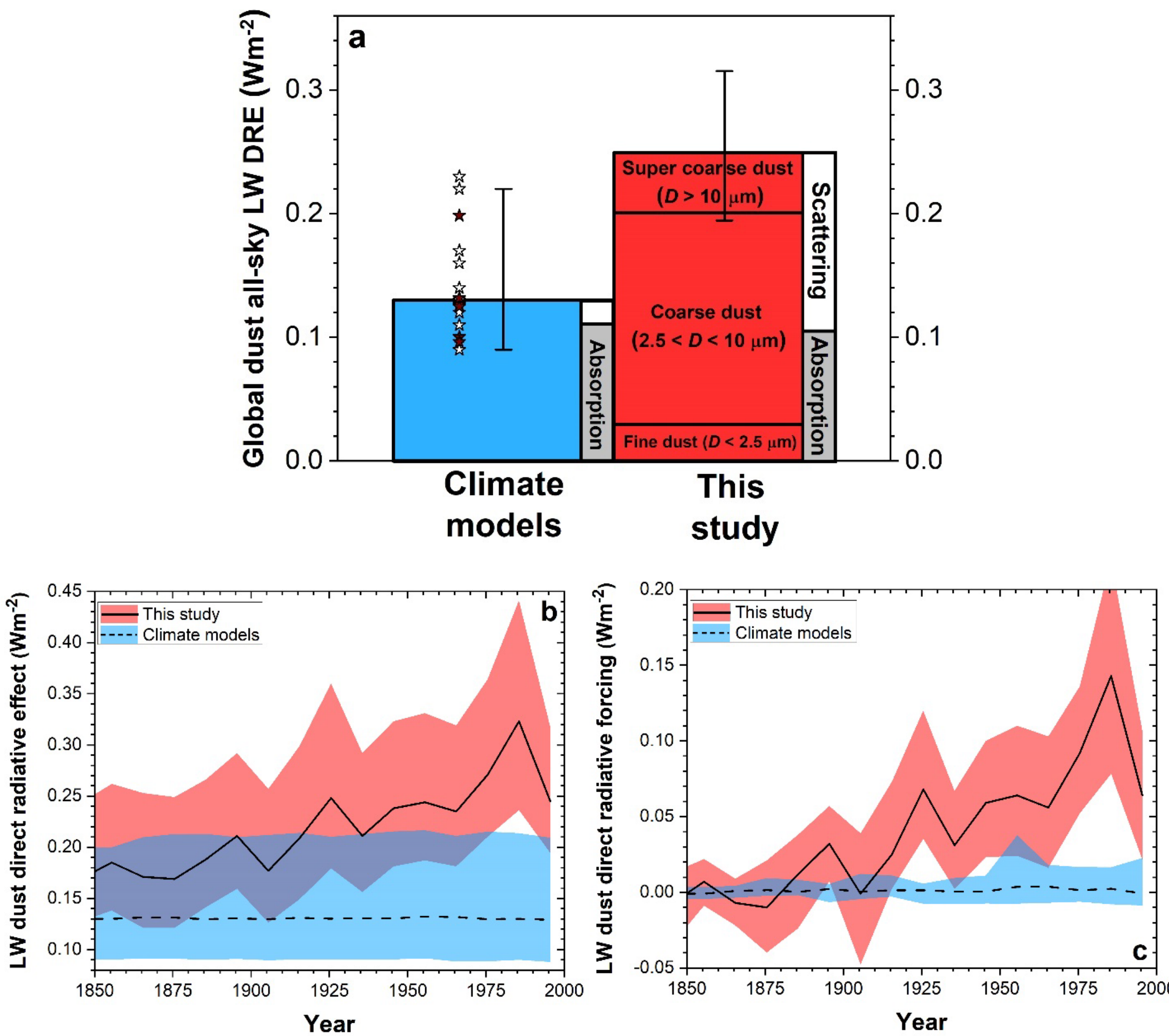

Fig. 4. Climate models underestimate the global mean direct radiative effect (DRE) and direct radiative forcing (DRF) due to dust interactions with longwave (LW) radiation. (**a**) A compilation of climate model results shows a global all-sky LW DRE at top-of-atmosphere (TOA) of 0.13 (0.09 – 0.22) Wm^{-2}, which is almost entirely due to LW absorption (grey vertical box) with a minor contribution from

LW scattering (small white vertical box; Table S2). In contrast, our data-driven analytical model constrains the all-sky LW DRE to almost double that value, 0.25 ± 0.06 Wm^{-2}, more than half of which is generated by LW scattering interactions. These interactions are omitted by most global models, which contributes to the underestimation by a factor of approximately 2 by those models. Additionally, the majority of the LW DRE is generated by coarse and super coarse dust, which is underestimated by global models[14]. (**b**) The time evolution of the all-sky LW DRE as simulated by climate models (dashed line) and calculated by the analytical model (solid line). (**c**) The time evolution of the LW direct radiative forcing (DRF) obtained by the analytical model (solid line). Because climate models underestimate both the LW DRE and the historical increase in desert dust[4], these models predict close-to-zero radiative forcing from changes in dust interactions with LW radiation (solid line). Filled brown stars in panel (a) denote global model results in the DustCOMM ensemble (see Fig. 2b and Table S1) and open stars denote published model results. The error bars in panel (a) and the shading in panels (b) and (c) represent 90% confidence ranges. The time evolution of the LW DRE was obtained by combining the LW DRE in (a) with a reconstruction of the atmospheric dust loading from sedimentary records and from the historical runs of 12 CMIP6 models with mechanistic dust cycles[4].

Despite this difference in the spatiotemporal pattern of the radiative effects of LW absorption and scattering, we find that neglecting LW scattering by global models causes only modest errors in the spatiotemporal pattern of the dust LW DREE (Fig. S8). As such, a simple approach to approximately account for the effects of LW scattering on the TOA energy budget is to use a mass extinction efficiency reflecting the contributions of both scattering and absorption, but to set the LW single-scattering albedo to zero for perfectly absorbing particles[17]. Doing so degrades agreement against LW DREE observations but yields a central estimate for the LW DRE of 0.22 Wm^{-2} (Fig. S8), which is close to our constraint. However, whereas LW absorption can substantially affect atmospheric dynamics and stability by producing atmospheric radiative cooling, scattering does not[12]. As such, it is preferable to represent dust LW scattering in radiative transfer schemes used in regional and global models, perhaps based on machine learning to reduce computational costs[39].

Implications for aerosol radiative forcing and climate change. We reconstruct the evolution of the LW DRE since pre-industrial times by combining the modern-climate LW DREE obtained here (Fig. 1) with the evolution of spatially resolved DAOD obtained in our previous work[4,40] (Fig. 4b). We find that the LW DRE increased steadily from the pre-industrial period (taken as 1850-1869), peaking in the 1980s when the global dust loading peaked[4], after which it decreased. The corresponding global mean LW DRF - obtained by differencing the LW DRE from its pre-industrial value - also increased steadily until it peaked at +0.14 ± 0.07 Wm^{-2} in the 1980s (Fig. 4b), thereby enhancing greenhouse warming. The LW DRF is thus substantial compared to the anthropogenic aerosols DRF[6] of -0.22 (-0.47 to +0.04) Wm^{-2}. Moreover, the dust LW DRF close to source regions reaches up to a few Wm^{-2}, which is over an order of magnitude larger than its global mean value (Fig. 3d). Because climate models underestimate the LW DRE (Fig. 4a) and do not capture the historical increase in dust[4], they have almost entirely omitted this substantial radiative forcing (Fig. 4c).

The role of dust LW DRF in future climate change remains uncertain because future changes in dust are not well understood. Climate model projections diverge widely[41-43] due to large uncertainties in the changes in key drivers of dust emissions, such as winds, soil moisture, and sediment supply[4]. To improve the accuracy of simulated future dust DRF, models need both more reliable predictions of dust emissions[41,42], as well as and a better representation of LW scattering interactions[12] and enhanced concentrations of super coarse dust[19].

The heating caused by the dust LW DRF has been offset by cooling from the dust SW DRF, since increased dust has also amplified the SW DRE. However, the SW DRE remains highly uncertain[7-9], with a recent review[4] constraining it to $-0.40 \pm 0.25\ Wm^{-2}$. Consequently, the sign of the total dust DRE (SW + LW) is still unclear, and it remains uncertain whether increased dust loading has, overall, heated or cooled the global climate system[4]. Although LW heating and SW cooling counteract each other in the global energy budget, their relative magnitudes vary greatly by region. Specifically, heating from the LW DRF is largest near dust source regions, whereas cooling from the SW DRF is strongest over oceans and other low-albedo surfaces downwind of sources[25,41]. This spatially varying dipole pattern in net dust DRF influences atmospheric dynamics, tropical cyclones, and monsoons[44-46].

In conclusion, we constrain the global annual mean heating from dust interactions with longwave radiation to $+0.25 \pm 0.06\ W/m^2$ at the top-of-atmosphere. This estimate is derived from a data-driven analytical model that integrates atmospheric and surface properties with observational constraints on dust abundance and characteristics. Our bottom-up calculations are statistically consistent with both the magnitude and spatial variability of observational estimates of LW direct radiative effects, yielding results in substantially better agreement with observations than current climate models (Fig. 2). Most models neglect longwave scattering, which contributes over half of the global mean longwave direct radiative effect, and underestimate or omit super coarse dust, which accounts for roughly 20% of the effect. Consequently, models underestimate the longwave direct radiative effect by about a factor of two (Fig. 4a). We further find that historical increases in dust[4] generated a longwave direct radiative forcing that peaked at $+0.14 \pm 0.07\ W/m^2$ in the 1980s, before declining. This warming partially offset the cooling from dust's shortwave direct radiative forcing and from other anthropogenic aerosols, which contributed a direct radiative cooling estimated at $-0.22 \pm 0.25\ W/m^2$ in 2019 relative to pre-industrial times[6]. As such, the omission of dust longwave direct radiative forcing from current climate models (Fig. 4c) could bias assessments of climate sensitivity and projections of future climate change. Improved representation of this effect could therefore enhance the accuracy of future climate projections.

Methods

Data-driven analytical model of dust LW radiative effects at TOA. We use a combination of theory, model simulations, and observations of dust abundance and LW radiative effects to constrain the LW DRE at TOA (Fig. S1). First, we derive a simplified model that captures the essence of how the dust LW DRE at TOA depends on atmospheric, surface, and dust properties[12]. We then calculate the dust LW DRE by driving this model with data on dust properties and abundance from the DustCOMM data set (described in the Supplement and in Refs. [10,14,23]), data on dust LW optical properties from various laboratory and in situ measurements[13], and data on atmospheric and surface properties from reanalysis data sets[47]. We propagate the uncertainties in these various data sets through a bootstrap procedure, yielding many (1,000) simulations of the LW DRE. We then apply a compilation of observational estimates of the clear-sky LW DREE[21,24] to eliminate the subset of simulations (~55%) that are statistically inconsistent with these observations. By combining the clear-sky LW DRE with an ensemble of model simulations of the ratio of the all-sky to the clear-sky LW DRE we then obtained the all-sky LW DRE at TOA. Finally, we combined the present-climate all-sky LW DRE with a reconstruction of the global dust cycle from 1841-2000[4] to obtain the temporal evolution of the LW DRE and therefore the LW DRF since pre-industrial times.

As illustrated in Extended Data Fig. 1, we consider a dust layer with optical depth τ_{LW} at some LW wavelength λ and effective emission temperature T_{d} (see definition in Supplement and Fig. S11e). The upwelling spectral flux ($\mathrm{Wm^{-2}\mu m^{-1}}$) immediately below the dust layer is[48]:

$$F_{\mathrm{s,eff}\uparrow}(\lambda) = \pi B\left(T_{\mathrm{s,eff}}, \lambda\right), \tag{1}$$

where B is the Planck function that describes the spectral intensity of a blackbody as a function of temperature. Further, $T_{\mathrm{s,eff}}$ is the effective emission temperature of upwelling radiation below the dust layer, which is defined in the supplement and depends primarily on the surface temperature T_{s} (Fig. S11a) and surface emissivity ϵ_{s} (Fig. S11b), with a small correction due to absorption and emission by the atmosphere below the dust layer. Because the surface emissivity can be substantially below 1 for desert regions, $T_{\mathrm{s,eff}}$ - T_{s} can be up to ~5 °C (Fig. S11d).

The upwelling spectral irradiance immediately above the dust layer is then

$$\begin{aligned} F_{\mathrm{d}\uparrow}(\lambda) = \pi B\left(T_{\mathrm{s,eff}}, \lambda\right)[1 - \epsilon_{\mathrm{d}}(\lambda)] + \epsilon_{\mathrm{d}}(\lambda)\pi B(T_{\mathrm{d}}, \lambda) \\ - \pi R_{\mathrm{d}}(\lambda)\left[B\left(T_{\mathrm{s,eff}}, \lambda\right) - \epsilon_{\mathrm{abv}}(\lambda) B(T_{\mathrm{abv}}, \lambda)\right] \end{aligned} \tag{2}$$

where ϵ_{d} is the emissivity of the dust layer and ϵ_{abv} and T_{abv} are respectively the absorptivity (Fig. S11g) and effective emission temperature at wavelength λ of the atmosphere above the dust layer, such that $\pi R_{\mathrm{d}} \epsilon_{\mathrm{abv}} B(T_{\mathrm{abv}}, \lambda)$ represents the spectral radiance due to upward scattering by dust of radiation emitted downward by the overlying atmosphere. Eq. (2) assumes that ϵ_d and ϵ_{abv} are << 1, which is a reasonable assumption only in the atmospheric window (see further discussion below). Further, R_{d} is the fraction of upwelling radiation that is scattered downward by the dust layer. For isotropic radiation and in the limit of τ_{LW} << 1 (see supplement for a discussion of the impact of this assumption), ϵ_d and R_{d} equal[49,50]

$$\epsilon_{\mathrm{d}}(\lambda) = [1 - \omega(\lambda)]\left[1 - \exp\left(-\frac{\tau_{\mathrm{LW}}(\lambda)}{\tilde{\mu}}\right)\right], \tag{3}$$

$$R_{\mathrm{d}}(\lambda) = \omega(\lambda)\beta_{\downarrow}\left[1 - \exp\left(-\frac{\tau_{\mathrm{LW}}(\lambda)}{\tilde{\mu}}\right)\right], \tag{4}$$

where $\omega(\lambda)$ is the dust layer's single-scattering albedo (Fig. S6) and $\tilde{\mu} = 0.6$ is the cosine of the effective zenith angle[48]. Furthermore, $\beta_{\downarrow}$ is the downscatter fraction, that is, the fraction of dust-scattered upwelling LW radiation that is scattered back towards Earth's surface. Note that the downscatter fraction $\beta_{\downarrow}$ thus differs from the backscatter fraction b, which is the fraction scattered into the backward hemisphere relative to the direction of propagation of the incoming radiation; only for straight-upward traveling radiation do we have that $\beta_{\downarrow} = b$, whereas $\beta_{\downarrow} > b$ for all other zenith angles. From geometrical arguments, $\beta_{\downarrow} = \beta_{\uparrow}$ for isotropic radiation, where $\beta_{\uparrow}$ is the fraction of scattered downwelling radiation that is scattered upwards, known as the upscatter fraction $\beta_{\uparrow}$[51]. For isotropic radiation, this upscatter fraction depends only on the phase function P, which defines the probability distribution of the scattering angle θ relative to the direction of propagation. Neglecting multiple scattering interactions, Wiscombe and Grams[49] showed that

$$\beta_{\uparrow} = \frac{1}{2\pi}\int_0^{\pi} \theta P(\cos\theta)\sin\theta \, d\theta, \tag{5}$$

which we use to calculate $\beta_{\downarrow}$ (Fig. S6). The downscatter fraction thus depends only on the phase function, which we calculate using Mie theory and the refractive indices reported in Table S4. The downscatter fraction equals 0.5 in the limit of $D << \lambda$ (asymmetry factor $g = 0$) and decreases to zero in the limit of $D >> \lambda$ ($g = 1$)[49,51]. The upwelling spectral irradiance above the dust layer is affected by absorption and emission by the colder atmosphere above (Extended Data Fig. 1), such that the upwelling spectral irradiance at TOA is reduced:

$$F_{\mathrm{TOA}\uparrow}(\lambda) = [1 - \epsilon_{\mathrm{abv}}(\lambda)]F_{\mathrm{d}\uparrow} + \epsilon_{\mathrm{abv}}(\lambda)\pi B(T_{\mathrm{abv}}, \lambda). \tag{6}$$

We then obtain the spectral LW DRE at the TOA by subtracting from Eq. (6) the corresponding equation without the dust layer present ($\tau_{\mathrm{LW}} \rightarrow 0$) and rearranging terms:

$$\begin{aligned} \Delta F_{\mathrm{TOA}\uparrow}(\lambda) = -\pi[1 - \epsilon_{\mathrm{abv}}(\lambda)]\{&\epsilon_{\mathrm{d}}(\lambda)[B(T_{\mathrm{s,eff}}, \lambda) - B(T_{\mathrm{d}}, \lambda)] \\ &+ R_{\mathrm{d}}(\lambda)[B(T_{\mathrm{s,eff}}, \lambda) - \epsilon_{\mathrm{abv}}(\lambda)B(T_{\mathrm{abv}}, \lambda)]\}, \end{aligned} \tag{7}$$

The first term in Eq. (*7*) represents the effect of absorption, which is mitigated by emission at T_{d}; the second term represents the effect of downward scattering of upwelling radiation by dust, the effect of which is mitigated somewhat by upward scattering of downwelling atmospheric radiation. The integration of Eq. (*7*) over the full LW spectrum then yields the LW DRE at the TOA:

$$\begin{aligned} R_{\mathrm{TOA}} &= -\int \Delta F_{\mathrm{TOA}\uparrow}(\lambda) d\lambda = \\ &\int \pi[1 - \epsilon_{\mathrm{abv}}(\lambda)]\{\epsilon_{\mathrm{d}}(\lambda)[B(T_{\mathrm{s,eff}}, \lambda) - B(T_{\mathrm{d}}, \lambda)] \\ &\qquad + R_{\mathrm{d}}(\lambda)[B(T_{\mathrm{s,eff}}, \lambda) - \epsilon_{\mathrm{abv}}(\lambda)B(T_{\mathrm{abv}}, \lambda)]\}d\lambda, \end{aligned} \tag{8}$$

where a minus sign was added because a decrease of the outgoing LW radiation corresponds to a gain of energy to the climate system and thus a positive LW DRE.

Eqs. (7) and (8) show explicitly that the dust LW DRE at TOA decreases with absorption above the dust layer. Dust radiative effects are therefore negligible for wavelengths for which the atmosphere is opaque[12]. This leads to two important conclusions: (i) dust radiative effects are only important in the spectral region of the atmosphere that is transparent to LW radiation – the so-called "atmospheric window" around 8 – 14 μm wavelength – because strong absorption by water vapor and other gases make the atmosphere opaque outside of this window, and (ii) the LW DRE at TOA is negligible when clouds – which block the atmospheric window by absorbing strongly and broadly in the LW spectrum – are present above the dust layer (with the exception of optically thin cirrus clouds)[12].

We use the observation that dust radiative effects are only important within the atmospheric window to simplify Eq. (8) by using values of the dust optical properties ($\bar{\varpi}$ and $\bar{\beta}_{\downarrow}$) averaged over the atmospheric window wavelength range (Table S4). This is further justified by the uncertainty in these parameters being of similar order of magnitude as their variation in the atmospheric window (see, e.g., Fig. 12 in Ref. [13]). We similarly also use the wavelength-averaged values of the atmospheric absorptivities ($\bar{\epsilon}_{\mathrm{bel}}$ and $\bar{\epsilon}_{\mathrm{abv}}$) and calculate the LW extinction ($\bar{\tau}_{\mathrm{LW}}$, $\bar{\epsilon}_{\mathrm{d}}$, and $\bar{R}_{\mathrm{d}}$) based on the size-resolved column loading and optical properties ($\overline{k_{\mathrm{ext}}}$, $\bar{\varpi}$, and $\bar{\beta}_{\downarrow}$) representative of the entire atmospheric window wavelength range (Table S4). That is,

$$R_{\mathrm{TOA}} = \pi(1-\bar{\epsilon}_{\mathrm{abv}})\int_{\lambda_{\min}}^{\lambda_{\max}}\{\bar{\epsilon}_{\mathrm{d}}[B(T_{\mathrm{s,eff}},\lambda)-B(T_{\mathrm{d}},\lambda)] + \bar{R}_{\mathrm{d}}[B(T_{\mathrm{s,eff}},\lambda)-\bar{\epsilon}_{\mathrm{abv}}B(T_{\mathrm{abv}},\lambda)]\}d\lambda, \tag{9}$$

We now simplify Eq. (9) further by evaluating the integral of the Planck function over the atmospheric window. We use the Stefan-Boltzmann law to write

$$\int_{\lambda_{\min}}^{\lambda_{\max}}\pi B(T_{\mathrm{emit}})d\lambda = \sigma_{\mathrm{SB}}f_{\mathrm{aw}}(T_{\mathrm{emit}})T_{\mathrm{emit}}^4, \tag{10}$$

where σ_{SB} is the Stefan-Boltzmann constant and f_{aw} is the fraction of emitted radiation that is in the atmospheric window, which is a weakly increasing function of the emitting temperature (T_{emit}) at the range of temperatures encountered in the troposphere (Fig. S12). Substituting Eq. (10) into Eq. (9) finally yields the clear-sky LW DRE at TOA produced by dust in an atmospheric column:

$$R_{\mathrm{CS}} = \sigma_{\mathrm{SB}}(1-\bar{\epsilon}_{\mathrm{abv}})f_{\mathrm{aw}}(T_{\mathrm{s,eff}})T_{\mathrm{s,eff}}^4\left[\bar{\epsilon}_{\mathrm{d}}\left(1-\frac{f_{\mathrm{aw}}(T_{\mathrm{d}})}{f_{\mathrm{aw}}(T_{\mathrm{s,eff}})}\frac{T_{\mathrm{d}}^4}{T_{\mathrm{s,eff}}^4}\right) + \bar{R}_{\mathrm{d}}\left(1-\bar{\epsilon}_{\mathrm{abv}}\frac{f_{\mathrm{aw}}(T_{\mathrm{abv}})}{f_{\mathrm{aw}}(T_{\mathrm{s,eff}})}\frac{T_{\mathrm{abv}}^4}{T_{\mathrm{s,eff}}^4}\right)\right]. \tag{11}$$

Eq. (11) shows that the TOA LW DRE has two distinct contributions. The first contribution (left-hand term inside the square brackets) is due to dust absorption of radiation that is emitted from the warmer surface and atmosphere below. The radiative effect of this absorption is countered by the emission of LW radiation by the dust layer at a lower temperature. As such, this term depends on the temperature difference of the dust layer with the surface and atmosphere below, which in turn is largely controlled by the height of the dust layer. The second contribution (right-hand term inside the square brackets) is due to the downward scattering of upwelling LW radiation by dust. This contribution is countered somewhat by upward scattering of downwelling radiation emitted by the overlying atmosphere. This causes a weaker dependence on dust layer height than occurs for LW absorption, such that the relative importance of LW scattering increases with decreasing dust layer altitude [12]. Note that the contributions of both LW absorption and LW scattering to the TOA LW DRE are decreased by the absorption and emission of LW radiation by the colder atmosphere above the dust layer.

Using dust optical properties, DustCOMM, and reanalysis data to calculate LW DRE at TOA during clear-sky conditions. We want to use Eq. (11) to constrain the climatology of the LW DRE at TOA, as a function of longitude, latitude, and time (season). Doing so requires quantification of all the variables and their uncertainties in Eq. (11), starting with the dust optical properties. We obtained the downscatter fraction ($\bar{\beta}_{\downarrow}$), single-scattering albedo ($\bar{\omega}$), and the mass extinction efficiency ($\bar{k}_{\text{ext}}$), which co-determines the dust aerosol optical depth ($\bar{\tau}_{\text{LW}}$), from Mie theory using six different data sets of published LW optical properties (see Supplement for details). This yielded values of $\bar{\beta}$ that decrease from 0.5 for very fine dust to ~0.15 for super coarse dust, values of $\bar{\omega}$ that increase strongly with particle diameter from ~0 for very small dust to ~0.5 for super coarse dust, and values of $\bar{k}_{\text{ext}}$ ranging from ~0.08 to 0.2 m^2g^{-1} (see Supplementary Methods and Table S4). Since the dust size distribution is variable in space and time, so are the corresponding bulk dust optical properties (Fig. S6).

The second ingredient needed to use Eq. (11) is the spatiotemporal pattern of the size-resolved dust concentration, which co-determines $\bar{\tau}_d$ and T_{d}. We obtained this from the DustCOMM data set[23], which constrained the climatology of the size-resolved concentration of dust up to 20 μm diameter as a function of latitude, longitude, height, and season from observational and modeling constraints on dust properties and abundance for the years 2004-2008. We extended this data set to include dust with diameters between 20 to 100 μm using simulations from Meng et al.[30] of the ratio of dust mass loading in this size range with dust mass loading for particles with $D \leq 20$ μm. As described in more detail in Adebiyi et al.[19], in order to match measurements of dust size distributions far from source regions, these simulations used a dust density reduced by a factor of 10 (250 kg m^{-3}) as a proxy for as-of-yet unclear processes missing from models that likely cause coarse dust to deposit less quickly than simulated in models[30]. These simulations indicate that dust with $D > 20$ μm accounts for ~2% of the global mean LW DAOD[19], although in situ measurements suggest that this might be an underestimation[31].

The final ingredient needed to use Eq. (11) is data on surface properties (temperature and emissivity) and atmospheric properties (vertical profiles of temperature and absorptivity and the downwelling radiation at the surface), which co-determine $\bar{\epsilon}_{\text{abv}}$, $\bar{\epsilon}_{\text{bel}}$, T_{bel}, T_{abv}, and T_{d}. We obtained surface temperature (T_{s}) from the MERRA-2 [52] meteorological reanalysis data set (Fig. S11a). Furthermore, we assumed that ocean surface emissivity is 0.985 based on theory and observations[53] and obtained land surface emissivity from the five wavelength bands of land surface emissivity retrieved by the Advanced Spaceborne Thermal Emission and Reflection Radiometer (ASTER) in the atmospheric window[54]. Note that some deserts have surface emissivity substantially less than 1 (Fig. S11b), particularly the Sahara desert, which is important to account for in accurate calculations of the LW DRE[55]. Finally, data on atmospheric absorptivity and downwelling radiation at the surface were obtained for clear-sky conditions, averaged over the atmospheric window (using λ_{min} = 8 μm to λ_{max} = 14 μm) by forcing the LibRadTran radiative transfer model[56,57] with MERRA-2[52] seasonally averaged reanalysis data of 2D surface temperature and 3D atmospheric temperature, atmospheric humidity and ozone. We obtained these seasonally averaged data for 6-hour increments (0, 6, 12, and 18 UTC) to account for the effect of diurnal variability in surface temperature and in vertical profiles of atmospheric water vapor, ozone, and temperature on the dust LW DRE. Relative to using diurnally averaged data, the effect of this accounting for diurnal variability was of the order of a few percent over land and less over ocean. As such, using higher temporal resolution data would have had negligible impact on our results compared to other uncertainties in the analysis. All 6-hourly and seasonally averaged reanalysis data was further averaged over the years 2004-2008 to match the period for which the DustCOMM dust climatology data was obtained[23].

Combining all these ingredients together yielded the spatiotemporal pattern of the LW DRE at TOA for clear-sky conditions (Fig. 1).

Using model simulations to calculate all-sky LW DRE from clear-sky LW DRE. The approach above constrains the clear-sky LW DRE (Figures 2, 3a), but the all-sky LW DRE is more important for the Earth's energy balance. If clouds are present above the dust layer then the TOA LW DRE is essentially zero[12,18], as is likely also the case for the SW DRE[58]. However, if clouds are present below the dust layer, then these normally decrease the effective surface temperature T_{b}, thereby somewhat decreasing the TOA LW DRE while increasing the fraction of that LW DRE that is due to scattering. These interactions are too complicated to account for in our analytical model and we thus use results from climate models to convert the clear-sky to the all-sky LW DRE at TOA:

$$R_{\mathrm{AS}}(s,\theta,\phi) = \eta(s,\theta,\phi) R_{\mathrm{CS}}(s,\theta,\phi), \tag{12}$$

where s denotes the season, θ and ϕ denote longitude and latitude, and η is the spatiotemporally varying ratio of the all-sky to the clear-sky LW DRE at TOA based on our ensemble of climate model simulations (see Figs. S1, S4). Note that a limitation of these model results is that they do not calculate the effect of dust LW scattering.

Propagation of uncertainty and use of LW DREE observations using bootstrap procedure. Each of the data sets used in the calculation of the LW DRE has uncertainties, which we propagated to the extent possible using a bootstrap method that also integrates observationally based estimates of the LW DREE. In order to compare our results against these observations, we used our analytical model to calculate the LW DREE (Ω_{mdl}) by dividing the clear-sky LW DRE (R_{CS}, Eq. 11) by the clear-sky dust aerosol optical depth in the shortwave spectrum at 550 nm (τ_{SW}). That is,

$$\Omega_{\mathrm{mdl}} = \frac{R_{\mathrm{TOA}}}{\tau_{\mathrm{SW}}} = \sigma_{\mathrm{SB}}(1-\bar{\epsilon}_{\mathrm{abv}}) f_{\mathrm{aw}}(T_{\mathrm{s,eff}}) T_{\mathrm{s,eff}}^4 \left[\frac{\bar{\epsilon}_{\mathrm{d}}}{\tau_{\mathrm{SW}}}\left(1-\frac{f_{\mathrm{aw}}(T_{\mathrm{d}})}{f_{\mathrm{aw}}(T_{\mathrm{s,eff}})}\frac{T_{\mathrm{d}}^4}{T_{\mathrm{s,eff}}^4}\right) + \frac{\bar{R}_{\mathrm{d}}}{\tau_{\mathrm{SW}}}\left(1-\bar{\epsilon}_{\mathrm{abv}}\frac{f_{\mathrm{aw}}(T_{\mathrm{abv}})}{f_{\mathrm{aw}}(T_{\mathrm{s,eff}})}\frac{T_{\mathrm{abv}}^4}{T_{\mathrm{s,eff}}^4}\right)\right]. \tag{13}$$

Because both $\bar{\epsilon}_{\mathrm{d}}$ and $\bar{R}_{\mathrm{d}}$ scale with $\bar{\tau}_{\mathrm{LW}}$, a major determinant of Ω_{mdl} is the ratio of the clear-sky LW to SW DAOD ($\bar{\tau}_{\mathrm{LW}}/\tau_{\mathrm{SW}}$), which is plotted in Fig. S13.

We performed a sufficiently large number of simulations (1,000) that our results did not change substantially with additional simulations. For each simulation, we drew from the probability distributions or ensembles of the data sets that are inputs to the analytical model (see Fig. S1). We then compared the calculated LW DREE (Eq. 13) against the compilation of observational estimates (see below) and, in a procedure similar to that used in perturbed parameter ensembles[59], we only retained the simulations consistent with these observational estimates (Extended Data Fig. 2). However, this procedure is hindered by the fact that most LW DREE observations did not include uncertainties, and even those studies that did[55,60] accounted for different factors in this uncertainty. Therefore, we estimated a common uncertainty on all reported observational DREE values as the standard deviation of groups of LW DREE values for similar regions. Specifically, the various observations of LW DREE over the springtime Sahara (six total; Ref. [21]) show a standard deviation of 1.6 $\mathrm{Wm^{-2}}$; observations of LW DREE over the summertime Sahara (eight total; Refs. [21,55,61]) show a standard deviation of 2.5 $\mathrm{W/m^2}$; and the two measurements over the tropical North Atlantic in September[62,63] show a spread of 3.3 $\mathrm{Wm^{-2}}$. Based on this, we estimate an observational error of ±2 $\mathrm{Wm^{-2}}$. Accordingly, simulations that perfectly reproduce nature would be expected to have a root-mean-squared error (RMSE) of $\mathrm{RMSE_{min}}$ = ~2 $\mathrm{Wm^{-2}}$ relative to these observations. And indeed, simulations in our bootstrap ensemble have a minimum RMSE of ~2 $\mathrm{W/m^2}$, so similar to $\mathrm{RMSE_{min}}$ (Extended Data Fig. 2). We therefore retained simulations with twice this minimal error, so with RMSE < $\mathrm{RMSE_{max}}$, where $\mathrm{RMSE_{max}} = 2\times\mathrm{RMSE_{min}}$ = 4 $\mathrm{Wm^{-2}}$. This procedure eliminated the ~55% of the bootstrap simulations that are in poorest agreement with the LW DREE observations. The result that nearly half of our bootstrap iterations are statistically consistent with the compilation of LW DREE observations supports closure between the "bottom-up" calculation of the LW DRE and "top-down" constraints from in situ and satellite data. However, this closure could be due to canceling errors (see Supplementary Methods). Note that our main results are relatively insensitive to the exact value of $\mathrm{RMSE_{max}}$. In fact, applying no constraint ($\mathrm{RMSE_{max}} = \infty$) yields a median all-sky LW DRE of +0.25 $\mathrm{Wm^{-2}}$, which is identical to our results using $\mathrm{RMSE_{max}}$ = 4 $\mathrm{Wm^{-2}}$ (Fig. 4a). Moreover, using an $\mathrm{RMSE_{max}}$ of 3 $\mathrm{Wm^{-2}}$, which retains only ~24% of bootstrap iterations, also yields a similar median all-sky LW DRE of +0.27 $\mathrm{Wm^{-2}}$.

The bootstrap procedure yields a probability distribution of the dust LW DRE, which we use to quantify the errors in our results[64,65]. These uncertainties should be seen as a lower bound because of the possibility of systematic errors that were not accounted for, including in the observational LW DREE estimates. These and other limitations, as well as the bootstrap procedure, are described in more detail in the Supplementary Methods.

Compilation of observational estimates of the clear-sky LW DREE. Over a dozen studies have used observations to estimate the clear-sky LW DREE. Those studies can be roughly divided into two groups. The first group of studies used ground-based and/or in situ measurements of radiative fluxes, dust aerosol properties (e.g., size distribution), and/or atmospheric and surface properties (temperature and humidity profiles) to inform and constrain a radiative transfer model that was then used to calculate the clear-sky LW DREE[60,66]. The second group of studies combined satellite remote sensing data of SW (dust) aerosol optical depth and LW flux measurements to estimate the clear-sky LW DREE, often also using a radiative transfer model[21,24]. We combined estimates of both types of studies into a compilation of observational estimates of the clear-sky LW DREE at TOA. For quality control purposes, we excluded studies that (i) did not account for the effect on TOA LW fluxes of the co-variability of dust with atmospheric humidity and surface temperature[67-69], which confound the effects of dust on OLR in the atmospheric window[21] (ii) studies that did not use observations of LW fluxes to constrain the results from a radiative transfer model[70], and (iii) studies that were based on very small amounts of observational data or had very large uncertainties in those data[71]. We did not include the results of Brindley[72] because these results were superseded by Brindley and Russell[21]. We also did not include the results of Kuwano et al.[73] because these results, obtained near the Salton Sea in California, are not representative of the long-range transported dust that is most relevant to climate, but rather of locally emitted dust confined within 1-2 km of the ground, which models struggle to accurately represent in marginal source regions like the U.S. Southwest[74]. Furthermore, we combined the estimates of di Sarra et al.[75] and Meloni et al.[76], both of which were obtained during spring time at the Mediterranean island of Lampedusa and had similar methods and author teams. Overall, we identified 11 studies that met these criteria, yielding a total of 21 observationally informed estimates of the clear-sky LW DREE (see Table S5). To directly compare the observational clear-sky LW DREE estimates to the seasonally and diurnally averaged results presented in this paper, we applied a correction factor to convert all observations in our compilation to a seasonally and diurnally averaged value (see Supplement).

Calculation of timeseries of the dust LW direct radiative effect and forcing. We combined our observationally constrained present-day LW DRE with a recent reconstruction of the historical change in global dust loading[4] to obtain the historical evolution of the dust LW DRE and thereby also the dust LW DRF. In doing so, we assumed that the perturbation to Earth's energy budget from the change in dust scales linearly with both dust loading and the present-climate LW DRE[9,77]. That is, we calculated the LW DRE in decade *d* as

$$R_{\text{hist}}(d) = \frac{R_{\text{mdrn}}}{L_{\text{mdrn}}}\, L_{\text{hist}}(d)\,, \tag{14}$$

where L_{hist} is the historical global dust loading in decade *d*. Furthermore, $R_{\text{mdrn}} = R_{\text{AS}}$ (see Eq. 12) and L_{mdrn} respectively denote the top-of-atmosphere global mean all-sky LW DRE and the global dust loading in the modern period for which the DustCOMM data set was obtained (2004-2008); our results here show that the amount of TOA LW DRE per unit global dust loading equals $\frac{R_{\text{mdrn}}}{L_{\text{mdrn}}} = 0.010 \pm 0.004$ $\text{Wm}^{-2}\text{Tg}^{-1}$. The LW direct radiative forcing $\Delta F(d)$ is then obtained by subtracting $R_{\text{hist}}(d)$ from its value R_{pi} in the pre-industrial period, which we take as 1850-1869:

$$\Delta F(d) = R_{\text{hist}}(d) - R_{\text{pi}} = \frac{R_{\text{mdrn}}}{L_{\text{mdrn}}} \Delta L(d) \,, \tag{15}$$

where $\Delta L(d) = \left[L_{\text{hist}}(d) - L_{\text{pi}}\right]$. We obtained this increase in the global dust loading since the pre-industrial period from Kok et al.[4], who found that global dust loading increased from 19 ± 6 Tg in the pre-industrial period to a peak of 33 ± 10 Tg in the 1980s.

In using Eq. (15), we assume that the global dust cycle did not change between the 1990s, which is the last decade for which the dust loading was reconstructed based on sedimentary records in Kok et al.[4], and 2004-2008, which is the period for which the DustCOMM data set was obtained. Note that we further assume for simplicity that the entire radiative perturbation due to dust changes is a radiative forcing, whereas in reality it might be a combination of a forcing and a feedback. This issue is discussed in more detail in Mahowald et al.[78].

Calculation of dust LW direct radiative effect and forcing from climate model results. We obtained a timeseries of the LW DRE and DRF that is representative of current climate models as follows. First, we obtained a compilation of 20 climate model simulation results of the LW DRE (Table S1), which includes results from the six models used in DustCOMM (see Fig. S14) as well as results from numerous studies published in the literature since 2014. We then combined these 20 modeling values of the LW DRE with 12 quantifications $L_{\text{hist}}(d)$ from historical runs (spanning 1850-2000) in the Coupled Model Intercomparison Project phase 6 (CMIP6) models shown in Fig. 5 of Kok et al.[4]. This yields an ensemble of 240 modeling results of ΔF for each decade:

$$\Delta F_{i,j}(d) = \frac{R_{\text{mdrn},i}}{L_j} \Delta L_j(d) \,, \tag{16}$$

where i indexes the 20 model simulations of the modern climate LW DRE and j indexes the 12 CMIP6 simulations of dust historical changes. For each decade, we then extracted from these 240 values of $\Delta F_{i,j}$ the median value and the range containing 90% of these values, which we report as the 90% confidence interval in Figs. 4b and 4c.

Limitations of the methodology. Our methodology is subject to important limitations, which we discuss in detail in the Supplementary Methods and summarize below. First, simplifying assumptions and treatments required to keep the analytical model solvable can cause biases in our results. These include assuming that dust and atmospheric absorption are small (i.e., $\bar{\tau}_{\text{LW}}$, $\bar{\epsilon}_{\text{bel}}$, $\bar{\epsilon}_{\text{abv}} << 1$), using atmospheric and dust properties spectrally averaged over the atmospheric window rather than resolving spectral variability, and using seasonally averaged inputs, thereby neglecting sub-seasonal co-variability between input fields. Second, our results could be biased due to errors in the input data (e.g. atmospheric temperature and humidity fields and dust concentration, size distribution, altitude, and optical properties). Third, errors in observational LW DREE estimates could cause biases. These observational estimates often focus on intense dust events with atypical properties, may conflate surface temperature responses with radiative effects, and are regionally and seasonally biased towards North African dust in the spring and summer seasons. These limitations are partially mitigated by retaining only bootstrap iterations consistent with observational constraints (Extended Data Fig. 2), but substantial biases remain possible because compensating errors could still result in agreement with these observations.

Data availability. The data shows in figures 1-4 are available at https://doi.org/xxxxx.

Code availability. The codes used to conduct the analysis presented in this paper and in the production of the figures is available from xxxx.

Acknowledgements. This work was developed with support from the National Science Foundation (NSF) grants 1856389 and 2151093 awarded to J.F.K. We also acknowledge high-performance computing support from NCAR's Computational and Information Systems Laboratory, sponsored by the National Science Foundation. AI acknowledges MEXT-Program for the advanced studies of climate change projection (SENTAN) Grant Number JPMXD0722681344. L.L. and N.M.M. acknowledge assistance from the Earth surface Mineral dust source InvesTigation (EMIT), a NASA Earth Ventures-Instrument (EVI-4) Mission, as well as from the Department of Energy (DOE) under award DE-SC0021302. MK has received funding from the Helmholtz Association's Initiative and Networking Fund (grant agreement no. VH-NG-1533). CPG-P and VO acknowledge support from the of the Spanish Ministerio de Economía y Competitividad through the HEAVY project (grant no. PID2022-140365OB-I00 funded by MCIN/AEI/10.13039/501100011033 and by ERDF/EU), the ERC under the Horizon 2020 research and innovation programme through the FRAGMENT project (grant agreement no. 773051), the Horizon Europe programme under Grant Agreement No 101137680 via project CERTAINTY, and the AXA Research Fund through the AXA Chair on Sand and Dust Storms at BSC. MK and CPG-P acknowledge PRACE for granting access to MareNostrum at the Barcelona Supercomputing Center to run MONARCH. RLM received support from the NASA Modeling, Analysis and Prediction Program.

Author contributions. J.F.K. conceived the project, designed the study, performed the analysis, and wrote the paper. A.K.G. contributed simulations of atmospheric absorptivity and A.T.E. contributed to designing the data-driven analytical model of the dust longwave direct radiative effect. A.A. and Y.H. provided dust optical properties data. S.A., Y.B., R.C.-G., P.R.C., D.H., A.I., M.K., L.L., N.M.M., R.L.M, V.O., C.P.G.-P., A.R.L., and J.W. contributed global model simulation data. All authors discussed the results and commented on the manuscript.

Competing interests. The authors declare no competing interests.

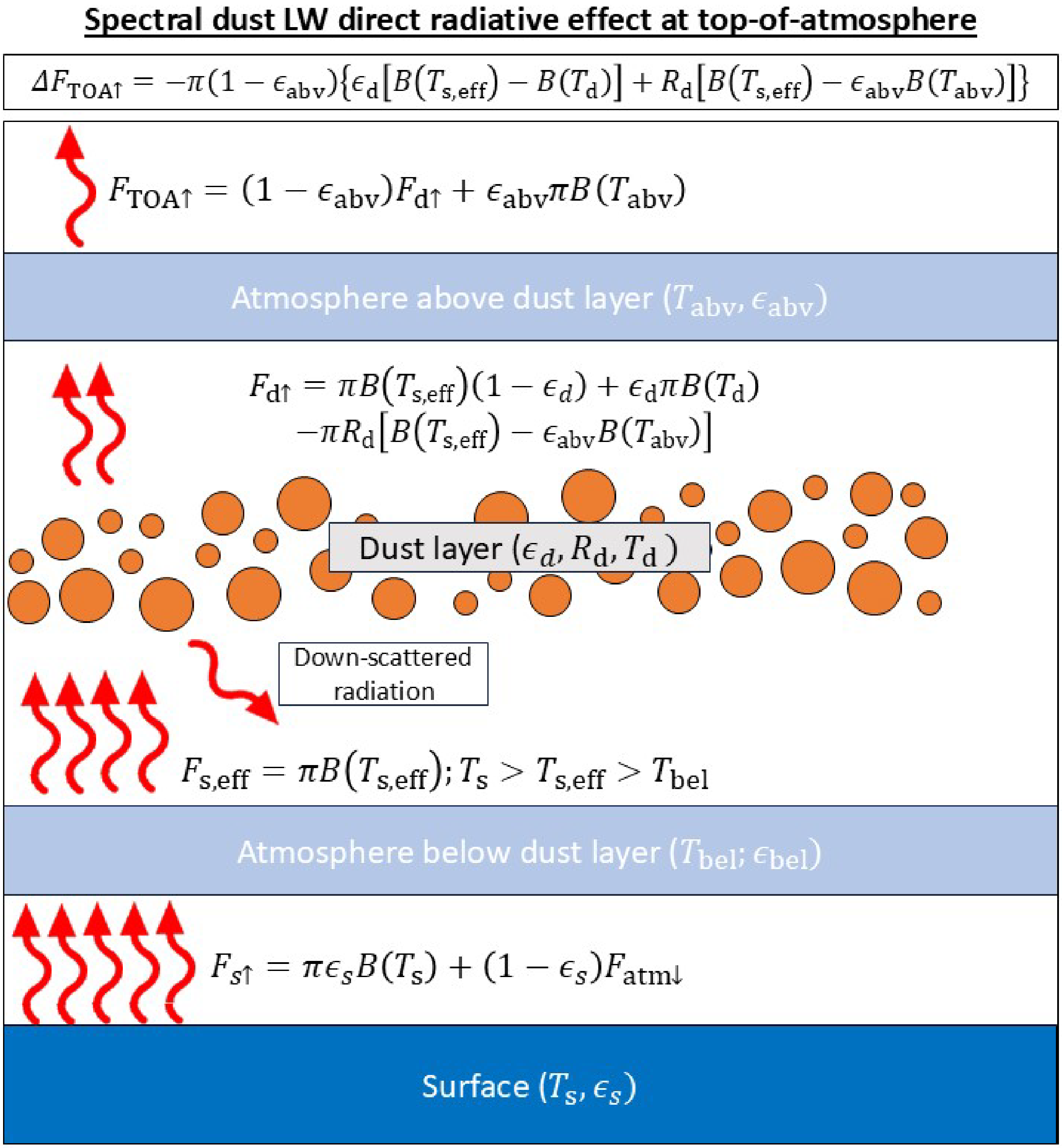

Extended Data Fig. 1. Conceptual model of the longwave (LW) direct radiative effect (DRE) at the top-of-atmosphere (TOA) created by a dust layer. The dependence of most variables on the wavelength λ is not explicitly denoted for simplicity but is defined in the text.

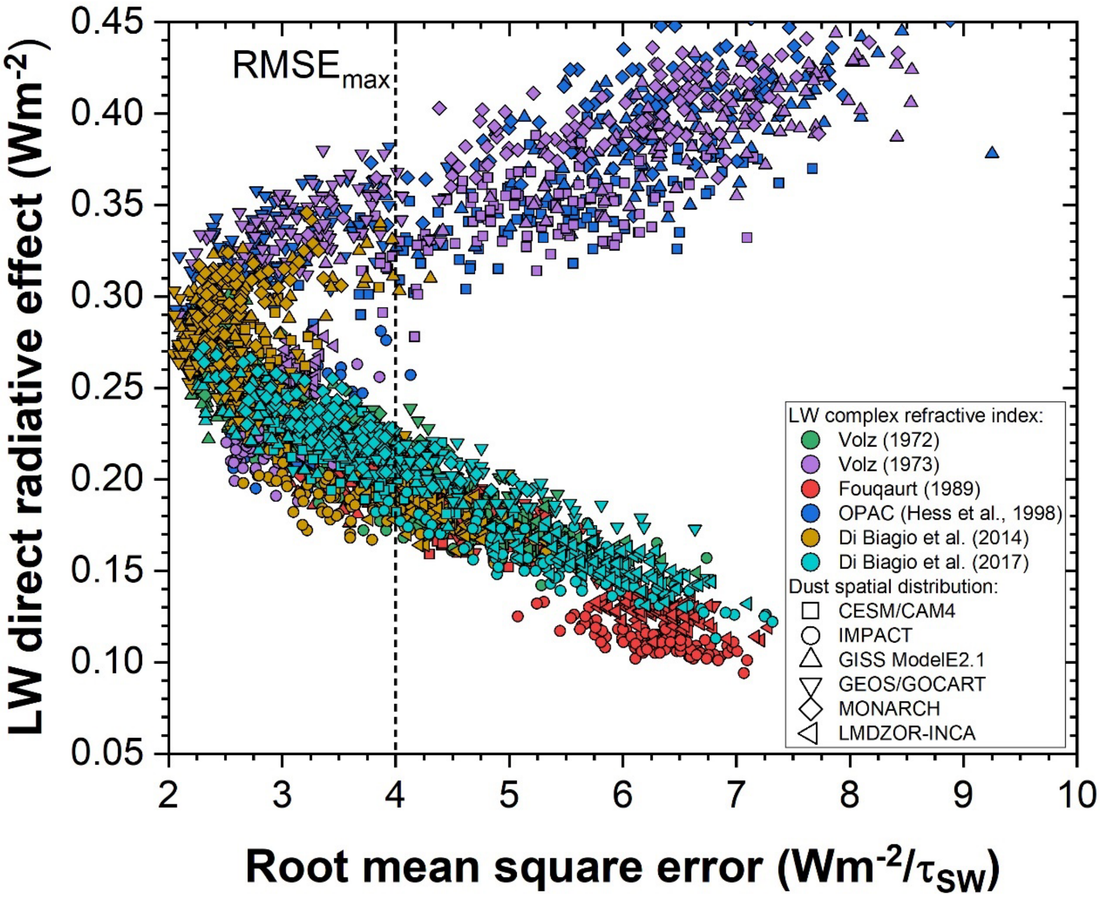

Extended Data Fig. 2. Root mean square error of individual bootstrap iterations of the data-driven analytical model with respect to a compilation of observational estimates of the dust LW direct radiative effect efficiency. Shown are 100 individual bootstrap iterations for each combination of the six LW complex refractive indices (Table S5; distinguished by symbol color) and the six global model simulations that co-determine the dust spatial distribution (see Kok et al.[23]; distinguished by symbol type).

References

1 Hooper, J. & Marx, S. A global doubling of dust emissions during the Anthropocene? *Glob. Planet. Change* **169**, 70-91, doi:10.1016/j.gloplacha.2018.07.003 (2018).

2 Mulitza, S. *et al.* Increase in African dust flux at the onset of commercial agriculture in the Sahel region. *Nature* **466**, 226-228, doi:10.1038/nature09213 (2010).

3 McConnell, J. R., Aristarain, A. J., Banta, J. R., Edwards, P. R. & Simoes, J. C. 20th-Century doubling in dust archived in an Antarctic Peninsula ice core parallels climate change and desertification in South America. *Proc. Natl. Acad. Sci. U. S. A.* **104**, 5743-5748, doi:10.1073/pnas.0607657104 (2007).

4 Kok, J. F. *et al.* Mineral dust aerosol impacts on global climate and climate change. *Nature Reviews Earth & Environment* **4**, 71–86, doi:10.1038/s43017-022-00379-5 (2023).

5 Sherwood, S. C. *et al.* An Assessment of Earth's Climate Sensitivity Using Multiple Lines of Evidence. *Reviews of Geophysics* **58**, doi:10.1029/2019rg000678 (2020).

6 Forster, P. *et al.* (eds V. Masson-Delmotte *et al.*) Ch. Chapter 7: The Earth’s energy budget, climate feedbacks, and climate sensitivity, (2021).

7 Di Biagio, C., Balkanski, Y., Albani, S., Boucher, O. & Formenti, P. Direct Radiative Effect by Mineral Dust Aerosols Constrained by New Microphysical and Spectral Optical Data. *Geophysical Research Letters* **47**, doi:10.1029/2019gl086186 (2020).

8 Li, L. L. *et al.* Quantifying the range of the dust direct radiative effect due to source mineralogy uncertainty. *Atmospheric Chemistry and Physics* **21**, 3973-4005, doi:10.5194/acp-21-3973-2021 (2021).

9 Kok, J. F. *et al.* Smaller desert dust cooling effect estimated from analysis of dust size and abundance. *Nature Geoscience* **10**, 274-278, doi:10.1038/ngeo2912 (2017).

10 Kok, J. F. *et al.* Contribution of the world's main dust source regions to the global cycle of desert dust. *Atmospheric Chemistry and Physics* **21**, 8169-8193, doi:10.5194/acp-21-8169-2021 (2021).

11 Wang, H. *et al.* Larger Dust Cooling Effect Estimated From Regionally Dependent Refractive Indices. *Geophysical Research Letters* **51**, doi:10.1029/2023GL107647 (2024).

12 Dufresne, J. L., Gautier, C., Ricchiazzi, P. & Fouquart, Y. Longwave scattering effects of mineral aerosols. *J. Atmos. Sci.* **59**, 1959-1966, doi:10.1175/1520-0469(2002)059<1959:lseoma>2.0.co;2 (2002).

13 Di Biagio, C. *et al.* Global scale variability of the mineral dust long-wave refractive index: a new dataset of in situ measurements for climate modeling and remote sensing. *Atmospheric Chemistry and Physics* **17**, 1901-1929, doi:10.5194/acp-17-1901-2017 (2017).

14 Adebiyi, A. A. & Kok, J. F. Climate models miss most of the coarse dust in the atmosphere. *Science Advances* **6**, eaaz9507, doi:10.1126/sciadv.aaz9507 (2020).

15 O'Sullivan, D. *et al.* Models transport Saharan dust too low in the atmosphere: a comparison of the MetUM and CAMS forecasts with observations. *Atmos. Chem. Phys.* **20**, 12955-12982, doi:10.5194/acp-20-12955-2020 (2020).

16 Kim, D. *et al.* Sources, sinks, and transatlantic transport of North African dust aerosol: A multimodel analysis and comparison with remote sensing data. *Journal of Geophysical Research-Atmospheres* **119**, 6259-6277, doi:10.1002/2013jd021099 (2014).

17 Miller, R. L. *et al.* Mineral dust aerosols in the NASA Goddard Institute for Space Sciences ModelE atmospheric general circulation model. *J. Geophys. Res.-Atmos.* **111**, D06208, doi:10.1029/2005jd005796 (2006).

18 Liao, H. & Seinfeld, J. H. Radiative forcing by mineral dust aerosols: sensitivity to key variables. *Journal of Geophysical Research-Atmospheres* **103**, 31637-31645 (1998).

19 Adebiyi, A. *et al.* A review of coarse mineral dust in the Earth system. *Aeolian Research* **60**, doi:10.1016/j.aeolia.2022.100849 (2023).
20 Ridley, D. A., Heald, C. L., Kok, J. F. & Zhao, C. An observationally-constrained estimate of global dust aerosol optical depth. *Atmos. Chem. Phys.* **16**, 15097-15117, doi:10.5194/acp-2016-385 (2016).
21 Brindley, H. E. & Russell, J. E. An assessment of Saharan dust loading and the corresponding cloud-free longwave direct radiative effect from geostationary satellite observations. *Journal of Geophysical Research-Atmospheres* **114**, doi:10.1029/2008jd011635 (2009).
22 Gelaro, R. *et al.* The Modern-Era Retrospective Analysis for Research and Applications, Version 2 (MERRA-2). *Journal of Climate* **30**, 5419-5454, doi:10.1175/jcli-d-16-0758.1 (2017).
23 Kok, J. F. *et al.* Improved representation of the global dust cycle using observational constraints on dust properties and abundance. *Atmospheric Chemistry and Physics* **21**, 8127-8167, doi:10.5194/acp-21-8127-2021 (2021).
24 Song, Q. Q. *et al.* Net radiative effects of dust in the tropical North Atlantic based on integrated satellite observations and in situ measurements. *Atmospheric Chemistry and Physics* **18**, 11303-11322, doi:10.5194/acp-18-11303-2018 (2018).
25 Song, Q. Q. *et al.* Size-resolved dust direct radiative effect efficiency derived from satellite observations. *Atmospheric Chemistry and Physics* **22**, 13115-13135, doi:10.5194/acp-22-13115-2022 (2022).
26 Gkikas, A. *et al.* Quantification of the dust optical depth across spatiotemporal scales with the MIDAS global dataset (2003-2017). *Atmospheric Chemistry and Physics* **22**, 3553-3578, doi:10.5194/acp-22-3553-2022 (2022).
27 Bellouin, N. & Yu, H. in *Aerosols and Climate* (ed K. Carslaw) (Elsevier, 2022).
28 Mlawer, E. J., Taubman, S. J., Brown, P. D., Iacono, M. J. & Clough, S. A. Radiative transfer for inhomogeneous atmospheres: RRTM, a validated correlated-k model for the longwave. *Journal of Geophysical Research-Atmospheres* **102**, 16663-16682, doi:10.1029/97jd00237 (1997).
29 Huang, Y., Kok, J. F., Saito, M. & Munoz, O. Single-scattering properties of ellipsoidal dust aerosols constrained by measured dust shape distributions. *Atmospheric Chemistry and Physics* **23**, 2557-2577, doi:10.5194/acp-23-2557-2023 (2023).
30 Meng, J. *et al.* Improved Parameterization for the Size Distribution of Emitted Dust Aerosols Reduces Model Underestimation of Super Coarse Dust. *Geophysical Research Letters* **49**, doi:10.1029/2021gl097287 (2022).
31 Ryder, C. L. *et al.* Coarse and giant particles are ubiquitous in Saharan dust export regions and are radiatively significant over the Sahara. *Atmospheric Chemistry and Physics* **19**, 15353-15376, doi:10.5194/acp-19-15353-2019 (2019).
32 González-Flórez, C. *et al.* Insights into the size-resolved dust emission from field measurements in the Moroccan Sahara. *Atmospheric Chemistry and Physics* **23**, 7177-7212, doi:10.5194/acp-23-7177-2023 (2023).
33 Kok, J. F. A scaling theory for the size distribution of emitted dust aerosols suggests climate models underestimate the size of the global dust cycle. *Proc. Natl. Acad. Sci. U. S. A.* **108**, 1016-1021, doi:10.1073/pnas.1014798108 (2011).
34 Huang, Y., Adebiyi, A. A., Formenti, P. & Kok, J. F. Linking the different diameter types of aspherical desert dust indicates that models underestimate coarse dust emission. *Geophysical Research Letters* **48**, e2020GL092054, doi:https://doi.org/10.1029/2020GL092054 (2021).
35 Rodakoviski, R., Kok, J. & Chamecki, M. Dust Settling From Turbulent Layers in the Free Troposphere: Implications for the Saharan Air Layer. *Journal of Geophysical Research-Atmospheres* **128**, doi:10.1029/2022jd037724 (2023).

36 Huang, Y. *et al.* Climate Models and Remote Sensing Retrievals Neglect Substantial Desert Dust Asphericity. *Geophys. Res. Lett.* **47**, e2019GL086592, doi:https://doi.org/10.1029/2019GL086592 (2020).
37 Mallios, S. A., Drakaki, E. & Amiridis, V. Effects of dust particle sphericity and orientation on their gravitational settling in the earth's atmosphere. *Journal of Aerosol Science* **150**, doi:10.1016/j.jaerosci.2020.105634 (2020).
38 van der Does, M., Knippertz, P., Zschenderlein, P., Harrison, R. G. & Stuut, J. B. W. The mysterious long-range transport of giant mineral dust particles. *Science Advances* **4**, doi:10.1126/sciadv.aau2768 (2018).
39 Ukkonen, P., Pincus, R., Hogan, R., Nielsen, K. & Kaas, E. Accelerating Radiation Computations for Dynamical Models With Targeted Machine Learning and Code Optimization. *J. Adv. Model. Earth Syst.* **12**, doi:10.1029/2020MS002226 (2020).
40 Leung, D. *et al.* A global dust emission dataset for estimating dust radiative forcings in climate models. *Atmospheric Chemistry And Physics* **25**, 2311-2331, doi:10.5194/acp-25-2311-2025 (2025).
41 Kok, J. F., Ward, D. S., Mahowald, N. M. & Evan, A. T. Global and regional importance of the direct dust-climate feedback. *Nature Communications* **9**, doi:10.1038/s41467-017-02620-y (2018).
42 Stanelle, T., Bey, I., Raddatz, T., Reick, C. & Tegen, I. Anthropogenically induced changes in twentieth century mineral dust burden and the associated impact on radiative forcing. *Journal of Geophysical Research-Atmospheres* **119**, 13526-13546, doi:10.1002/2014jd022062 (2014).
43 Evan, A. T., Flamant, C., Gaetani, M. & Guichard, F. The past, present and future of African dust. *Nature* **531**, 493-495 (2016).
44 Pausata, F. S. R., Messori, G. & Zhang, Q. Impacts of dust reduction on the northward expansion of the African monsoon during the Green Sahara period. *Earth and Planetary Science Letters* **434**, 298-307, doi:10.1016/j.epsl.2015.11.049 (2016).
45 Evan, A. T., Foltz, G. R., Zhang, D. X. & Vimont, D. J. Influence of African dust on ocean-atmosphere variability in the tropical Atlantic. *Nature Geoscience* **4**, 762-765, doi:10.1038/ngeo1276 (2011).
46 Miller, R. L., Knippertz, P., Pérez García-Pando, C., Perlwitz, J. P. & Tegen, I. in *Mineral Dust: A Key Player in the Earth System* (eds Peter Knippertz & Jan-Berend W. Stuut) 327-357 (Springer Netherlands, 2014).
47 Dee, D. P. *et al.* The ERA-Interim reanalysis: configuration and performance of the data assimilation system. *Quarterly Journal of the Royal Meteorological Society* **137**, 553-597, doi:10.1002/qj.828 (2011).
48 Liou, K. N. *An Introduction to Atmospheric Radiation*. Second edn, (Academic Press, 2002).
49 Wiscombe, W. & Grams, G. Backscattered fraction in 2-stream approximations. *J. Atmos. Sci.* **33**, 2440-2451 (1976).
50 Seinfeld, J. H. & Pandis, S. N. *Atmospheric chemistry and physics: From air pollution to climate change*. (John Wiley & Sons, Inc., 1998).
51 Moosmüller, H. & Ogren, J. Parameterization of the Aerosol Upscatter Fraction as Function of the Backscatter Fraction and Their Relationships to the Asymmetry Parameter for Radiative Transfer Calculations. *Atmosphere* **8**, doi:10.3390/atmos8080133 (2017).
52 Randles, C. A. *et al.* The MERRA-2 Aerosol Reanalysis, 1980 Onward. Part I: System Description and Data Assimilation Evaluation. *Journal of Climate* **30**, 6823-6850, doi:10.1175/jcli-d-16-0609.1 (2017).

53 Newman, S., Smith, J., Glew, M., Rogers, S. & Taylor, J. Temperature and salinity dependence of sea surface emissivity in the thermal infrared. *Quarterly Journal of the Royal Meteorological Society* **131**, 2539-2557, doi:10.1256/qj.04.150 (2005).
54 Hulley, G. *et al.* The ASTER Global Emissivity Dataset (ASTER GED): Mapping Earth's emissivity at 100 meter spatial scale. *Geophysical Research Letters* **42**, 7966-7976, doi:10.1002/2015GL065564 (2015).
55 Yang, E. S., Gupta, P. & Christopher, S. A. Net radiative effect of dust aerosols from satellite measurements over Sahara. *Geophysical Research Letters* **36**, L18812, doi:10.1029/2009gl039801 (2009).
56 Mayer, B. & Kylling, A. Technical note: The libRadtran software package for radiative transfer calculations - description and examples of use. *Atmospheric Chemistry and Physics* **5**, 1855-1877, doi:10.5194/acp-5-1855-2005 (2005).
57 Emde, C. *et al.* The libRadtran software package for radiative transfer calculations (version 2.0.1). *Geoscientific Model Development* **9**, 1647-1672, doi:10.5194/gmd-9-1647-2016 (2016).
58 Myhre, G. *et al.* Cloudy-sky contributions to the direct aerosol effect. *Atmospheric Chemistry and Physics* **20**, 8855-8865, doi:10.5194/acp-20-8855-2020 (2020).
59 Bellouin, N. *et al.* Bounding Global Aerosol Radiative Forcing of Climate Change. *Reviews of Geophysics* **58**, 45, doi:10.1029/2019rg000660 (2020).
60 Hansell, R. *et al.* An assessment of the surface longwave direct radiative effect of airborne dust in Zhangye, China, during the Asian Monsoon Years field experiment (2008). *Journal of Geophysical Research-Atmospheres* **117**, doi:10.1029/2011JD017370 (2012).
61 Osborne, S. *et al.* Short-wave and long-wave radiative properties of Saharan dust aerosol. *Quarterly Journal of the Royal Meteorological Society* **137**, 1149-1167, doi:10.1002/qj.771 (2011).
62 Haywood, J. *et al.* Radiative properties and direct radiative effect of Saharan dust measured by the C-130 aircraft during SHADE: 1. Solar spectrum. *Journal of Geophysical Research-Atmospheres* **108**, doi:10.1029/2002jd002687 (2003).
63 Hansell, R. *et al.* An Assessment of the Surface Longwave Direct Radiative Effect of Airborne Saharan Dust during the NAMMA Field Campaign. *J. Atmos. Sci.* **67**, 1048-1065, doi:10.1175/2009JAS3257.1 (2010).
64 Efron, B. *The jackknife, the bootstrap, and other resampling plans*. (Capital City Press, 1982).
65 Chernick, M. R. *Bootstrap methods : a guide for practitioners and researchers*. 400 (Wiley-Interscience, 2007).
66 Meloni, D. *et al.* Determining the infrared radiative effects of Saharan dust: a radiative transfer modelling study based on vertically resolved measurements at Lampedusa. *Atmospheric Chemistry and Physics* **18**, 4377-4401, doi:10.5194/acp-18-4377-2018 (2018).
67 Zhang, J. L. & Christopher, S. A. Longwave radiative forcing of Saharan dust aerosols estimated from MODIS, MISR, and CERES observations on Terra. *Geophysical Research Letters* **30**, 4, doi:10.1029/2003gl018479 (2003).
68 Christopher, S. & Jones, T. Satellite-based assessment of cloud-free net radiative effect of dust aerosols over the Atlantic Ocean. *Geophysical Research Letters* **34**, doi:10.1029/2006GL027783 (2007).
69 Hsu, N., Herman, J. & Weaver, C. Determination of radiative forcing of Saharan dust using combined TOMS and ERBE data. *Journal of Geophysical Research-Atmospheres* **105**, 20649-20661 (2000).
70 Huang, J. *et al.* Taklimakan dust aerosol radiative heating derived from CALIPSO observations using the Fu-Liou radiation model with CERES constraints. *Atmospheric Chemistry and Physics* **9**, 4011-4021 (2009).

71 Haywood, J. *et al.* Observations and modelling of the solar and terrestrial radiative effects of Saharan dust: a radiative closure case-study over oceans during the GERBILS campaign. *Quarterly Journal of the Royal Meteorological Society* **137**, 1211-1226, doi:10.1002/qj.770 (2011).
72 Brindley, H. Estimating the top-of-atmosphere longwave radiative forcing due to Saharan dust from satellite observations over a west African surface site. *Atmos. Sci. Lett.* **8**, 74-79, doi:10.1002/asl.155 (2007).
73 Kuwano, A., Evan, A., Walkowiak, B. & Frouin, R. Quantifying the dust direct radiative effect in the southwestern United States: findings from multiyear measurements. *Atmospheric Chemistry and Physics* **24**, 9843-9868, doi:10.5194/acp-24-9843-2024 (2024).
74 Pu, B. & Ginoux, P. How reliable are CMIP5 models in simulating dust optical depth? *Atmospheric Chemistry and Physics* **18**, 12491-12510, doi:10.5194/acp-18-12491-2018 (2018).
75 di Sarra, A. *et al.* Shortwave and longwave radiative effects of the intense Saharan dust event of 25-26 March 2010 at Lampedusa (Mediterranean Sea). *Journal of Geophysical Research-Atmospheres* **116**, doi:10.1029/2011JD016238 (2011).
76 Meloni, D. *et al.* Altitude-resolved shortwave and longwave radiative effects of desert dust in the Mediterranean during the GAMARF campaign: Indications of a net daily cooling in the dust layer. *Journal of Geophysical Research-Atmospheres* **120**, 3386-3407, doi:10.1002/2014JD022312 (2015).
77 Stevens, B. Rethinking the Lower Bound on Aerosol Radiative Forcing. *J. Climate* **28**, 4794-4819, doi:10.1175/jcli-d-14-00656.1 (2015).
78 Mahowald, N., Li, L., Albani, S., Hamilton, D. & Kok, J. Opinion: The importance of historical and paleoclimate aerosol radiative effects. *Atmospheric Chemistry and Physics* **24**, 533-551, doi:10.5194/acp-24-533-2024 (2024).

Supplementary Information for "Desert dust exerts a substantial longwave radiative forcing missing from climate models"

Jasper F. Kok[1,*], Ashok. K. Gupta[1], Amato T. Evan[2], Adeyemi A. Adebiyi[3], Samuel Albani[4], Yves Balkanski[5], Ramiro Checa-Garcia[6], Peter R. Colarco[7], Douglas Hamilton[8], Yue Huang[1], Akinori Ito[9], Martina Klose[10], Longlei Li[11], Natalie M. Mahowald[11], Ron L. Miller[12], Vincenzo Obiso[13], Carlos Pérez García-Pando[13,14], Adriana Rocha Lima[15], Jessica Wan[2]

[1]Department of Atmospheric and Oceanic Sciences, University of California, Los Angeles, CA 90095, USA
[2]Scripps Institution of Oceanography, University of California, San Diego, CA 92093
[3]Department of Life and Environmental Sciences, University of California, Merced, CA, 95344, USA
[4]Department of Environmental and Earth Sciences, University of Milano-Bicocca, Milano, Italy
[5]Laboratoire des Sciences du Climat et de l'Environnement, CEA-CNRS-UVSQ-UPSaclay, Gif-sur-Yvette, France
[6]Royal Netherlands Meteorological Institute, De Bilt, the Netherlands
[7]Atmospheric Chemistry and Dynamics Laboratory, NASA Goddard Space Flight Center, Greenbelt, MD 20771, USA
[8]Marine, Earth, and Atmospheric Science, North Carolina State University, Raleigh, NC, 27606
[9]Yokohama Institute for Earth Sciences, JAMSTEC, Yokohama, Kanagawa 236-0001, Japan
[10]Institute of Meteorology and Climate Research Troposphere Research, Karlsruhe Institute of Technology (KIT), Karlsruhe, Germany
[11]Department of Earth and Atmospheric Sciences, Cornell University, Ithaca, NY, 14850, USA.
[12]NASA Goddard Institute for Space Studies, New York NY10025 USA
[13]Barcelona Supercomputing Center (BSC), 08034 Barcelona, Spain
[14]ICREA, Catalan Institution for Research and Advanced Studies, 08010 Barcelona, Spain
[15]Department of Physics, University of Maryland, Baltimore County, 1000 Hilltop Circle, Baltimore, MD, 21250, USA
[*]Corresponding author: jfkok@ucla.edu

Supplementary Methods

Below, we describe the DustCOMM dust climatology data set, the various effective emission temperatures used in the analytical model, how the radiative transfer calculations of the atmospheric absorptivity were performed, how the bootstrap procedure was performed, and the treatment of longwave interactions in our ensemble of six global model simulations that were also used in obtaining the DustCOMM data set. We end with a discussion of the limitations of our methodology.

DustCOMM dust climatology data set. One of the main data sets used in the analytical model is the Dust Constraints from joint Observational-Modelling-Experimental analysis (DustCOMM) data set. Details on this data set can be found in various recent publications[1-4] and we provide a brief overview here. DustCOMM is a climatology of the global dust cycle obtained for the years 2004-2008. It provides constraints on the main properties of the global dust cycle, including dust concentration, dust aerosol optical depth, and dust deposition fluxes. All these variables are resolved by season, particle size (up to a diameter of 20 μm), and the emitting major source region.

The DustCOMM data set was produced using inverse modeling, which integrated an ensemble of simulations from six global models (listed in table 1 in Kok et al.[3] and also in Table S3) with observational constraints on the dust size distribution[1], extinction efficiency[5], and regional dust aerosol optical depth near dust source regions[2,6]. The DustCOMM data include uncertainties, which were obtained through a bootstrap procedure[7] that propagated uncertainty from the spread in the model simulations, uncertainties in observed dust microphysical properties, and uncertainties in the regional DAOD. Comparisons against dust surface concentration and deposition flux measurements indicated that DustCOMM is in substantially better agreement with these independent measurements than current model simulations[3].

For this paper, we used three products from the DustCOMM data set (Fig. S1). First, we used the dust concentration, resolved by location, particle size, and season, which we combined with data sets of the dust LW refractive index (Table S6) to calculate the LW dust aerosol optical depth (Fig. S9) and ultimately the dust clear-sky LW DRE. Second, we used the SW DAOD, which we combined with the clear-sky LW DRE to calculate the clear-sky LW DREE, which we then compared against observations. Note that some of the model simulations used in DustCOMM assumed that the clear-sky SW DAOD equals the all-sky SW DAOD, which could cause errors, although studies indicate that such a systematic difference is small for dusty regions[6,8]. And finally, we used the ratio of the clear-sky to the all-sky LW DRE from the six models used in the DustCOMM data set, which we combined with the clear-sky LW DRE calculated by the data-driven analytical model to obtain the all-sky LW DRE.

Effective emission temperatures. We define the effective emission temperature as the temperature that a blackbody would need to have to emit the same radiative flux in the atmospheric window (taken as 8-14 μm). The effective emission temperature T_{d} (Fig. S11e) of dust in an atmospheric column is then

$$T_{\mathrm{d}} = \left[\frac{1}{f_{\mathrm{aw}}(T_{\mathrm{d}})} \frac{\sum_{i=1}^{N_{\mathrm{i}}} \bar{\tau}_{\mathrm{d},i} f_{\mathrm{aw}}(T_i) T_i^4}{\sum_{i=1}^{N_i} \bar{\tau}_{\mathrm{d},i}}\right]^{\frac{1}{4}}, \tag{S17}$$

where f_{aw} (Fig. S12) is the fraction of the emitted radiative flux with wavelength in the atmospheric window, the index i sums over the $N_i = 48$ pressure levels in the DustCOMM data set spanning from sea level to the top-of-atmosphere, and T_i is the atmospheric temperature at the center of each pressure level, which is supplied by MERRA-2 reanalysis data[9]. For simplicity, equation (S1) assumes that the total column dust optical depth τ_d << 1, such that a weighting function to calculate the fraction of radiation from each model level that transmits to the top of the dust layer is not needed; the impact of the assumption of τ_d << 1 is discussed further below. In addition, $\bar{\tau}_{\mathrm{d},i}$ is the optical thickness (unitless) of dust in layer i, which is calculated as

$$\bar{\tau}_{\mathrm{d},i} = \sum_{b=1}^{N_b} l_{i,b}\, \bar{k}_{\mathrm{ext},b}, \tag{S18}$$

where b sums over the N_b dust particle bins (Table S4), which include the bins spanning until 20 µm diameter in the DustCOMM product[3] and three more bins that account for dust with diameter between 20 – 100 µm based on CESM simulations calibrated to in situ measurements of super coarse dust[10,11]. Furthermore, $l_{i,b}$ is the mass path (kg m^{-2}) of bin b in vertical model layer i, and $\bar{k}_{\mathrm{ext},b}$ is each bin's mass extinction efficiency (m^2 kg^{-1}) in the atmospheric window, which was obtained as described below and listed in Table S4.

We similarly define the effective emission temperature of upwelling atmospheric radiation below the dust layer (T_{bel}) and of downwelling radiation above the dust layer (T_{abv}) as the temperature that a blackbody would need to have to produce the same radiative flux in the atmospheric window. That is,

$$T_{\mathrm{bel}} = \left[\frac{1}{f_{\mathrm{aw}}(T_{\mathrm{bel}})} \frac{\sum_{i=1}^{i_{\mathrm{d}}-1} \bar{\epsilon}_{\mathrm{atm},i} f_{\mathrm{aw}}(T_i) T_i^4}{\sum_{i=1}^{N_i} \bar{\epsilon}_{\mathrm{atm},i}}\right]^{\frac{1}{4}}, \text{ and} \tag{S19}$$

$$T_{\mathrm{abv}} = \left[\frac{1}{f_{\mathrm{aw}}(T_{\mathrm{abv}})} \frac{\sum_{i_d+1}^{N_i} \bar{\epsilon}_{\mathrm{atm},i} f_{\mathrm{aw}}(T_i) T_i^4}{\sum_{i=1}^{N_i} \bar{\epsilon}_{\mathrm{atm},i}}\right]^{\frac{1}{4}}, \tag{S20}$$

where $\bar{\epsilon}_{\mathrm{atm},i}$ is the absorptivity due to atmospheric constituents in model layer i below the dust layer's central model layer i_{d}, calculated using a radiative transfer model (see below); T_{bel} is typically one to ten degrees colder than T_{s}.

The effective emission temperature below the dust layer, $T_{\mathrm{s,eff}}$ (Fig. S11c), depends primarily on the surface temperature T_{s} (Fig. S11a) and surface emissivity ϵ_{s} (Fig. S11b); $T_{\mathrm{s,eff}}$ - T_{s} can be up to ~5 °C in desert regions with relatively small ϵ_{s} (Figs. S11b, S11d). The effective emission temperature is defined as

$$T_{\mathrm{s,eff}} = \left[\frac{(1-\bar{\epsilon}_{\mathrm{bel}})}{f_{\mathrm{aw}}(T_{\mathrm{s,eff}})}\left[\bar{\epsilon}_{\mathrm{s}} f_{\mathrm{aw}}(T_{\mathrm{s}}) T_{\mathrm{s}}^4 + (1-\bar{\epsilon}_{\mathrm{s}}) f_{\mathrm{aw}}(T_{\mathrm{atm}\downarrow}) T_{\mathrm{atm}\downarrow}^4\right] + \frac{f_{\mathrm{aw}}(T_{\mathrm{bel}})}{f_{\mathrm{aw}}(T_{\mathrm{s,eff}})} \bar{\epsilon}_{\mathrm{bel}} T_{\mathrm{bel}}^4\right]^{\frac{1}{4}}, \tag{S21}$$

where $T_{\mathrm{atm}\downarrow}$ is the effective emission temperature of downwelling radiation at the surface (generally, $T_{\mathrm{atm}\downarrow} < T_s$). The three terms in Eq. (S5) respectively represent the contributions of upwelling radiation emitted by the surface, of the downwelling atmospheric radiation scattered upward by the surface, and of the upwelling radiation emitted by the atmosphere between the surface and the dust layer.

Finally, the effective emission temperature of downwelling radiation at the surface equals

$$T_{\text{atm}\downarrow} = \left[\frac{1}{f_{\text{aw}}(T_{\text{atm}\downarrow})}\left[\bar{\epsilon}_{\text{bel}} f_{\text{aw}}(T_{\text{bel}}) T_{\text{bel}}^4 + (1-\bar{\epsilon}_{\text{bel}}-\bar{\epsilon}_{\text{d}})\bar{\epsilon}_{\text{abv}} f_{\text{aw}}(T_{\text{abv}}) T_{\text{abv}}^4 + (1-\bar{\epsilon}_{\text{bel}})\bar{\epsilon}_{\text{d}} f_{\text{aw}}(T_{\text{d}}) T_{\text{d}}^4 + (1-\bar{\epsilon}_{\text{bel}}) f_{\text{aw}}(T_{\text{s,eff}}) T_{\text{s,eff}}^4 R_d\right]\right]^{\frac{1}{4}}, \quad \text{(S22)}$$

where the first two of the four terms inside the square brackets respectively represents the contributions from the atmosphere below and above the dust layer, the third term represent the contribution of emission from the dust layer, and the fourth term represents the (relatively small) contribution of upwelling radiation below the dust layer that is scattered down towards Earth's surface by the dust layer.

Dust optical properties. The optical properties in the LW spectrum are quite uncertain, in large part because of a scarcity of measurements. Correspondingly, values of the refractive index in the longwave spectrum used in different models and theoretical studies vary greatly, as summarized in Di Biagio et al.[12]. Considering this large divergence, we draw from six different LW refractive index data sets in common use in the literature[12-17]. For each of these data sets, we obtained the complex refractive index averaged over the atmospheric window (Table S6). We then calculated the mass extinction efficiency, downscatter fraction, and single-scattering albedo for each bin b ($\bar{k}_{\text{ext},b}$, $\bar{\beta}_{\downarrow,b}$, and $\bar{\omega}_b$, respectively) as

$$\bar{k}_{\text{ext},b} = \frac{\int_{D_{b-}}^{D_{b+}} \frac{dN}{dD}\frac{\pi}{4}D^2\, \bar{Q}_{\text{ext}}(D)dD}{\int_{D_{b-}}^{D_{b+}} \frac{dN}{dD}\frac{\pi}{6}D^3 \rho_{\text{d}} dD}, \quad \text{(S23)}$$

$$\bar{\beta}_{\downarrow,b} = \frac{\int_{D_{\text{min},b}}^{D_{b+}} \frac{dN}{dD}\frac{\pi}{4}D^2\, \bar{Q}_{\text{scat}}(D)\bar{\beta}_{\downarrow}(D)dD}{\int_{D_{b-}}^{D_{b+}} \frac{dN}{dD}\frac{\pi}{4}D^2\, \bar{Q}_{\text{scat}}(D)dD}, \quad \text{(S24)}$$

$$\bar{\omega}_b = \frac{\int_{D_{b-}}^{D_{b+}} \frac{dN}{dD}\frac{\pi D^2}{4}\, \bar{Q}_{\text{ext}}(D)\bar{\omega}(D)dD}{\int_{D_{b-}}^{D_{b+}} \frac{dN}{dD}\frac{\pi}{4}D^2\, \bar{Q}_{\text{ext}}(D)dD}, \quad \text{(S25)}$$

where D_{b-} and D_{b+} are respectively the lower and upper diameter limits of particle size bin k, $\rho_d = (2.5 \pm 0.2) \times 10^3$ kg m^{-3} is the globally representative density of dust aerosols[18-21], and $\frac{dN}{dD}$ is the observationally constrained globally averaged dust number size distribution obtained in Adebiyi and Kok[1]. Furthermore, $\bar{Q}_{\text{scat}}(D)$, $\bar{Q}_{\text{ext}}(D)$, $\bar{\beta}_{\downarrow}(D)$ and $\bar{\omega}(D)$ are respectively the size-resolved scattering efficiency, extinction efficiency, downscatter fraction, and single-scattering albedo. Note that the exact values of these optical properties for a given model bin vary for each bootstrap iteration (explained further below) as they depend on which of the complex refractive indices in Table S6 was drawn in the bootstrap procedure as well on which realization of the sub-bin dust size distribution was drawn from the ensemble of possible global dust size distributions provided in Adebiyi and Kok[1].

Table S4 reports the mean values and standard deviation of the mass extinction efficiency ($\bar{k}_{\text{ext},b}$), downscatter fraction ($\bar{\beta}_{\downarrow,b}$), and single-scattering albedo ($\bar{\omega}_b$) for each bin. Variability in these optical properties for a given particle bin are due to variability in the sub-bin dust size distribution [see Eqs. (S7)-(S9)], and in the dust complex refractive index in the atmospheric window, based on a random drawing of one of six data sets (see Table S6).

Note that the optical properties calculated by Eqs. (S7)-(S9) neglect the effect of dust asphericity. This is necessary because there are no optical properties available for aspherical dust for the broad range of complex refractive indices used in this study (Table S5), necessitating the use of Mie theory and therefore the assumption of spherical dust particles. The main effect of neglecting dust asphericity is an underestimation of the mass extinction efficiency by ~40% in both the SW[5] and LW spectra[22]. In other words, asphericity has a minimal effect on the ratio of the LW to the SW DAOD (Fig. S13), which co-determines the LW radiative effects (Eq. 13) because the main constraint on the size of the global dust cycle is the SW DAOD[3]. For consistency, we therefore also neglected the effect of asphericity in the SW spectrum. That is, we obtained the DustCOMM data as described in Kok et al.[3], except that we used optical properties in the SW spectrum obtained from Mie theory with the SW complex refractive index used in Kok et al.[5]. Because dust abundance in the DustCOMM climatology is constrained by the SW DAOD[6], this results in an enhancement of the global dust mass loading by ~40%, which almost exactly counteracts the reduction in LW DAOD that would be caused by neglecting the asphericity on LW optical properties only. As such, the effect of neglecting asphericity on the results reported in this paper is expected to induce an error that is small compared to other errors in the analysis (see discussion of limitations below).

Radiative transfer model simulations of atmospheric absorptivity. To assess the spatial and temporal variations of average atmospheric absorptivity ($\bar{\epsilon}_{\mathrm{atm}}$ and $\bar{\epsilon}_{\mathrm{abv}}$) and downwelling atmospheric temperature ($T_{\mathrm{atm}\downarrow}$) for clear-sky conditions within the 8–14 µm wavelength range, we employed the LibRadtran radiative transfer model[23,24]. Atmospheric profiles of water vapor, ozone, pressure, temperature, and air density were obtained from MERRA-2 reanalysis data[9] and were interpolated onto the grid used for DustCOMM[3]. Additionally, we used seasonal mean climatological values for trace gases, including CO_2, O_2, CH_4, and NO_2, from the Air Force Geophysics Laboratory (AFGL)[25] to represent background concentrations appropriate for radiative transfer simulations[23]. These three-dimensional atmospheric profiles of greenhouse gas concentrations, temperature, and pressure were then utilized as inputs for LibRadtran[24].

The model was configured to simulate thermal radiation specifically within the 8–14 µm atmospheric window, where water vapor, ozone, and CO_2 are the predominant absorbers. For the simulations, the six streams DISORT solver was used to perform accurate multi-layer radiative transfer calculations, while the REPTRAN molecular absorption parameterization was applied to achieve detailed spectral resolution[26,27]. These calculations were conducted over the period from 2004 to 2008, for which the DustCOMM dust climatology was obtained.

Bootstrap procedure to propagate uncertainties. In order to propagate the uncertainties in the inputs to our data-driven analytical model (orange boxes in Fig. S1), we used the following bootstrap procedure[28,29]:

1. We randomly choose one the many realizations of the global dust cycle in the DustCOMM data set[3]. These realizations were themselves obtained from a bootstrap procedure that propagated uncertainties due to inputs to the DustCOMM data set, including on DAOD in 15 dusty regions[2,6], the globally averaged atmospheric dust

particle size distribution in the atmosphere[1], and the spread between the six global model simulations used in the DustCOMM inversion method.

2. We randomly drew a complex refractive index representative of the atmospheric window from the six available data sets (Table S6) and used it to calculate the LW optical properties ($\overline{\omega}_b$, $\bar{\beta}_{\downarrow,b}$, and $\bar{k}_{\text{ext},b}$).
3. Using this realization of the global dust cycle and the LW optical properties, we calculated the seasonally and spatially resolved LW clear-sky DRE at TOA, using the data-driven analytical model.
4. We calculated the root mean-squared error (RMSE) of the simulated LW clear-sky DREE relative to the compilation of LW DREE observations (Table S5). If the RMSE was larger than RMSE_{max} = 4 Wm^{-2} (see Methods) then the bootstrap iteration was reinitialized at step 1. This resulted in the elimination of ~55% of the simulations, retaining the other ~45% (Extended Data Fig. 2).
5. We randomly drew one of the six global model simulations used in the DustCOMM data set and obtained $\eta(s, \theta, \phi)$, the spatially and seasonally resolved ratio of the simulated LW clear-sky DRE and LW all-sky DRE. We then used this to calculate the seasonally and spatially resolved LW all-sky DRE (see Eq. 12 in Methods).

We repeated the above steps 1,000 times, yielding a large number of realizations that represent the probability distributions of the LW clear-sky and all-sky DRE, with the spread in these probability distributions representing the uncertainty due to the propagation of the various uncertainties in the input data to our procedure. We report the median and 90% confidence interval of these results in the main text. Because our procedure cannot propagate systematic errors due to limitations of our method, which are discussed in more detail below, the errors should be interpreted as a lower bound.

Treatment of LW interactions in the six global aerosol models. Below, we describe the treatment of LW interactions of each of the six models used in the DustCOMM inversion method, namely CESM/CAM4, IMPACT, GISS Model E2.1, GEOS/GOCART, MONARCH, and LMDZOR-INCA. Other details of these simulations can be found in the Supplement to Kok et al.[3]. The seasonal LW DREE simulated by each model is shown in Fig. S14, with the comparison against the compilation of LW DREE observations (Table S5) shown in Fig. 2b.

CESM. We use simulations with the Community Atmosphere Model version 4 (CAM4) within the Community Earth System Model version 1 (CESM1), which includes active atmosphere, land, and sea ice components, alongside a data ocean and slab glacier forced by MERRA2 meteorology. CAM4 utilizes the Bulk Aerosol Model (BAM) parameterization for dust size distribution[30], where emission fluxes are partitioned into four size bins (diameters: 0.1-1.0, 1.0-2.5, 2.5-5.0, 5.0-10 μm)[31]. Dust emissions in these bins follow the brittle fragmentation theory[32].

CAM4's longwave radiation scheme uses an absorptivity/emissivity formulation[33] that neglects aerosol scattering. A seven-band broadband approach is used, which accounts for water vapor window regions[34]. The longwave optical properties of dust in CAM4 are inherited from CAM3[31,35] and are based on Maxwell-Garnett mixing of 47.6% quartz, 25% illite, 25% montmorillonite, 2% calcite, and 0.4% hematite by volume. The prescribed dust density and hygroscopicity are 2500 kg m^{-3} and 0.14, respectively. To account for longwave aerosol scattering, the longwave dust direct radiative effect at the top of the atmosphere is scaled up by the maximum reported error of approximately 50%[36].

The cloud parameterization in CAM 4.0 diagnoses cloud fraction based on relative humidity, atmospheric stability, water vapor, and convective mass fluxes[37]. It categorizes clouds into three types: low-level marine stratocumulus, convective clouds, and layered clouds. Marine stratocumulus clouds are determined using empirical relationships involving potential temperature differences[38], while convective clouds are linked to updraft mass fluxes from deep and shallow cumulus schemes[39]. Layered clouds form when relative humidity exceeds a pressure-dependent threshold, with adjustments made to account for land-surface variability and cold climates to avoid unrealistic cloud decks[40]. The total cloud fraction combines these cloud types under a maximum overlap assumption, ensuring consistency between cloud fraction, condensate, and relative humidity.

IMPACT. This study used the Integrated Massively Parallel Atmospheric Chemical Transport (IMPACT) model to calculate the concentration of mineral dust aerosols in 4 size bins (diameters: 0.1–1.26, 1.26–2.5, 2.5–5, and 5–20 μm) (Ito et al.[41] and references therein), as in Kok et al.[3]. Emitted dust particles were distributed among these four bins following brittle fragmentation theory[32]. We used an off-line radiative transfer model to calculate the optical depth of mineral dust particles per layer and their resulting radiative effects (Ito et al., 2018 and references therein). The radiative parameterizations include effects of clouds based on the National Center for Atmospheric Research (NCAR) Community Atmosphere Model 3[43]. In this study, the off-line radiative transfer model estimated LW radiative effect based on CAM4 and thus scattering of longwave radiation by dust was neglected (Albani et al.[44] and references therein). In the off-line radiative transfer model, the mineral dust particles were treated as externally mixed in each size bin, and thus the water uptake by dust particles was neglected. The aerosol optical properties were calculated using a look-up table as a function of wavelength and size parameter[45]. Here, we updated the refractive indices for mineral dust particles. The LW refractive indices were derived from averages of in situ measurements over 9 regions[12]. The dust radiative effect is estimated for each region and each size bin as the difference in the calculated radiative fluxes with all dust particles and with all dust particles except the size bin for the region being estimated in the calculation[46]. Thus, 5 simulations were conducted for each 9 regions with each refractive index. The results in Figure S14 show the resulting radiative effects from the summation over each bin and region.

GISS Model E2.1. The distribution of dust aerosols and their radiative impact is calculated here using the One Moment Aerosol (OMA) version of the NASA Goddard Institute for Space Sciences Earth System ModelE2.1[47,48] that has horizontal resolution of 2° latitude by 2.5° longitude and 40 vertical layers that extend to 0.1 hPa, just above the stratopause. The dust simulations described here are the same as analyzed by Kok et al.[3]. Further model description is given by Miller at al.[49] and Perlwitz et al.[50].

Dust sources are identified as arid lowlands[51], where dust emission increases with wind speed, while being inhibited by soil moisture[52]. Emission also increases with parameterized wind gustiness[53]. Transport occurs within five size classes (with diameters 0.1-2 μm, 2-4 μm, 4-8 μm, 8-16 μm and 16-32 μm, respectively). We did not use the largest bin (16-32 μm) because it exceeds the 20 μm maximum diameter used in the inverse model and instead generated a 16-20 μm bin based on the 8-16 μm bin and the GEOS/GOCART simulations, as described in Kok et al.[3]. The emitted ratio of clay (dust with $D < 2$ μm) and silt (dust with $D \geq 2$ μm) particles was prescribed to match retrievals of the aerosol size distribution at AERONET stations in dusty regions of high dust concentration, which resulted in a ratio consistent with measurements of the emitted size distribution compiled by Kok[32].

Model winds were nudged toward NCEP reanalysis values four times daily with a 1000-second relaxation time that was chosen to reproduce the magnitude of observed convergence. Dust is removed from the atmosphere by gravitational settling, turbulence within the surface layer and wet deposition. The latter includes below-cloud scavenging by precipitation with potential reevaporation, and in-cloud scavenging by nucleation, assuming that dust particles have a solubility of fifty percent, based upon explicit simulation of heterogeneous chemistry on dust particles[54].

The dust radiative effect is calculated from external mixtures of the size bins. The complex refractive index (CRI) for dust is prescribed at solar wavelengths assuming two equal external mixtures whose CRI is taken from retrievals by Sinyuk et al.[55] and Patterson et al.[56], respectively. At thermal wavelengths, the CRI is prescribed from measurements by Volz[14]. Longwave scattering is not explicitly calculated but its effect is approximated by increasing the total extinction by 30 percent[57], based upon calculations by Dufresne et al.[36]. Water coatings on dust particles by deliquescence and its radiative effect through particle radius is neglected.

The ModelE2.1 version of OMA represents only the first aerosol indirect effect[58], where aerosols influence cloud droplet number (CDN), which impacts cloud droplet size and optical thickness. The CDN at cloud base is specified from empirical relations based upon aerosol number and updraft speed[59]. The combined direct and indirect radiative effect of all aerosols in ModelE2.1 OMA is near -1 W/m2 in 2014[60], near the center of the range estimated by the Sixth Assessment Report of the Intergovernmental Panel on Climate Change[61].

Non-dust aerosols are prescribed in these simulations using monthly varying concentrations taken from separate OMA simulations of the CMIP6 historical period (1850-2014) with SST and sea ice prescribed from observations. This model version was subsequently found to have specified an erroneous particle radius for volcanic aerosols. While this distorted the stratospheric response following eruptions, the effect of this error on surface climate is small, as shown by comparisons with a corrected OMA version[60].

ModelE2.1 and other models in this study are used to calculate how clouds modify the clear-sky LW DRE, resulting in its all-sky counterpart. ModelE2.1 clouds are either convective or stratiform[62,63]. Convective clouds consist of two updrafts rising to their level of neutral buoyancy: one deep and undilute with the other diluted by entrainment of environmental air. Downdrafts created by detraining cloudy air and reevaporating moisture are also present[63]. The optical depth of each cloud type depends upon condensed vapor, which is prognostic, along with precipitate[62,64]. While the areal fraction of each cloud type is calculated, radiative fluxes are computed assuming that the layer is either entirely cloudy or else clear. A random number from a uniform distribution between zero and one is generated at each time step for both convective and stratiform clouds and the cloud is assumed to impact radiation at all levels where its calculated fraction exceeds this number[65]. Thus, while radiative fluxes will differ at any single time step from those calculated assuming partial coverage, the climatological average will be the same because the partial coverage is emulated by the fractional occurrence of full coverage. This method of stochastic occurrence is computationally more efficient than assuming partial coverage because, in the former case, the radiative fluxes are calculated for only one grid box type: either clear or else cloudy.

GEOS/GOCART. Simulations performed with the Goddard Earth Observing System (GEOS) global Earth system model ran the Goddard Chemistry, Aerosol, Radiation, and Transport (GOCART) aerosol module [66,67]. GOCART simulates the dust particle size distribution in five non-interacting size bins (diameters: 0.2 – 2, 2 – 3.6, 3.6 – 6, 6 – 12, 12 – 20 μm). Dust emissions use an updated version of the scheme described in Ginoux et al.[51], where dust vertical flux is a function of the surface wind speed, soil moisture, and a topographically weighted source function. Emissions are distributed across our five size bins using the brittle fragmentation theory of Kok[68]. Dust optical properties are as described in Colarco et al.[69], assuming a spheroidal shape distribution and LW refractive indices compiled from various observational measurements as described in Koepke et al.[70] and synthesized in the OPAC database[16]. GEOS uses the Rapid Radiative Transfer Model for GCMs (RRTMG, Ref. [71]) for its LW internal radiative transfer, which uses 16 bands spanning 3.08 – 1000 μm in wavelength space. The GEOS implementation of RRTMG does not account for longwave scattering on aerosols, so that in addition to extinction due to gas absorption there is extinction also due to aerosol absorption. Prognostic water and ice clouds in the GEOS AGCM are from Bacmeister et al.[72] as modified with a sub-grid PDF distribution of humidity-related fields after Molod[73]. See Molod et al.[74] for additional details.

MONARCH. The Multiscale Online Non-hydrostatic AtmospheRe CHemistry (MONARCH) model, developed at the Barcelona Supercomputing Center[75-77], incorporates advanced chemistry and aerosol packages, including a comprehensive representation of the dust cycle. MONARCH is coupled online with the Non-hydrostatic Multiscale Model (NMMB)[78], providing a fully interactive framework for atmospheric composition and weather and climate simulations.

MONARCH employs the RRTMG (Rapid Radiative Transfer Model for GCMs) scheme[71] to compute shortwave and longwave radiative fluxes and associated heating rates using the correlated-k approach. The longwave component (RRTMG_LW) calculates fluxes across sixteen contiguous spectral bands spanning 3.08–1000 μm. Molecular absorbers considered in the model include water vapor, carbon dioxide, ozone, nitrous oxide, methane, oxygen, nitrogen, and several halocarbons (CFC-11, CFC-12, CFC-22, and CCl_4). Except for water vapor, which is computed online, all other gas concentrations are prescribed from climatological datasets in these simulations.

In RRTMG_LW, scattering is not explicitly modeled for either clouds or aerosols; instead, only extinction due to absorption is accounted for. The optical properties of clouds are parameterized per spectral band, following Hu and Stamnes[79] for water clouds and Fu et al.[80] for ice clouds. Cloud fields are treated as grid-mean quantities without sub-grid variability, assuming a maximum-random cloud overlap configuration.

The dust module in MONARCH includes eight size transport bins, encompassing particles up to 20 μm in diameter, with the mass fraction of emitted dust in each bin parameterized following brittle fragmentation theory[32]. Dust particles are assumed to be externally mixed within each size bin, with no water uptake considered. While SW radiative interactions incorporate dust mineralogy-based refractive indices and non-spherical particle shapes, the LW component assumes spherical dust particles and utilizes refractive indices from the Optical Properties of Aerosols and Clouds (OPAC) dataset[16].

LMDZOR-INCA. Dust aerosol is represented by four modes in LMDZOR-INCA that cover aerosol diameters from 0.01 to 100 μm[81,82]. The prescribed size distribution of dust at emission is partitioned among the four modes (0.57%, 4.2%, 30.8%, 62.4%), which ensures consistency with Kok et al.[5] and measurements from the Fennec field campaign Experiment[83]. In the present study, the outputs from the dust simulations were reprojected on five bins up to a diameter of 20 µm as listed in Table S4 and discussed in Kok et al.[3].

The radiative transfer code that describes the longwave portion of the spectrum consists of 16 bands with wavelengths that span from 3.33 to 1,000 µm. This radiative transfer code, the Rapid Radiative Transfer Model (RRTM), was developed at the European Centre for Medium-Range Weather Forecasts[84]. No corrections were applied to these results to account for scattering in the longwave, which is not accounted for in the radiative transfer code[85]. For each of these bands, optical parameters are read from lookup tables according to the particle diameter. Dust is considered externally mixed with regards to the aerosol components and has no affinity with water. The refractive index in the longwave spectrum was taken from the compilation of measurements from Di Biagio et al.[12]. Dust longwave radiative effects are computed for each band and each dust mode (or bin equivalent) of the size distribution through a double call to the radiation code, one in which dust is present and another one when dust concentrations are set to zero. Results are shown in Figure 2b for the summation of all five bins for the season and over the area for which measurements were reported.

Within LMDZ[86] cloud cover and cloud water content are computed using a statistical scheme using a lognormal function for deep convection[87] and a bigaussian function for shallow cumulus[88]. Cloud droplet and crystal number concentrations are diagnosed afterward for the radiation scheme only. In particular, the first indirect effect, due to soluble aerosols, is restricted to liquid clouds and to the liquid fraction of mixed clouds, whereas the effective sizes of ice crystals are those of the RRTM scheme as implemented in the ECMWF mode[86].

Correction of observed LW clear-sky DREE values to diurnally and seasonally averaged values.

Because the predictions of our data-driven analytical model are diurnally and seasonally averaged, we corrected measurements in our compilation of LW clear-sky DREE observations (Table S5) as follows:

$$\widetilde{\Omega}_{\mathrm{obs},i} = \Omega_{\mathrm{obs},i} \frac{\widetilde{\Omega}_{\mathrm{mdl},i}}{\Omega_{\mathrm{mdl},i}}, \tag{S26}$$

where $\Omega_{\mathrm{obs},i}$ denotes one of the published observationally based estimate (indexed by *i*) of the LW clear-sky DREE and $\widetilde{\Omega}_{\mathrm{obs},i}$ denotes its corresponding seasonally and diurnally averaged value (see Table S5 and Fig. 1) using the correction factor $\widetilde{\Omega}_{\mathrm{mdl},i}/\Omega_{\mathrm{mdl},i}$. Here, $\widetilde{\Omega}_{\mathrm{mdl},i}$ is the diurnally averaged model result (plotted in Fig. 1) for the season (and location) that is the closest match to the time-of-year for which measurement *i* was made, whereas $\Omega_{\mathrm{mdl},i}$ is the model-calculated LW clear-sky DREE at the particular time-of-day and time-of-year for which the measurement was made. Its value was obtained by interpolating between the 6-hourly LW clear-sky DREE values calculated in our procedure using the 6-hourly reanalysis fields (see Methods). The correction factor $\widetilde{\Omega}_{\mathrm{mdl},i}/\Omega_{\mathrm{mdl},i}$ is substantially less than unity (of order ~0.80) for measurements made during daylight hours only[89-91]. This is because the LW DREE is largest in the middle of the day when both the surface temperature peaks and dust usually resides at higher altitude[90]. As such, correcting these observations to be representative of the diurnally averaged

LW DREE is critical before comparison against (diurnally averaged) model results. Note that observationally based estimates of the LW clear-sky DREE are subject to numerous limitations[89,92], which we discuss below.

Limitations and caveats. We expect the calculation of the LW direct radiative effect and forcing with the data-driven analytical model to be more accurate than climate model results because of the explicit propagation of errors (see Fig. S1), the inclusion of the spatiotemporally varying effects of LW scattering, the use of observationally constrained particle size distributions that include super coarse dust[3,22], and the integration of observational estimates of the LW DREE (Fig. S1), our methodology is nonetheless subject to important limitations that could still cause possibly substantial biases. These limitations can roughly be divided into three groups: (1) uncertainties and limitations induced by simplifying assumptions that were made in order for the data-driven analytical model to remain analytically solvable, (2) errors in the data sets used in the data-driven analytical model, and (3) errors in the observational estimates of the LW clear-sky DREE.

The main errors and limitations of the analytical model are as follows. First, we assumed that $\tau_{\mathrm{LW}} << 1$, allowing us to simplify the effects of dust on longwave radiation. However, when τ_{LW} becomes of order 1, multiple extinction effects start becoming important, which are not included, possibly causing a slight underestimate of the LW radiative effects. This could affect the calculated LW DRE at the dustiest locations, as the maximum seasonally averaged LW DAOD reaches ~0.5 in spring and summer (and ~0.3 in fall and winter) (Fig. S9). Moreover, the LW DAOD on an event basis could reach substantially above the seasonal average, contributing to a further underestimation of the LW DRE. Second, we similarly assumed that atmospheric absorption is small (i.e., $\bar{\epsilon}_{\mathrm{bel}}$, $\bar{\epsilon}_{\mathrm{abv}} << 1$). Here also, the maximum seasonally averaged $\bar{\epsilon}_{\mathrm{bel}}$ and $\bar{\epsilon}_{\mathrm{abv}}$ reach ~0.5 in summer, such that our assumption that $\bar{\epsilon}_{\mathrm{bel}}$ and $\bar{\epsilon}_{\mathrm{abv}} << 1$ would cause a slight underestimation of the LW DRE. Third, we simplified the LW radiative effects by using optical and radiative properties (e.g., $\bar{\epsilon}_{\mathrm{abv}}$, $\bar{\omega}_b$, $\bar{\beta}_{\downarrow,b}$, $\bar{k}_{\mathrm{ext},b}$, $\bar{\tau}_{\mathrm{LW}}$) averaged over the entire atmospheric window (8 – 14 μm). However, optical properties of both dust and atmospheric absorption can vary substantially in this spectral range[12,93]. As such, this simplified treatment of radiative effects can cause errors if parts of the spectrum have dust optical depths or atmospheric absorptivity of order 1, as then the radiative effects become sub-linear in the optical depth or absorptivity (see previous two limitations). Fourth, because our analysis is done with seasonally averaged variables, we neglect any sub-seasonal co-variability of LW DAOD with temperature and humidity profiles and ozone concentrations. Fifth, although we use observational estimates of the LW DREE to constrain the results of our data-driven analytical model, the agreement of our results with observations does not necessarily imply that all of the relevant processes have been accurately captured or that each parameter value used is realistic. Indeed, given the remaining uncertainties in dust LW optical properties, dust altitude, and dust size distribution, it is likely that some of the bootstrap iterations achieve RMSE < $\mathrm{RMSE}_{\mathrm{max}}$ due to compensating errors among parameters. This phenomenon, known as "equifinality", highlights that different parameter combinations can produce similar model outputs, a well know result in perturbed parameter ensemble model study approaches[94]. Sixth, our analysis assumes that dust produces zero top-of-atmosphere direct radiative effect outside of the atmospheric window because of high absorptivity outside of that spectral region, primarily due to absorption by water vapor. However, for high and cold dust layers, the overhead absorptivity might be small enough that dust still exerts some direct radiative effect outside of the atmospheric window, causing some overestimation of the LW DRE. Seventh, our analysis does not account for the possible enhancement of LW extinction created by coatings on supermicron dust particles[95,96]. And finally, our calculation of the LW DRF assumed that the LW DREE has stayed constant over time since the pre-industrial period. However, surface and atmospheric temperatures, and concentrations of water vapor, CO2, and other greenhouse gases have changed from the pre-industrial to the historical period. Additionally, the vertical profile and horizontal distribution of dust has likely changed[97]. All these changes modify the LW DREE, which we do not account for.

In addition to these limitations inherent in the analytical model, there are also several important limitations on the data used to drive the analytical model. The DustCOMM dust climatology that is an important input to the analytical model has many experimental, observational, and modeling uncertainties propagated, but might still be subject to important biases, as discussed in Kok et al.[3,4]. One especially important such bias for the LW DRE is that the vertical profile of dust in DustCOMM is based on an ensemble of model simulations, but these are known to struggle to reproduce the vertical profile of dust[8,98]. A second important limitation on the data driving the analytical model is the large uncertainty in the size-dependent LW optical properties of dust. Although we used a series of LW refractive index data sets[12,13,15,16], and thus propagated the uncertainty quantified by the spread in these data sets, this ensemble of refractive indices might still be biased because of various factors, including the limited number of dust samples analyzed, the inherent difficulties of reproducing natural dust emission in a laboratory[99], experimental limitations and biases in measuring LW optical properties[12], and the need to represent all dust with a single set of LW optical properties, whereas in reality there exists (poorly quantified) regional variability due to changes in mineralogy[12,46]. A third important limitation on the data driving the analytical model is that the ratio of the all-sky to clear-sky LW DRE that we used from an ensemble of model simulations (Fig. S4) might be biased because these simulations do not account for LW scattering, which responds differently to clouds below the dust layer than does LW absorption. A fourth limitation is that the analytical model uses only a single reanalysis data set (MERRA-2) to provide the atmospheric properties and surface temperature, and thus does not account for uncertainty in these variables.

Note that the effects of all the above limitations on the calculated LW direct radiative effect and forcing are mitigated by our procedure of retaining only the subset of bootstrap iterations that are consistent with observational LW DREE estimates (explained above and shown in Fig. S1 and Extended Data Fig. 2). However, those observational estimates have important limitations themselves. First, studies that used ground-based or in situ measurements to estimate the LW DREE necessarily mostly focused on (intense) dust events, which might have different properties (e.g., dust vertical profile and size distribution) and atmospheric conditions (e.g., drier) than the seasonally averaged properties used to drive the analytical model. Second, estimates of the LW DREE over land that used observed temperatures[91,100] inherently include the fast response of the surface temperature to the dust loading. Since dust on balance decreases surface temperatures by decreasing incident solar radiation, this effect reduces the upwelling LW flux, which is then erroneously interpreted as an instantaneous LW dust radiative effect. This effect can cause an overestimate of the instantaneous LW DREE that is at most 25-35%[92]. Third, satellite-based studies usually assume that the LW DRE is zero when clouds are present in the atmospheric column[89]. This is reasonable when dust is located below clouds, but dust still exerts a LW cooling effect when located above clouds, which is neglected. Fourth, errors in cloud screening can cause LW effects of clouds to be attributed to dust or vice versa[89]. Similarly, errors in aerosol typing can affect the calculation of the dust aerosol optical depth. And fifth, most of the LW DREE observations were obtained for North African dust (Fig. 1) in Spring and Summer, such that systematic differences in dust LW optical properties with season and location that are not captured by the analytical model could induce a bias.

Supplementary Tables

Table S1. Compilation of global model simulations of the global annual mean LW DRE at TOA.

Study	Model	Annual global LW clear-sky DRE (Wm^{-2})	Annual global LW all-sky DRE (Wm^{-2})	All-sky LW DRE due to scattering (Wm^{-2})
This study	CESM/CAM4	0.26[a]	0.20[a]	0.07
This study	IMPACT	0.19	0.13	0
This study	GISS ModelE2.1	0.13[b]	0.10[b]	0.02
This study	GEOS/GOCART	0.12	0.10	0
This study	MONARCH	0.17	0.13	0
This study	INCA	0.15	0.12	0
Heald et al. (2014)[101]	GEOS-Chem–RRTMG	0.16	0.14	0
Albani et al. (2014)[44]	CESM/CAM4	--	0.125[c]	0
Albani et al. (2014)[44]	CESM/CAM5	--	0.14	0
Scanza et al. (2015)[102]	CESM/CAM4	--	0.09	0
Scanza et al. (2015)[102]	CESM/CAM5	--	0.13	0
Klingmuller et al. (2019)[103]	ECHAM/MESSy	--	0.09	0
Tucella et al. (2020)[104]	GEOS-Chem	--	0.09	0
Di Biagio et al. (2020)[81]	LMDZOR-INCA	--	0.22[d]	0.11
Checa-Garcia et al. (2021)[82]	LMDZOR-INCA	0.14	--	--
Ito et al. (2021)[46]	IMPACT	--	0.23[d]	0.12
Li et al. (2021)[105]	CESM/CAM5	--	0.11[a]	0.04
Li et al. (2021)[105]	CESM/CAM6	--	0.14[a]	0.05
Li et al. (2021)[105]	MONARCH	--	0.17	0
Feng et al. (2022)[106]	E3SMv1	--	0.12[e]	0
Ke et al. (2022)[107]	CESM/CAM5/MAM9	--	0.13	0
Wang et al. (2024)[108]	SPRINTARS	--	0.16[f]	0
--	--	0.16	0.13 (0.09 – 0.22)[g]	0.02

[a]The effect of longwave scattering was approximated by increasing the LW DRE at the top-of-atmosphere by 50%.
[b]The effect of longwave scattering was approximated by increasing the LW extinction due to dust by 30%.
[c]Mean of the C4wn and C4fn model simulations.
[d]The effect of longwave scattering was approximated by scaling the LW DRE at the top-of-atmosphere by a factor of 2.04.
[e]Mean of five model simulations with different resolution, dust size distribution, and model parameter settings.
[f]Mean of three model simulations with different optical properties and dust size distribution.
[g]The range represents the 90% confidence interval, which was obtained by eliminating the lowest and highest values, leaving the 19 central values of the 21 model results, which corresponds approximately to the central 90% of model results.

Table S2. Size-resolved dust radiative effects. Listed are the aerosol optical depth in both the LW (averaged over the 8-14 μm spectral range) and the SW (550 nm) spectra, the TOA DRE for both all-sky and clear sky conditions, and the LW direct radiative effect efficiency (DREE). All values represent global annual means and were obtained from the analytical model.

Diameter range	LW DAOD ($\times 10^{-3}$)	SW DAOD	LW clear-sky DRE (Wm^{-2})	LW all-sky DRE (Wm^{-2})	LW DREE ($Wm^{-2}\,\tau_{SW}^{-1}$)
$D \leq 2.5$ μm	1.1	0.013	0.04	0.03	1.4

2.5 < D ≤ 5 µm	2.7	0.007	0.10	0.07	14
5 < D ≤ 10 µm	4.3	0.004	0.12	0.10	30
10 < D ≤ 20 µm	2.5	0.002	0.05	0.04	20
D > 20 µm	0.4	0.0004	0.01	0.01	10
All dust	11.0 ± 3.1	0.027 ± 0.005	0.32 ± 0.08	0.25 ± 0.06	11 ± 5

Table S3. Statistical parameters quantifying agreement of six global models with LW DREE observations

Global model	Annual global LW all-sky DRE (Wm^{-2})	R^2	RMSE ($Wm^{-2}\ \tau_{SW}^{-1}$)	Bias ($Wm^{-2}\tau_{SW}^{-1}$)
CESM/CAM4	0.20	0.21	5.2	-4.4
IMPACT	0.13	0.35	9.0	-8.7
GISS ModelE2.1	0.10	0.48	6.5	-6.1
GEOS/GOCART	0.10	0.00	8.4	-7.7
MONARCH	0.13	0.25	7.2	-6.8
LMDZOR-INCA	0.12	0.07	9.7	-9.3

Table S4. Optical properties in the atmospheric window (i.e., averaged over the 8-14 µm spectral range) for each dust particle bin of each of the six different model simulations used in the DustCOMM dust climatology (see Ref. [3]). Reported values represent the average and standard deviation. The variability in the optical properties for a given particle bin is due to variability in the sub-bin dust size distribution, which is based on Adebiyi and Kok[1] [see Eqs. (S7)-(S9)], and in the dust complex refractive index in the atmospheric window, which is based on a random drawing of one of six data sets (see Table S6).

Model	Bin number	Diameter range (µm)	SSA ($\bar{\omega}_b$)	Downscatter fraction ($\bar{\beta}_{\downarrow,b}$)	Mass ext. efficiency ($\bar{k}_{\mathrm{ext},b}$ in m^2g^{-1})
CESM/CAM4	1	0.1-1	0.014 ± 0.006	0.495 ± 0.001	0.084 ± 0.036
	2	1-2.5	0.139 ± 0.055	0.472 ± 0.004	0.106 ± 0.040
	3	2.5-5	0.39 ± 0.13	0.374 ± 0.016	0.181 ± 0.078
	4	5-10	0.52 ± 0.15	0.231 ± 0.005	0.203 ± 0.057
	5	10-20[a]	0.52 ± 0.10	0.150 ± 0.009	0.118 ± 0.022
IMPACT	1	0.1-1.26	0.026 ± 0.011	0.493 ± 0.001	0.086 ± 0.036
	2	1.26-2.5	0.150 ± 0.059	0.470 ± 0.004	0.109 ± 0.041
	3	2.5-5	0.39 ± 0.13	0.374 ± 0.016	0.181 ± 0.078
	4	5-20	0.52 ± 0.12	0.200 ± 0.009	0.159 ± 0.036
GISS ModelE2.1	1	0.2–0.36	$(0.9 \pm 0.4)\times10^{-3}$	0.499 ± 0.001	0.081 ± 0.036
	2	0.36-0.6	$(3.9 \pm 1.6)\times10^{-3}$	0.498 ± 0.002	0.082 ± 0.036
	3	0.6-1.2	0.025 ± 0.010	0.493 ± 0.008	0.086 ± 0.036
	4	1.2-2	0.103 ± 0.041	0.479 ± 0.003	0.100 ± 0.039
	5	2-4	0.32 ± 0.12	0.417 ± 0.013	0.156 ± 0.065
	6	4-8	0.50 ± 0.14	0.267 ± 0.009	0.212 ± 0.072
	7	8-16	0.53 ± 0.12	0.169 ± 0.007	0.146 ± 0.030
	8	16-20	0.49 ± 0.05	0.128 ± 0.012	0.084 ± 0.011
GEOS/GOCART & LMDZOR-INCA[b]	1	0.2–2	0.08 ± 0.03	0.483 ± 0.002	0.095 ± 0.038
	2	2-3.6	0.230 ± 0.11	0.430 ± 0.010	0.148 ± 0.061
	3	3.6-6	0.46 ± 0.15	0.310 ± 0.014	0.210 ± 0.085
	4	6-12	0.54 ± 0.14	0.204 ± 0.004	0.185 ± 0.044

	5	12-20	0.51 ± 0.08	0.140 ± 0.009	0.103 ± 0.017
MONARCH	1	0.2–0.36	$(0.9 \pm 0.4)\times10^{-3}$	0.499 ± 0.001	0.081 ± 0.036
	2	0.36-0.6	$(3.9 \pm 1.6)\times10^{-3}$	0.498 ± 0.002	0.082 ± 0.036
	3	0.6-1.2	0.025 ± 0.010	0.493 ± 0.008	0.086 ± 0.036
	4	1.2-2	0.103 ± 0.041	0.479 ± 0.003	0.100 ± 0.039
	5	2-3.6	0.30 ± 0.11	0.430 ± 0.010	0.148 ± 0.061
	6	3.6-6	0.46 ± 0.15	0.310 ± 0.014	0.210 ± 0.085
	7	6-12	0.54 ± 0.14	0.204 ± 0.004	0.185 ± 0.044
	8	12-20	0.51 ± 0.08	0.140 ± 0.009	0.103 ± 0.017
All models	SC1[c]	20-35	0.50	0.075	0.084
	SC2[c]	35-62.5	0.50	0.075	0.044
	SC3[c]	62.5-100	0.50	0.075	0.024

[a]Denotes an additional bin added to the original model output in order to extend the particle diameter range to 20 μm. See Kok et al. [3] for details.

[b]Both models use the same particle bins. See Kok et al. [3] for details.

[c]Results for each model were extended with three bins to include dust with diameters between 20 to 100 μm, using simulations with the Community Earth System Model (CESM) from Meng et al. [10], as described in Methods.

Table S5. Compilation of observational estimates of the LW clear-sky direct radiative effect efficiency (DREE) at the top-of-atmosphere. Listed are the originally reported ($\Omega_{\mathrm{obs},i}$), the diurnally corrected, and the diurnally and seasonally corrected ($\tilde{\Omega}_{\mathrm{obs},i}$) values of the LW DREE (see Eq. S10), in units of Wm^{-2} per unit of SW (550 nm) optical depth. Also listed is whether the study was primarily based on in situ data or on satellite data and whether the observational estimate was representative of the LW DREE over land or over ocean.

Reference	Study area & coordinates	Season or months	Study type	Time (UTC)	Reported LW DREE	Diurnal LW DREE	Diurnal & seasonal LW DREE
Highwood et al. (2003)[109]	Between Sal Island and Daqar (16 °N, ~20 °W)	September	In situ; over ocean	Diurnal	9.7	9.7	9.6
Brindley and Russell (2009)[89]	West Africa (16 - 28 °N, 16 - 4 °W)	MAM	Satellite; over land	0800-1600	18	14.2	14.2
Brindley and Russell (2009)[89]	West Africa (16 - 28 °N, 16 - 4 °W)	JJA	Satellite; over land	0800-1600	17	14.2	14.2
Brindley and Russell (2009)[89]	Niger/Chad (15 - 20 °N, 5 - 20 °E)	MAM	Satellite; over land	0800-1600	15	11.6	11.6
Brindley and Russell (2009)[89]	Niger/Chad (15 - 20 °N, 5 - 20 °E)	JJA	Satellite; over land	0800-1600	16	13.1	13.1
Brindley and Russell (2009)[89]	Sudan (15 - 22 °N, 22 - 36 °E)	MAM	Satellite; over land	0800-1600	19	14.9	14.9
Brindley and Russell (2009)[89]	Sudan (15 - 22 °N, 22 - 36 °E)	JJA	Satellite; over land	0800-1600	21	17.4	17.4
Brindley and Russell (2009)[89]	Egypt/Israel (23 - 32 °N, 25 - 35 °E)	MAM	Satellite; over land	0800-1600	19	16.0	16.0
Brindley and Russell (2009)[89]	Egypt/Israel (23 - 32 °N, 25 - 35 °E)	JJA	Satellite; over land	0800-1600	25	21.1	21.1
Brindley and Russell (2009)[89]	North Libya (27 - 33 °N, 15 - 25 °E)	MAM	Satellite; over land	0800-1600	18	14.8	14.8
Brindley and Russell (2009)[89]	North Libya (27 - 33 °N, 15 - 25 °E)	JJA	Satellite; over land	0800-1600	20	16.6	16.6
Brindley and Russell (2009)[89]	South Libya (23 - 27 °N, 15 - 25 °E)	MAM	Satellite; over land	0800-1600	16	12.5	12.5
Brindley and Russell (2009)[89]	South Libya (23 - 27 °N, 15 - 25 °E)	JJA	Satellite; over land	0800-1600	18	14.5	14.5
Yang et al. (2009)[90]	Sahara (15 - 30 °N, 10 °W - 30 °E)	JJAS	Satellite; over land	1030 and 1330	18.5	14.4	15.0

Xia and Zong (2009)[91]	Taklimakan desert (36 - 42 °N, 75 - 95 °E)	May	Satellite; over land	0500	28.4	21.0	19.1
Hansell et al. (2010)[110]	Cape Verde (16.73 °N, 22.93 °W)	September	In situ; over land	Diurnal (ocean)	13	13	12.8
Osborne et al. (2011)[100]	Mauritania and Niger (18 °N, 6.45 °W)	June	In situ; over land	Diurnal	17.2	17.2	18.5
Hansell et al. (2012)[111]	East of Taklimakan desert (39 °N, 101 °E)	April and May	In situ; over land	Diurnal	19	19	18.4
Di Sarra et al. (2011)[112] & Meloni et al. (2015)[113]	Lampedusa (35.5 °N, 12.6 °W)	March and May	In situ; over ocean	Diurnal	10.3	10.3	10.3
Meloni et al. (2018)[114]	Lampedusa (35.5 °N, 12.6 °W)	June	In situ; over ocean	Diurnal	15.8	15.8	16.3
Song et al. (2018)[115]	Tropical North Atlantic (10 - 30 °N, 45 - 20 °W)	JJA	Satellite; over ocean	Diurnal	10.5	10.5	10.5

Table S6. Values of the six atmospheric window-averaged (8-14 μm) complex refractive indices used in this study.

Reference	**Complex refractive index**
Volz (1972)[13]	$1.54 + 0.11i$
Volz (1973)[14]	$1.83 + 0.33i$
Fouquart et al. (1987)[15]	$1.00 + 0.28i$
Hess et al. (1998)[16]	$1.85 + 0.35i$
Di Biagio et al. (2014)[17]	$1.59 + 0.17i$
Di Biagio et al. (2017)[12]	$1.45 + 0.12i$

Supplementary Figures

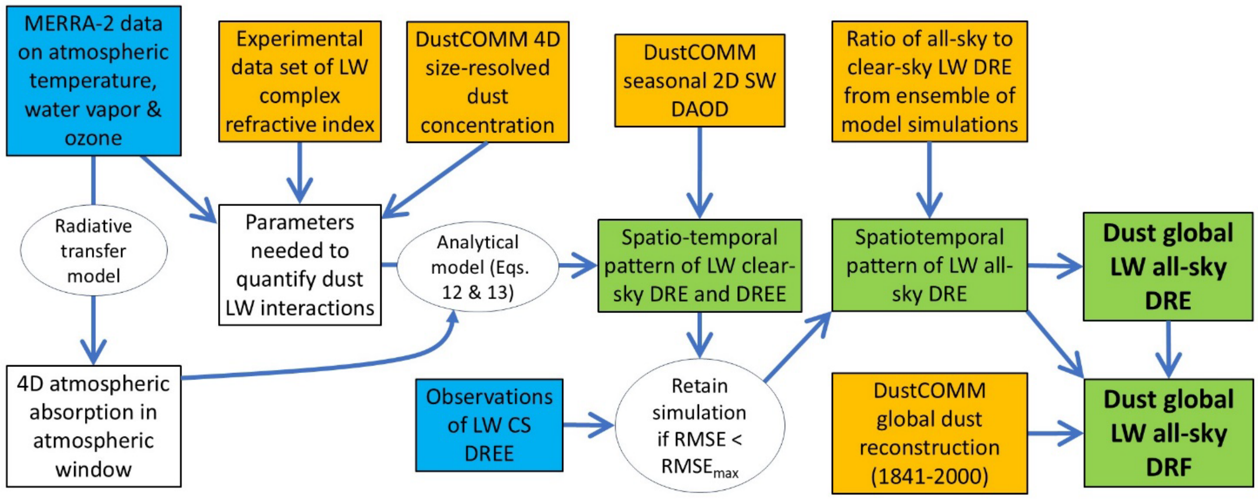

Figure S1. Schematic overview of the methodology used to constrain the longwave (LW) all-sky direct radiative effect (DRE) and direct radiative forcing (DRF) at top-of-atmosphere. Orange boxes denote data from which different random realizations are drawn for each bootstrap iteration, blue boxes denote inputs of observationally informed data that are the same for each bootstrap iteration, and green boxes denote results that are reported in figures in the main text.

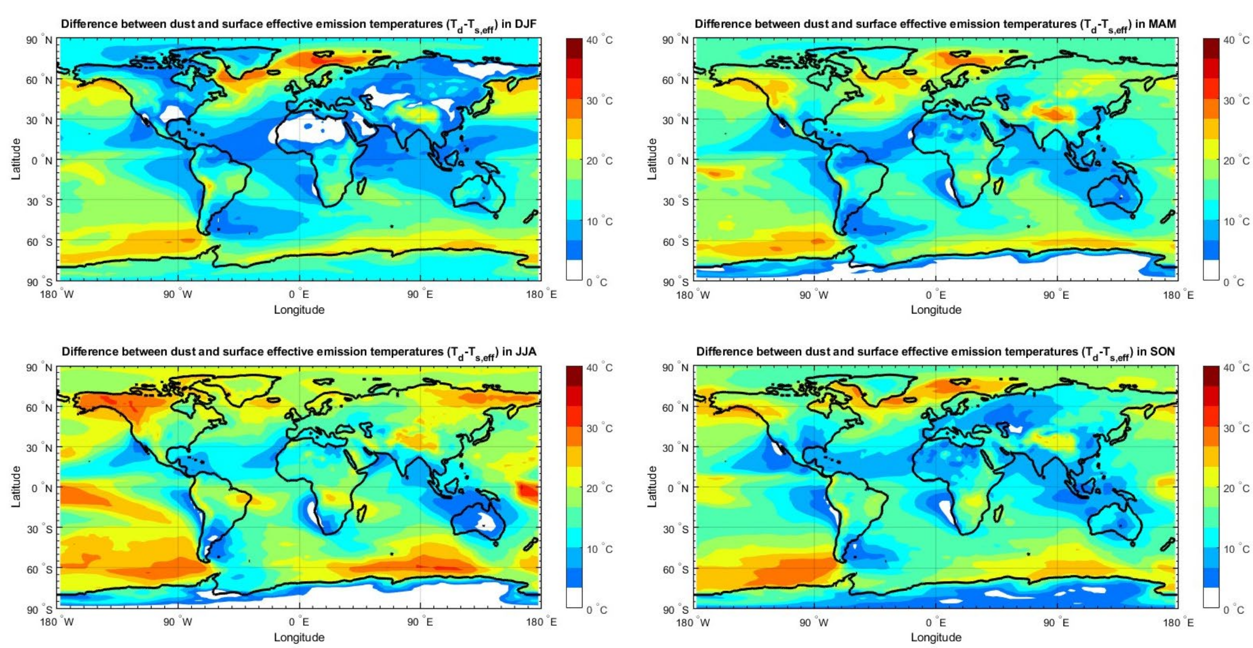

Figure S2. Difference between the dust layer temperature (T_d) and the effective surface emission temperature (T_{bel}) as a function of season.

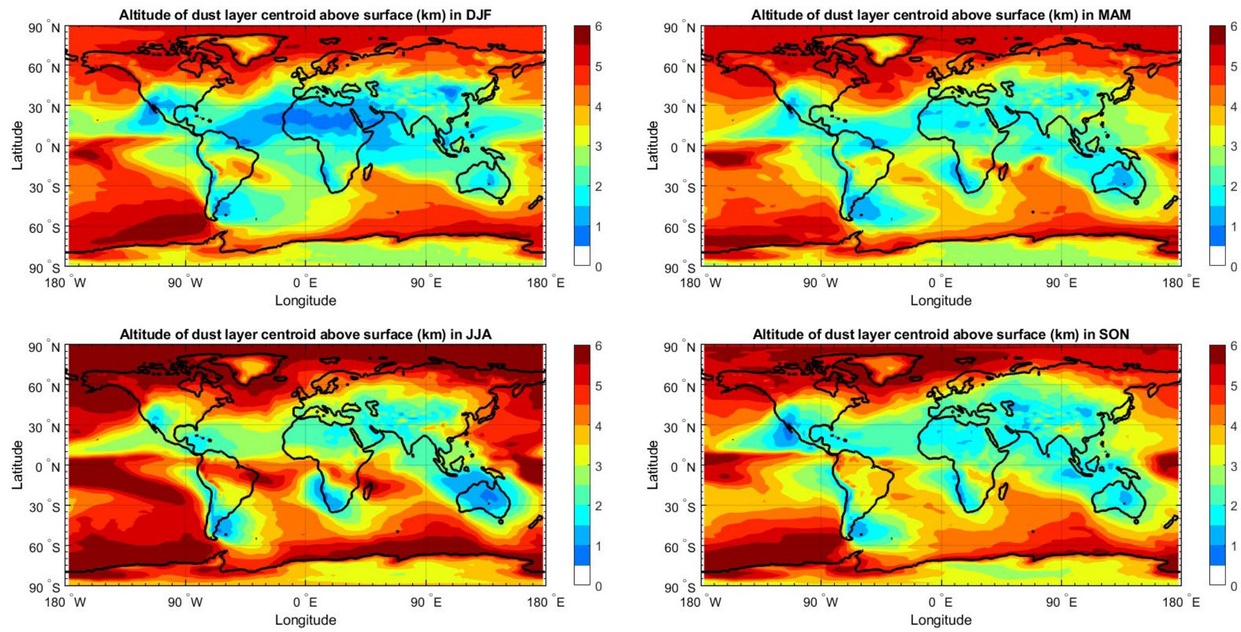

Figure S3. Elevation of dust layer centroid above the local surface. The dust layer centroid is calculated as $z_{\mathrm{d}} = \int_0^\infty \bar{\beta}_{\mathrm{LW}}(z) z dz \,/\, \int_0^\infty \bar{\beta}_{\mathrm{LW}}(z) dz$, where the volume extinction coefficient in the LW spectrum is calculated as $\bar{\beta}_{\mathrm{LW}}(z) = \sum_b^{n_b} \rho_b(z) \bar{k}_{\mathrm{ext},b}$, where the index b sums over the n_{b} particle size bins, ρ_b is the density (kgm^{-3}) of dust in bin b in the layer, and $\bar{k}_{\mathrm{ext},b}$ is the mass extinction efficiency of bin b (Table S4).

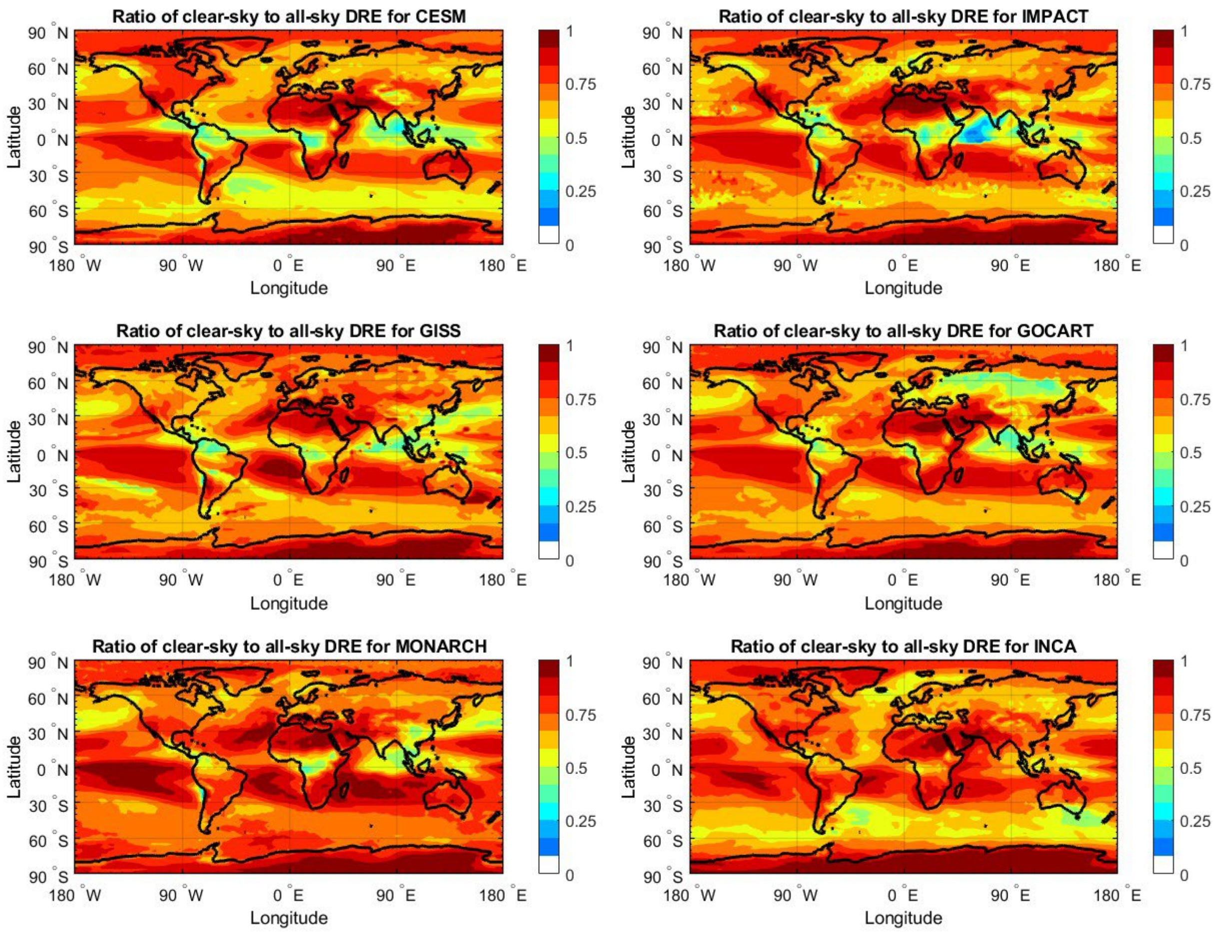

Figure S4. Maps of the ratio of the clear-sky to the all-sky LW DRE at the top-of-atmosphere for the six model simulations in our ensemble.

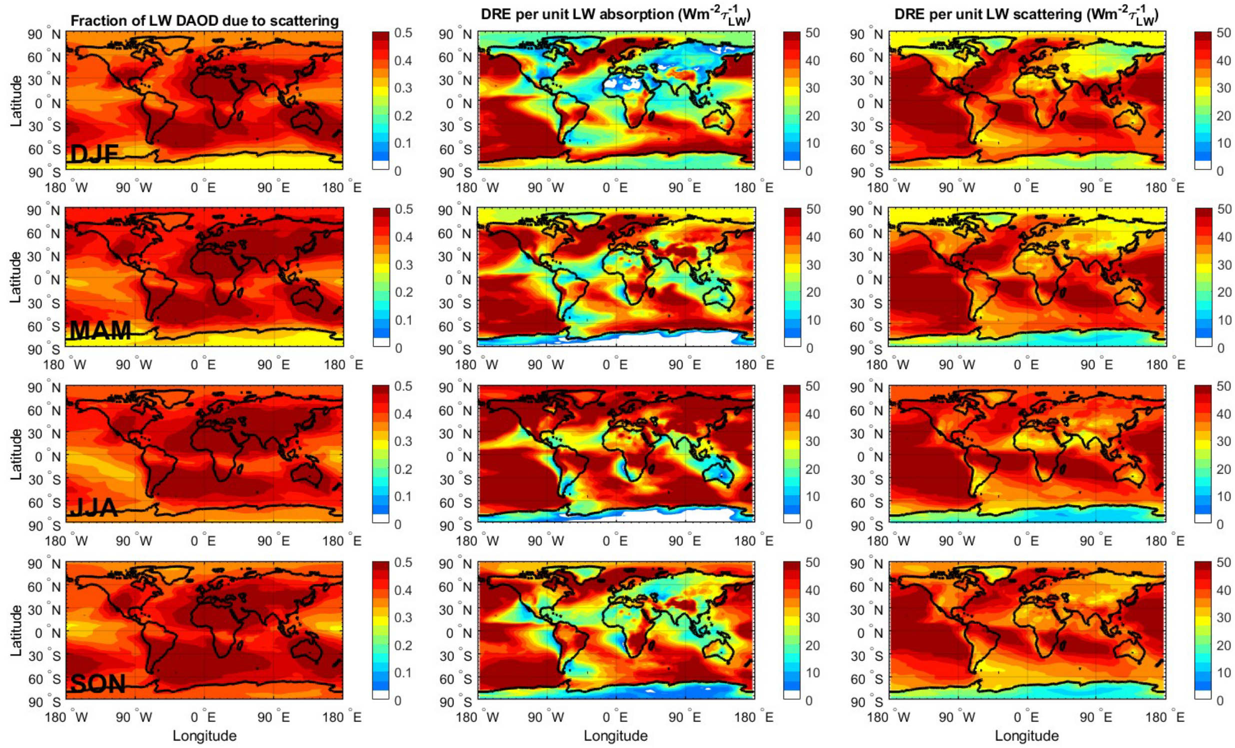

Figure S5. Separation of seasonal TOA LW radiative effects into contributions from absorption and scattering. The fractional contribution of scattering to the dust aerosol optical depth (τ_{LW}) in the atmospheric window (averaged across 8-14 μm) is somewhat below 0.5 in dust source regions, decreasing to approximately 0.4 in remote regions (left columns). However, because 28 ± 3 % of scattering interactions result in downscattering (Fig. S6), scattering is relatively effective in perturbing Earth's radiative energy budget, with a unit of LW dust aerosol optical depth (DAOD) from scattering (right column) generating a greater TOA radiative effect than a unit of LW DAOD from absorption (middle column). In the global annual mean, a unit of LW DAOD due to scattering generates 33 ± 7 Wm^{-2} of TOA radiative effect, whereas a unit of LW DAOD from absorption generates 26 ± 7 Wm^{-2}, which is less than 80% of the radiative effect produced by scattering.

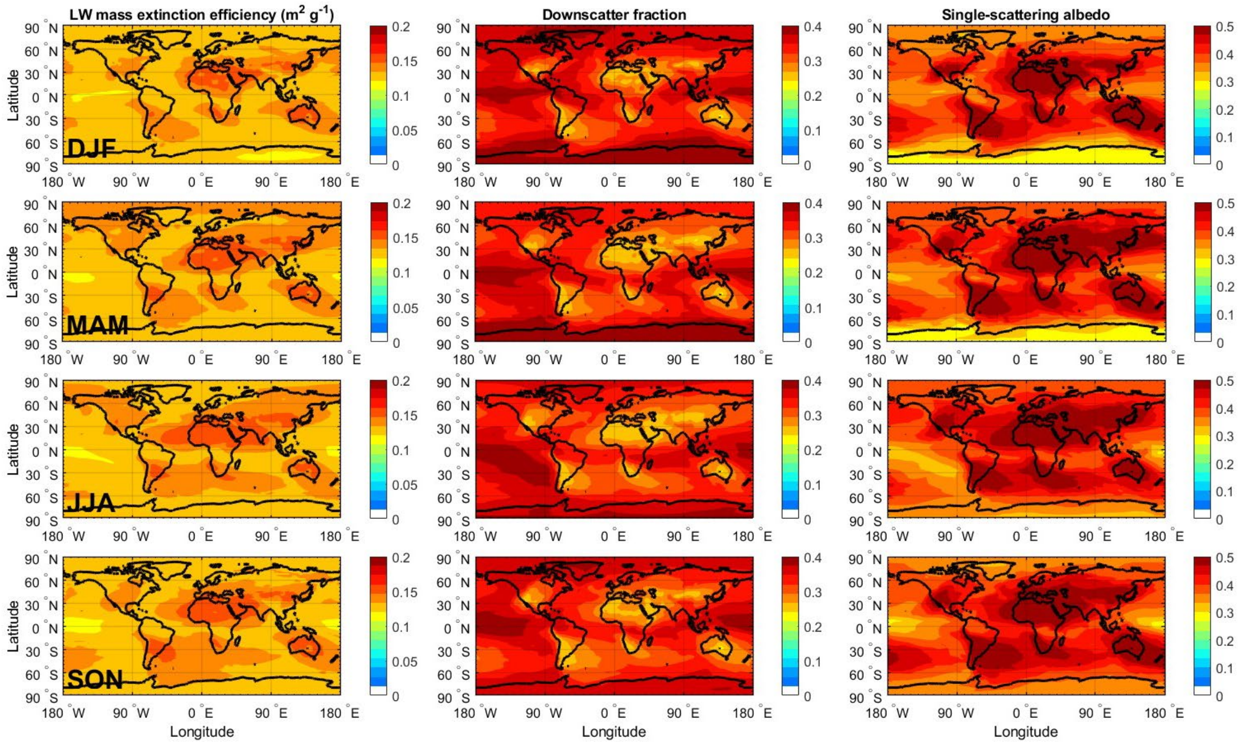

Figure S6. Spatial variability of dust optical properties in the LW spectrum. Shown are the seasonally averaged mass extinction efficiency $\bar{k}_{\mathrm{ext}}$ (left column), downscatter fraction ($\bar{\beta}_{\downarrow}$; middle column), and single-scattering albedo ($\bar{\varpi}$; right column), averaged over the atmospheric window (8-14 μm).

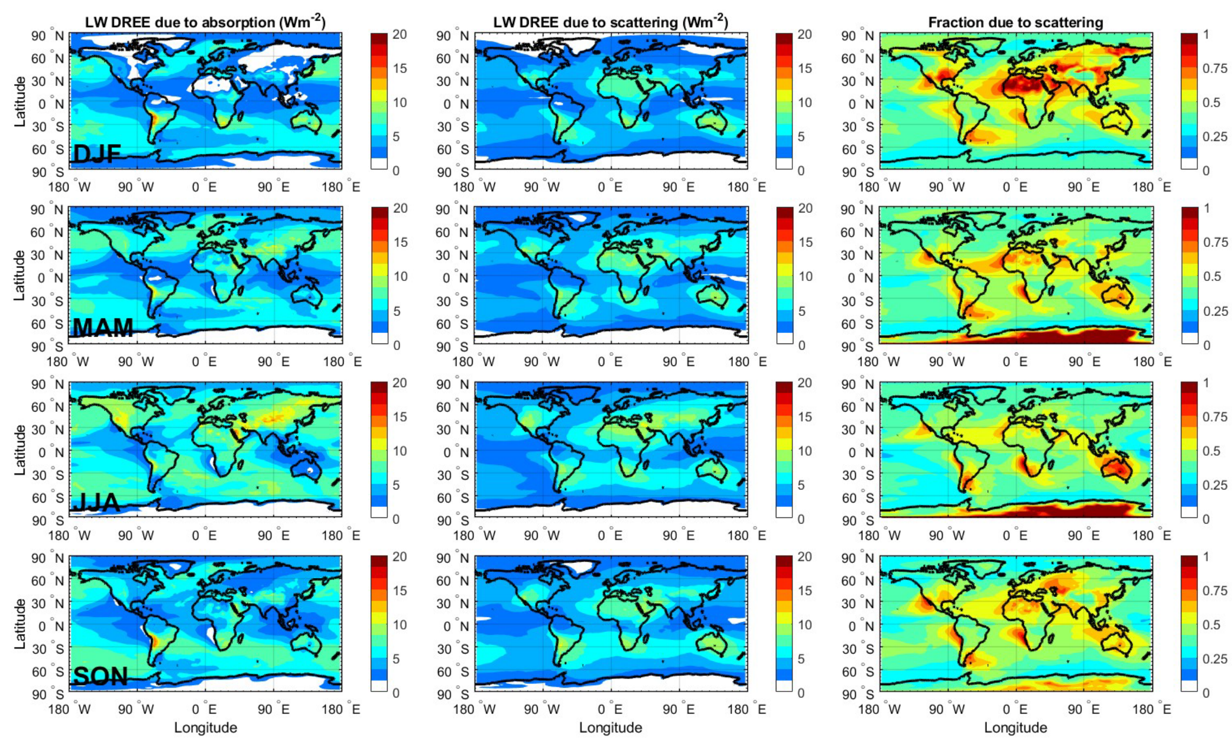

Figure S7. The LW DREE at the top-of-atmosphere that is due to absorption (left column), due to scattering (middle column), and the fraction of the LW DREE warming that is due to scattering (right column), all as a function of season. The spatial pattern in the LW absorption DREE is primarily due to the spatiotemporal pattern of the difference in the emission temperatures of dust and the surface (Fig. S2), which in turn depends largely on the dust altitude (Fig. S3). In contrast, the spatial pattern in the LW scattering DREE does not depend on the temperature of the dust layer and instead is primarily determined by the spatial patterns of the single-scattering albedo, the downscatter fraction (Fig. S6), and overhead atmospheric absorption (Fig. S11g). The correlation between the spatially resolved LW DREE due to absorption and scattering is modest, with Pearson correlation coefficients of 0.61, 0.70, 0.78, and 0.64 for DJF, MAM, JJA, and SON, respectively (0.69 for the annual mean results). Note that the fractional contribution due to scattering is very large in polar winter because the presence of persistent temperature inversions reduces the warming effect of dust absorption of LW radiation, even to the point that it produces net cooling. All results are for clear-sky conditions.

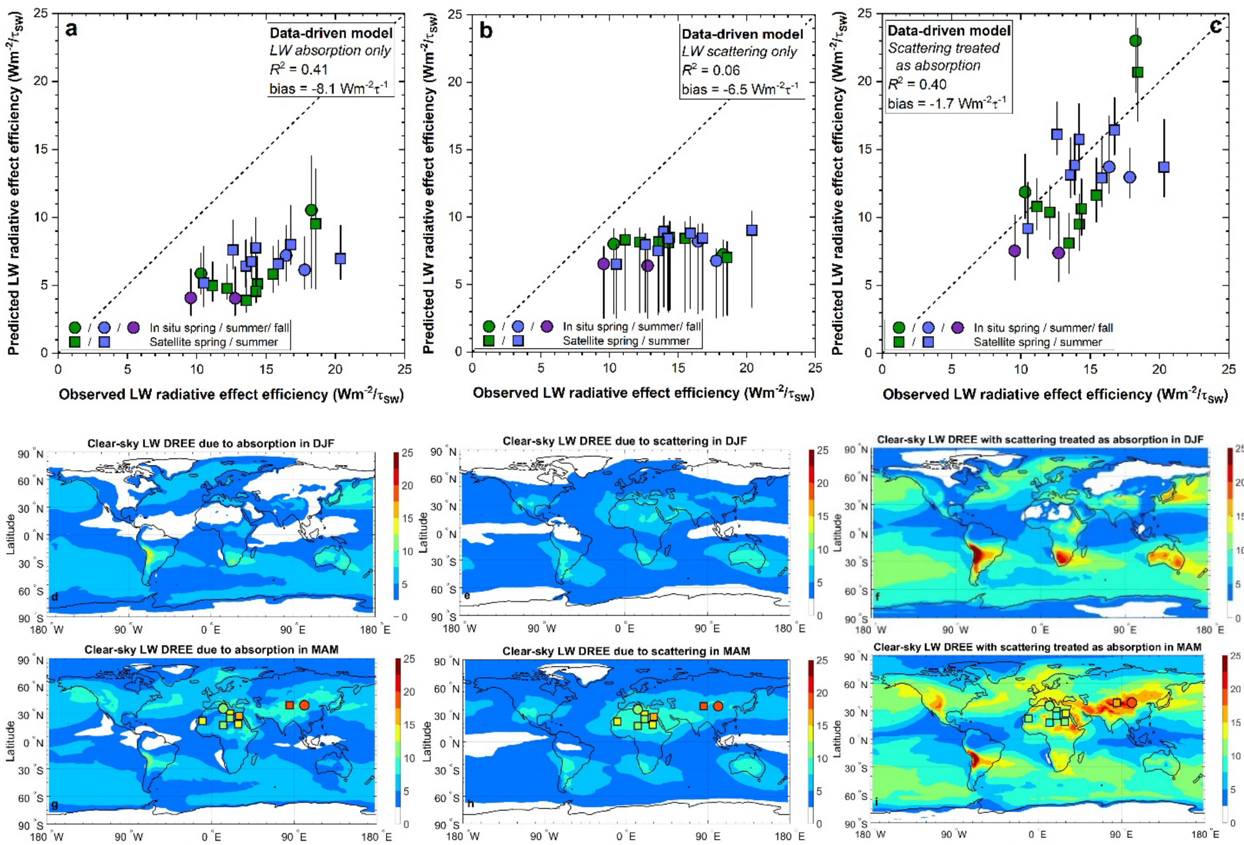

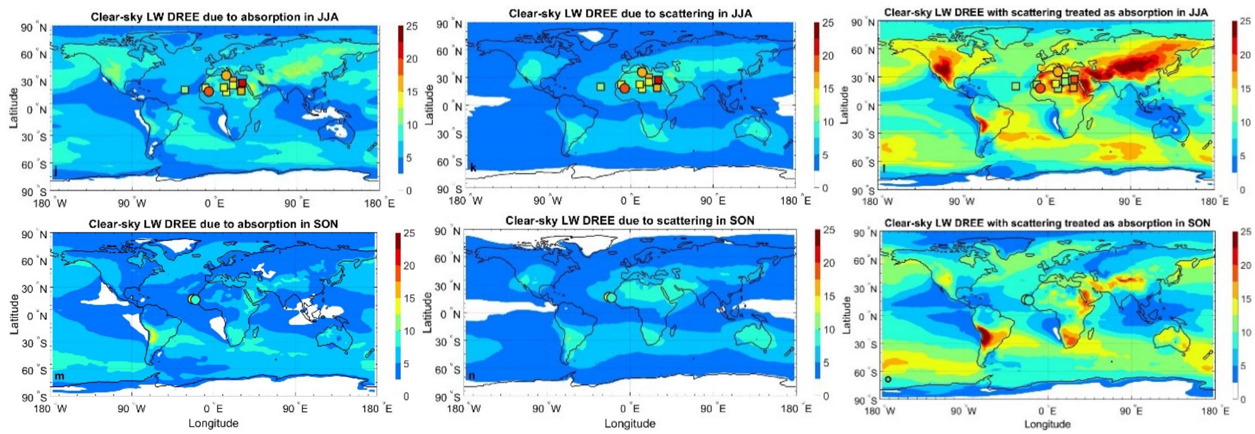

Figure S8. Analytical model predictions of clear-sky longwave (LW) direct radiative effect efficiency (DREE) due only to absorption interactions (left column), due only to scattering interactions (middle column), and with scattering treated as absorption by setting the single-scattering albedo equal to zero (right column). Shown for each of these three cases are the comparison against observational estimates of LW clear-sky DREE derived mainly from in situ (colored circles) and satellite (colored squares) data (panels **a**-**c**). Also shown are the spatial patterns of the LW clear-sky DREE for each of the three cases, along with the observational constraints, for boreal winter (DJF; panels **d**-**f**), boreal spring (MAM; panels **g**-**i**), boreal summer (JJA; panels **j**-**l**), and boreal fall (SON; panels **m**-**o**).

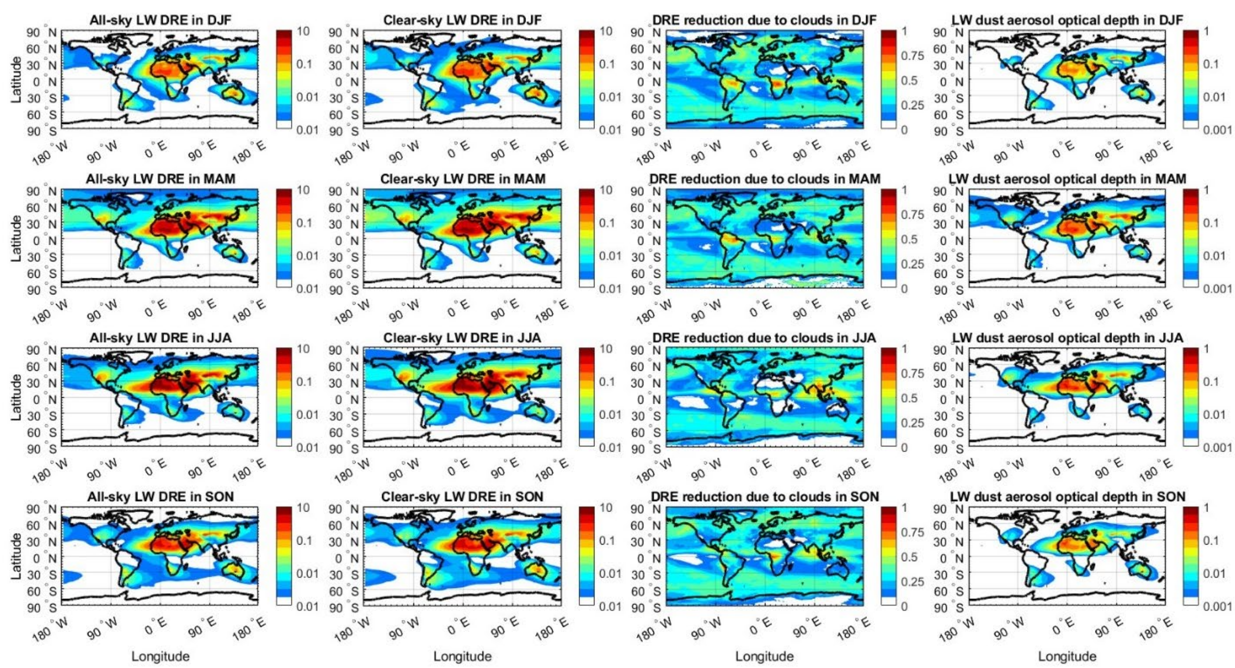

Figure S9. Seasonally averaged dust radiative effects in the LW spectrum. Shown for all four seasons (different rows) are the all-sky (first column) and clear-sky (second column) LW DRE at the top-of-atmosphere, the fractional reduction of the LW DRE due to cloud cover (third column), and the LW dust aerosol optical depth (fourth column).

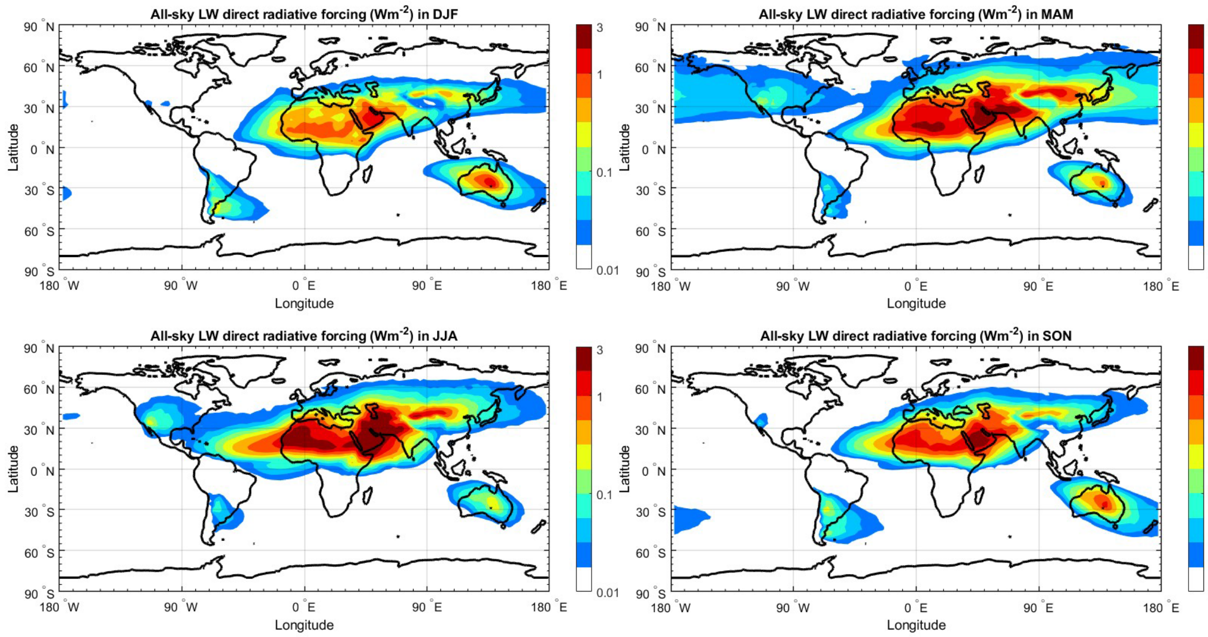

Figure S10. The seasonally averaged LW direct radiative forcing.

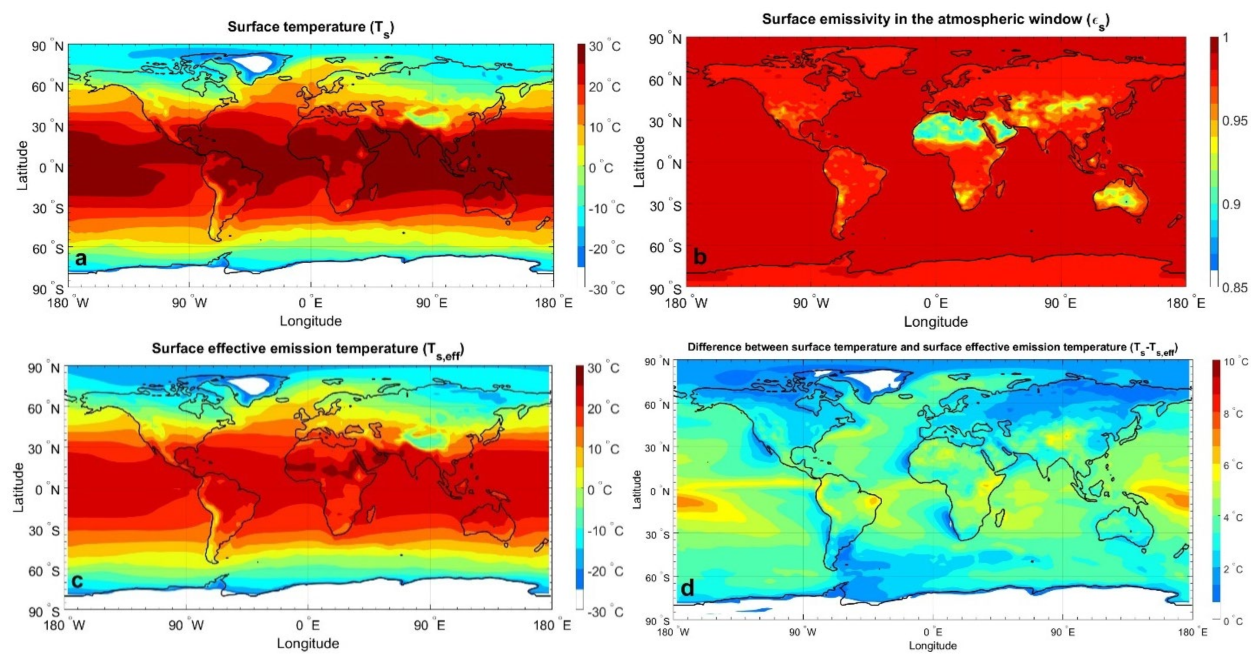

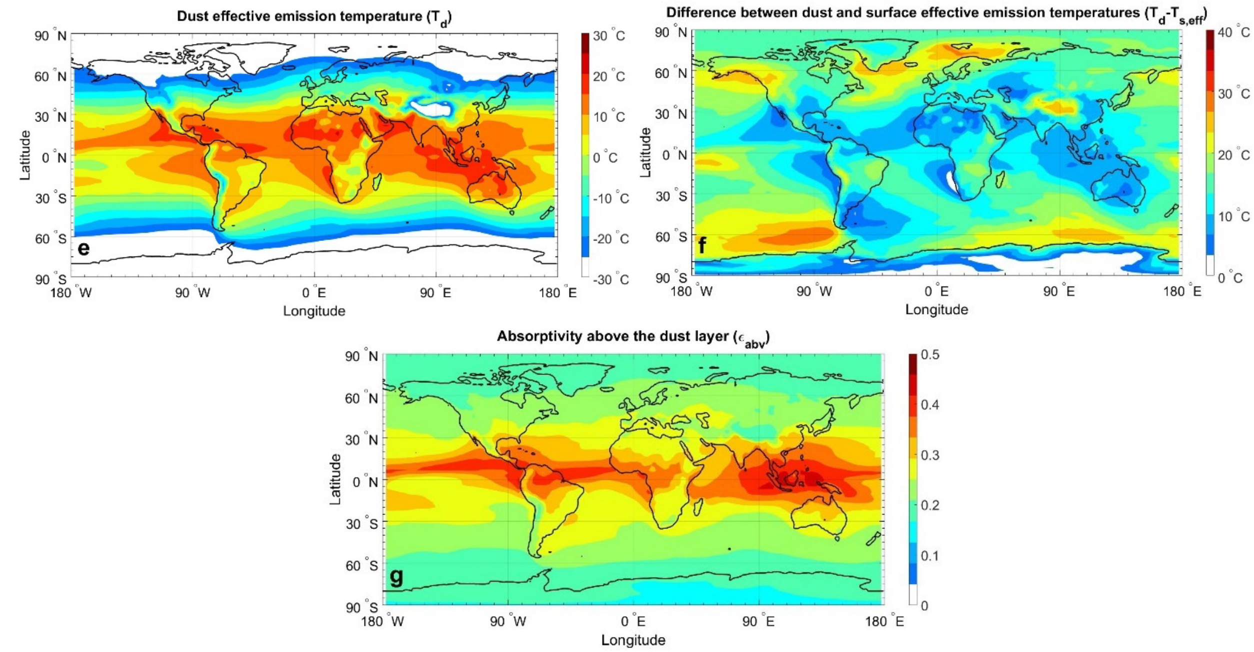

Figure S11. Dust radiative effects in the LW spectrum are controlled by temperature, surface emissivity, and atmospheric absorptivity. Shown are the annual mean surface temperature, T_s (**a**), the surface emissivity in the atmospheric window (8-14 μm), $\bar{\epsilon}_s$ (**b**), the effective emission temperature below the dust layer, $T_{s,eff}$ (**c**), the difference between the surface temperature and the surface effective emission temperature, T_s-$T_{s,eff}$ (**d**), the dust effective emission temperature, T_d (**e**), the difference between the dust and the surface effective emission temperature, T_d-$T_{s,eff}$ (**f**), and the absorptivity in the atmospheric window above the dust layer, $\bar{\epsilon}_{abv}$ (**g**). All graphs represent annual mean values for the 2004-2008 period (see Methods).

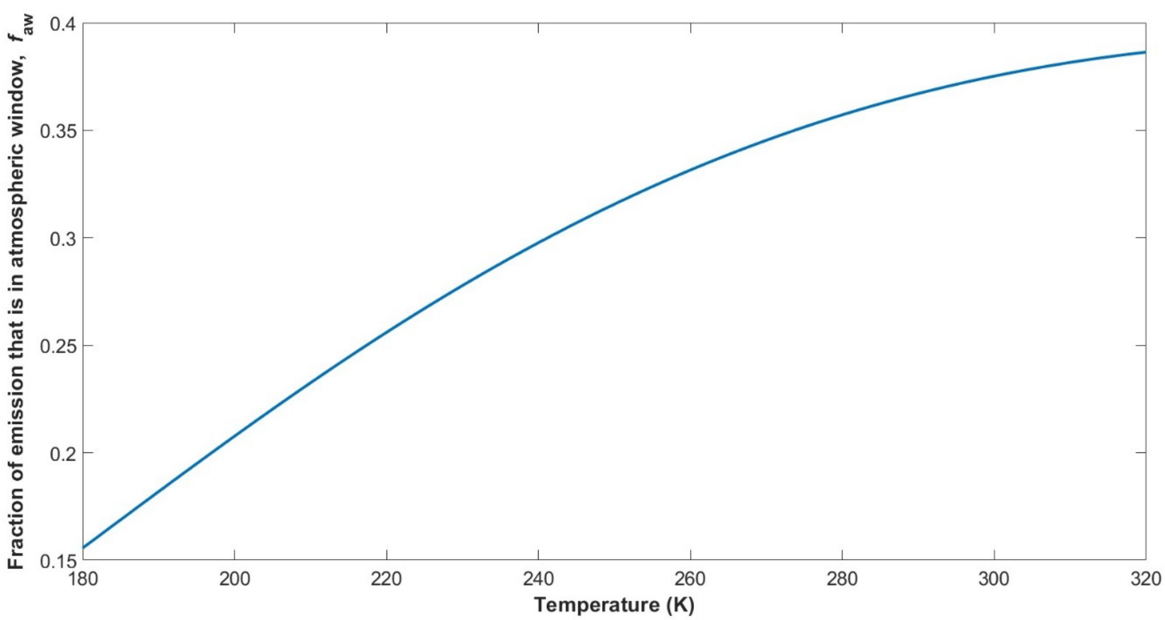

Figure S12. Fraction of emitted radiant energy that is in the atmospheric window between 8 and 14 μm, as a function of temperature.

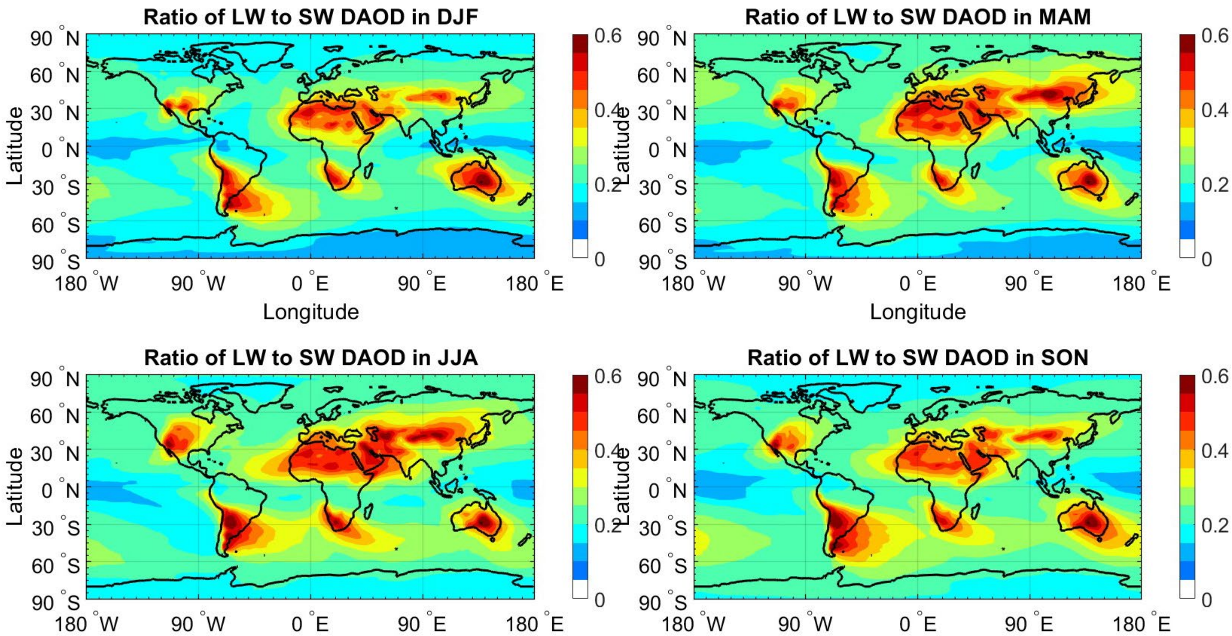

Figure S13. Ratio of the longwave (LW) dust aerosol optical depth (DAOD; averaged across the 8-14 μm atmospheric window) and the shortwave (SW) DAOD (at 550 nm) as a function of season.

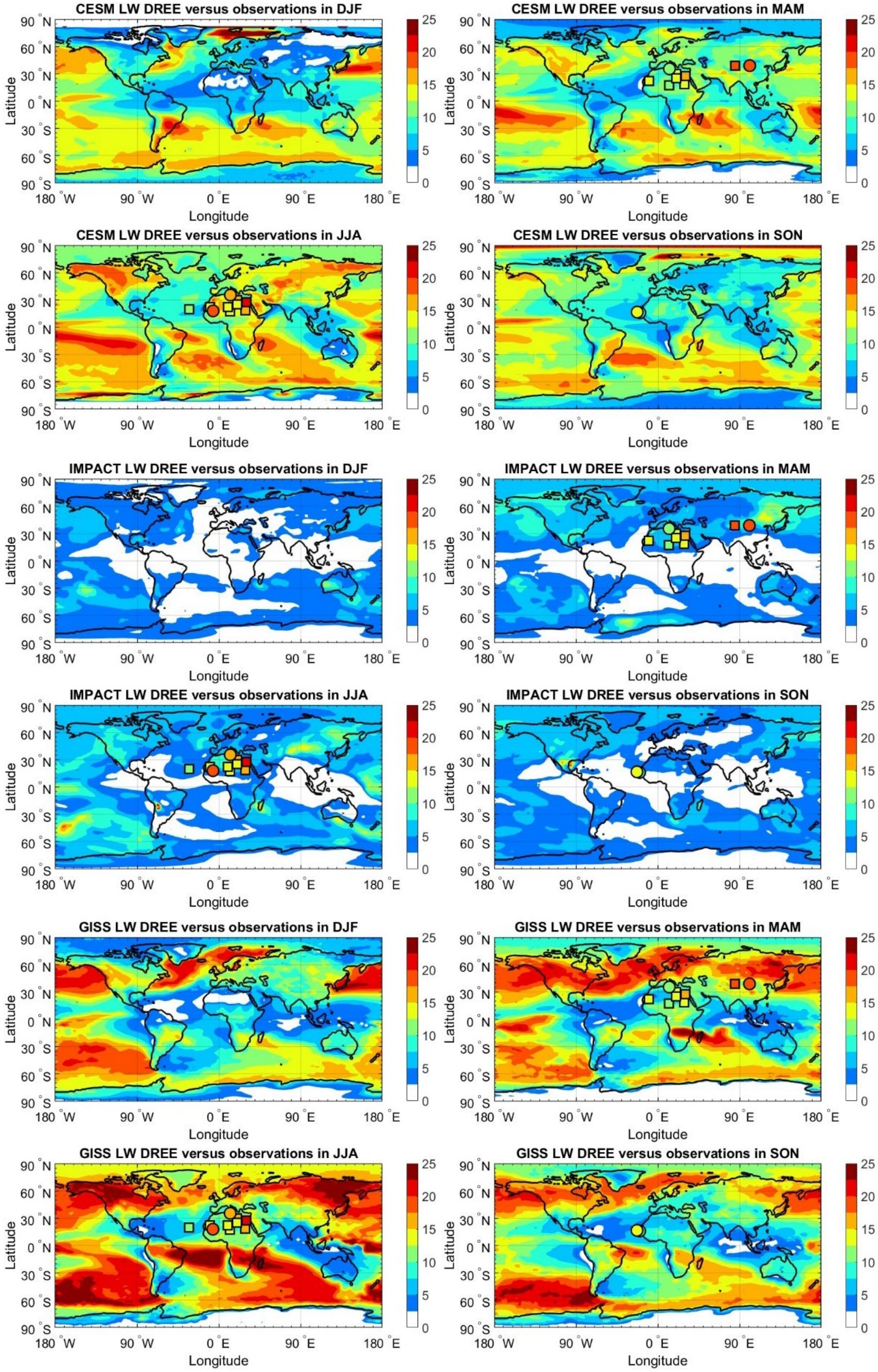
CESM LW DREE versus observations in DJF
CESM LW DREE versus observations in MAM
CESM LW DREE versus observations in JJA
CESM LW DREE versus observations in SON
IMPACT LW DREE versus observations in DJF
IMPACT LW DREE versus observations in MAM
IMPACT LW DREE versus observations in JJA
IMPACT LW DREE versus observations in SON
GISS LW DREE versus observations in DJF
GISS LW DREE versus observations in MAM
GISS LW DREE versus observations in JJA
GISS LW DREE versus observations in SON
Latitude
Longitude
90 °N
60 °N
30 °N
0 °N
30 °S
60 °S
90 °S
180 °W
90 °W
0 °E
90 °E
180 °E
0
5
10
15
20
25

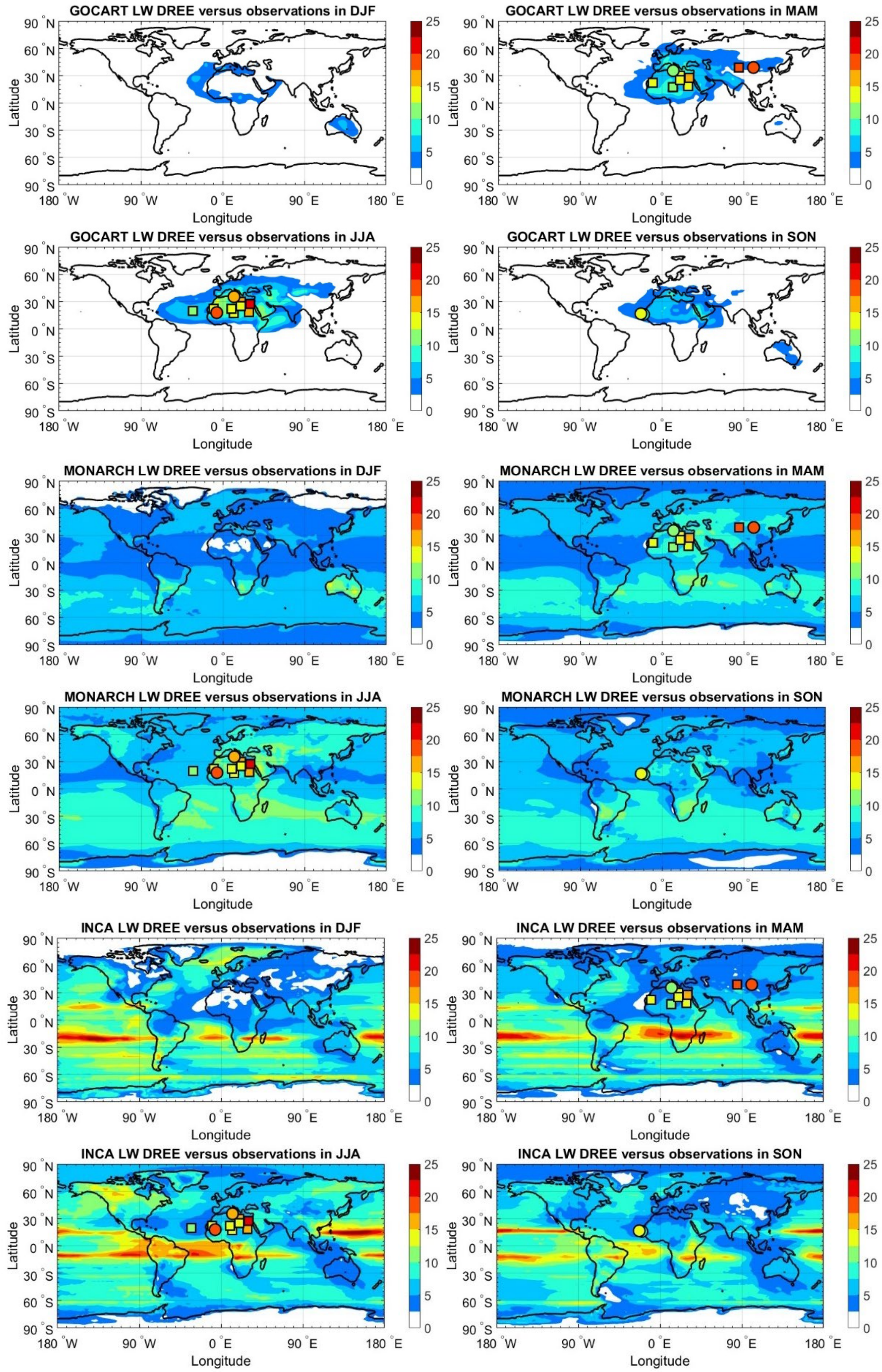
GOCART LW DREE versus observations in DJF
GOCART LW DREE versus observations in MAM
GOCART LW DREE versus observations in JJA
GOCART LW DREE versus observations in SON
MONARCH LW DREE versus observations in DJF
MONARCH LW DREE versus observations in MAM
MONARCH LW DREE versus observations in JJA
MONARCH LW DREE versus observations in SON
INCA LW DREE versus observations in DJF
INCA LW DREE versus observations in MAM
INCA LW DREE versus observations in JJA
INCA LW DREE versus observations in SON
Latitude
Longitude
90 °N
60 °N
30 °N
0 °N
30 °S
60 °S
90 °S
180 °W
90 °W
0 °E
90 °E
180 °E
25
20
15
10
5
0

Figure S14. Maps of simulated seasonal LW clear-sky DREE at TOA for each of the six models in our ensemble. Colored symbols denote observational estimates of LW clear-sky DREE at TOA derived mainly from in situ (circles) and satellite (squares) data.

References

1 Adebiyi, A. A. & Kok, J. F. Climate models miss most of the coarse dust in the atmosphere. *Science Advances* **6**, eaaz9507, doi:10.1126/sciadv.aaz9507 (2020).

2 Adebiyi, A. A. *et al.* Dust Constraints from joint Observational-Modelling-experiMental analysis (DustCOMM): comparison with measurements and model simulations. *Atmospheric Chemistry and Physics* **20**, 829-863, doi:10.5194/acp-20-829-2020 (2020).

3 Kok, J. F. *et al.* Improved representation of the global dust cycle using observational constraints on dust properties and abundance. *Atmospheric Chemistry and Physics* **21**, 8127-8167, doi:10.5194/acp-21-8127-2021 (2021).

4 Kok, J. F. *et al.* Contribution of the world's main dust source regions to the global cycle of desert dust. *Atmospheric Chemistry and Physics* **21**, 8169-8193, doi:10.5194/acp-21-8169-2021 (2021).

5 Kok, J. F. *et al.* Smaller desert dust cooling effect estimated from analysis of dust size and abundance. *Nature Geoscience* **10**, 274-278, doi:10.1038/ngeo2912 (2017).

6 Ridley, D. A., Heald, C. L., Kok, J. F. & Zhao, C. An observationally-constrained estimate of global dust aerosol optical depth. *Atmos. Chem. Phys.* **16**, 15097-15117, doi:10.5194/acp-2016-385 (2016).

7 Wilks, D. S. *Statistical Methods in the Amtospheric Sciences*. 3rd edn, (Academic Press, 2011).

8 Kim, D. *et al.* Sources, sinks, and transatlantic transport of North African dust aerosol: A multimodel analysis and comparison with remote sensing data. *Journal of Geophysical Research-Atmospheres* **119**, 6259-6277, doi:10.1002/2013jd021099 (2014).

9 Gelaro, R. *et al.* The Modern-Era Retrospective Analysis for Research and Applications, Version 2 (MERRA-2). *Journal of Climate* **30**, 5419-5454, doi:10.1175/jcli-d-16-0758.1 (2017).

10 Meng, J. *et al.* Improved Parameterization for the Size Distribution of Emitted Dust Aerosols Reduces Model Underestimation of Super Coarse Dust. *Geophysical Research Letters* **49**, doi:10.1029/2021gl097287 (2022).

11 Adebiyi, A. *et al.* A review of coarse mineral dust in the Earth system. *Aeolian Research* **60**, doi:10.1016/j.aeolia.2022.100849 (2023).

12 Di Biagio, C. *et al.* Global scale variability of the mineral dust long-wave refractive index: a new dataset of in situ measurements for climate modeling and remote sensing. *Atmospheric Chemistry and Physics* **17**, 1901-1929, doi:10.5194/acp-17-1901-2017 (2017).

13 Volz, F. E. Infrared refractive-index of atmospheric aerosol substances. *Applied Optics* **11**, 755-&, doi:10.1364/ao.11.000755 (1972).

14 Volz, F. E. Infrared optical-constants of ammonium sulfate, sahara dust, volcanic pumice, and flyash. *Applied Optics* **12**, 564-568, doi:10.1364/ao.12.000564 (1973).

15 Fouquart, Y. *et al.* Observations of saharan aerosols - results of eclats field experiment .2. Broad-band radiative characteristics of the aerosols and vertical radiative flux divergence. *Journal of climate and applied meteorology* **26**, 38-52 (1987).

16 Hess, M., Koepke, P. & Schult, I. Optical properties of aerosols and clouds: The software package OPAC. *Bulletin of the American Meteorological Society* **79**, 831-844, doi:10.1175/1520-0477(1998)079<0831:opoaac>2.0.co;2 (1998).

17 Di Biagio, C. *et al.* Variability of the infrared complex refractive index of African mineral dust: experimental estimation and implications for radiative transfer and satellite remote sensing. *Atmospheric Chemistry and Physics* **14**, 11093-11116, doi:10.5194/acp-14-11093-2014 (2014).
18 Fratini, G., Ciccioli, P., Febo, A., Forgione, A. & Valentini, R. Size-segregated fluxes of mineral dust from a desert area of northern China by eddy covariance. *Atmos. Chem. Phys.* **7**, 2839-2854 (2007).
19 Reid, J. S. *et al.* Dynamics of southwest Asian dust particle size characteristics with implications for global dust research. *Journal of Geophysical Research-Atmospheres* **113**, D14212, doi:10.1029/2007jd009752 (2008).
20 Kaaden, N. *et al.* State of mixing, shape factor, number size distribution, and hygroscopic growth of the Saharan anthropogenic and mineral dust aerosol at Tinfou, Morocco. *Tellus Ser. B-Chem. Phys. Meteorol.* **61**, 51-63, doi:10.1111/j.1600-0889.2008.00388.x (2009).
21 Sow, M., Alfaro, S. C., Rajot, J. L. & Marticorena, B. Size resolved dust emission fluxes measured in Niger during 3 dust storms of the AMMA experiment. *Atmos. Chem. Phys.* **9**, 3881-3891 (2009).
22 Huang, Y., Kok, J. F., Saito, M. & Munoz, O. Single-scattering properties of ellipsoidal dust aerosols constrained by measured dust shape distributions. *Atmospheric Chemistry and Physics* **23**, 2557-2577, doi:10.5194/acp-23-2557-2023 (2023).
23 Mayer, B. & Kylling, A. Technical note: The libRadtran software package for radiative transfer calculations - description and examples of use. *Atmospheric Chemistry and Physics* **5**, 1855-1877, doi:10.5194/acp-5-1855-2005 (2005).
24 Emde, C. *et al.* The libRadtran software package for radiative transfer calculations (version 2.0.1). *Geoscientific Model Development* **9**, 1647-1672, doi:10.5194/gmd-9-1647-2016 (2016).
25 Anderson, G., Clough, S., Kneizys, F., Chetwynd, J. & Shettle, E. AFGL atmospheric constituent profiles (0-120 km). (Air Force Geophys. Lab., Hanscom Air Force Base, Bedford, Mass., 1986).
26 Stamnes, K., Tsay, S.-C., Wiscombe, W. & Laszlo, I. DISORT, general-purpose Fortran program for discrete-ordinate-method radiative transfer in scattering and emitting layered media: documentation of methodology. (2000).
27 Gasteiger, J. *et al.* Representative wavelengths absorption parameterization applied to satellite channels and spectral bands. *Journal of Quantitative Spectroscopy & Radiative Transfer* **148**, 99-115, doi:10.1016/j.jqsrt.2014.06.024 (2014).
28 Efron, B. *The jackknife, the bootstrap, and other resampling plans*. (Capital City Press, 1982).
29 Chernick, M. R. *Bootstrap methods : a guide for practitioners and researchers*. 400 (Wiley-Interscience, 2007).
30 Neale, R. B. *et al.* Description of the NCAR Community Atmosphere Model (CAM 5.0). *NCAR Technical Note* **TN-486**, pp. 268 (2010).
31 Mahowald, N. M. *et al.* Change in atmospheric mineral aerosols in response to climate: Last glacial period, preindustrial, modern, and doubled carbon dioxide climates. *J. Geophys. Res.* **111**, D10202, doi:10.1029/2005jd006653 (2006).
32 Kok, J. F. A scaling theory for the size distribution of emitted dust aerosols suggests climate models underestimate the size of the global dust cycle. *Proc. Natl. Acad. Sci. U. S. A.* **108**, 1016-1021, doi:10.1073/pnas.1014798108 (2011).
33 Ramanathan, V. & Downey, P. A nonisothermal emissivity and absorptivity formulation for water-vapor. *Journal Of Geophysical Research-Atmospheres* **91**, 8649-8666 (1986).
34 Collins, W., Hackney, J. & Edwards, D. An updated parameterization for infrared emission and absorption by water vapor in the National Center for Atmospheric Research Community Atmosphere Model. *Journal of Geophysical Research-Atmospheres* **107**, doi:10.1029/2001JD001365 (2002).

35 Yoshioka, M. *et al.* Impact of desert dust radiative forcing on Sahel precipitation: Relative importance of dust compared to sea surface temperature variations, vegetation changes, and greenhouse gas warming. *Journal of Climate* **20**, 1445-1467, doi:10.1175/jcli4056.1 (2007).
36 Dufresne, J. L., Gautier, C., Ricchiazzi, P. & Fouquart, Y. Longwave scattering effects of mineral aerosols. *J. Atmos. Sci.* **59**, 1959-1966, doi:10.1175/1520-0469(2002)059<1959:lseoma>2.0.co;2 (2002).
37 Slingo, J. The development and verification of a cloud prediction scheme for the ECMWF model. *Quarterly Journal Of The Royal Meteorological Society* **113**, 899-927 (1987).
38 Klein, S. & Hartmann, D. The seasonal cycle of low stratiform clouds. *Journal of Climate* **6**, 1587-1606 (1993).
39 Xu, K. & Krueger, S. Evaluation of cloudiness parameterizations using a cumulus ensemble model. *Monthly Weather Review* **119**, 342-367 (1991).
40 Vavrus, S. & Waliser, D. An Improved Parametrization for Simulating Arctic Cloud Amount in the CCSM3 Climate Model. *Journal of Climate* **21**, 5673-5687, doi:10.1175/2008JCLI2299.1 (2008).
41 Ito, A., Ye, Y., Yamamoto, A., Watanabe, M. & Aita, M. N. Responses of ocean biogeochemistry to atmospheric supply of lithogenic and pyrogenic iron-containing aerosols. *Geological Magazine* **157**, 741-756, doi:10.1017/s0016756819001080 (2020).
42 Ito, A., Lin, G. X. & Penner, J. E. Radiative forcing by light-absorbing aerosols of pyrogenetic iron oxides. *Scientific Reports* **8**, doi:10.1038/s41598-018-25756-3 (2018).
43 Collins, W. D. *et al.* The Community Climate System Model version 3 (CCSM3). *Journal of Climate* **19**, 2122-2143 (2006).
44 Albani, S. *et al.* Improved dust representation in the Community Atmosphere Model. *J. Adv. Model. Earth Sy.* **6**, 541-570, doi:10.1002/2013ms000279 (2014).
45 Xu, L. & Penner, J. E. Global simulations of nitrate and ammonium aerosols and their radiative effects. *Atmospheric Chemistry and Physics* **12**, 9479-9504, doi:10.5194/acp-12-9479-2012 (2012).
46 Ito, A., Adebiyi, A. A., Huang, Y. & Kok, J. F. Less atmospheric radiative heating by dust due to the synergy of coarser size and aspherical shape. *Atmospheric Chemistry and Physics* **21**, 16869-16891, doi:10.5194/acp-21-16869-2021 (2021).
47 Bauer, S. E. *et al.* Historical (1850-2014) Aerosol Evolution and Role on Climate Forcing Using the GISS ModelE2.1 Contribution to CMIP6. *J. Adv. Model. Earth Syst.* **12**, doi:10.1029/2019ms001978 (2020).
48 Kelley, M. *et al.* GISS-E2.1: Configurations and climatology. *J. Adv. Model. Earth Syst.* **12**, e2019MS002025, doi:10.1029/2019MS002025 (2020).
49 Miller, R. L. *et al.* Mineral dust aerosols in the NASA Goddard Institute for Space Sciences ModelE atmospheric general circulation model. *J. Geophys. Res.-Atmos.* **111**, D06208, doi:10.1029/2005jd005796 (2006).
50 Perlwitz, J. P., Perez Garcia-Pando, C. & Miller, R. L. Predicting the mineral composition of dust aerosols - Part 1: Representing key processes. *Atmos. Chem. Phys.* **15**, 11593-11627 (2015).
51 Ginoux, P. *et al.* Sources and distributions of dust aerosols simulated with the GOCART model. *J. Geophys. Res.* **106**, 20255-20273 (2001).
52 Cakmur, R. V. *et al.* Constraining the magnitude of the global dust cycle by minimizing the difference between a model and observations. *Journal of Geophysical Research-Atmospheres* **111**, D06207, doi:10.1029/2005jd005791 (2006).
53 Cakmur, R. V., Miller, R. L. & Torres, O. Incorporating the effect of small-scale circulations upon dust emission in an atmospheric general circulation model. *Journal of Geophysical Research-Atmospheres* **109**, doi:10.1029/2003jd004067 (2004).

54 Bauer, S. E. & Koch, D. Impact of heterogeneous sulfate formation at mineral dust surfaces on aerosol loads and radiative forcing in the Goddard Institute for Space Studies general circulation model. *Journal of Geophysical Research-Atmospheres* **110**, doi:10.1029/2005jd005870 (2005).
55 Sinyuk, A., Torres, O. & Dubovik, O. Combined use of satellite and surface observations to infer the imaginary part of refractive index of Saharan dust. *Geophysical Research Letters* **30**, 1081, doi:10.1029/2002gl016189 (2003).
56 Patterson, E. M., Gillette, D. A. & Stockton, B. H. Complex index of refraction between 300 and 700 nm for saharan aerosols. *Journal of Geophysical Research-Oceans and Atmospheres* **82**, 3153-3160, doi:10.1029/JC082i021p03153 (1977).
57 Schmidt, G. A. *et al.* Present-day atmospheric simulations using GISS ModelE: Comparison to in situ, satellite, and reanalysis data. *Journal of Climate* **19**, 153-192, doi:10.1175/jcli3612.1 (2006).
58 Twomey, S. Influence of pollution on shortwave albedo of clouds. *J. Atmos. Sci.* **34**, 1149-1152 (1977).
59 Menon, S. & Rotstayn, L. The radiative influence of aerosol effects on liquid-phase cumulus and stratiform clouds based on sensitivity studies with two climate models. *Clim. Dyn.* **27**, 345-356, doi:10.1007/s00382-006-0139-3 (2006).
60 Miller, R. *et al.* CMIP6 Historical Simulations (1850-2014) With GISS-E2.1. *J. Adv. Model. Earth Syst.* **13**, doi:10.1029/2019MS002034 (2021).
61 Forster, P. *et al.* (eds V. Masson-Delmotte *et al.*) Ch. Chapter 7: The Earth's energy budget, climate feedbacks, and climate sensitivity, (2021).
62 DelGenio, A., Yao, M., Kovari, W. & Lo, K. A prognostic cloud water parameterization for global climate models. *Journal of Climate* **9**, 270-304 (1996).
63 DelGenio, A. D. & Yao, M.-S. in *The Representation of Cumulus Convection in Numerical Models AMS Meteorological Monograph* (eds K.A. Emanuel & D.A. Raymond) (American Meteorological Society, 1993).
64 Schmidt, G. *et al.* Configuration and assessment of the GISS ModelE2 contributions to the CMIP5 archive. *J. Adv. Model. Earth Syst.* **6**, 141-184, doi:10.1002/2013MS000265 (2014).
65 Hansen, J. *et al.* Efficient 3-dimensional global-models for climate studies - model-I and model-II. *Monthly Weather Review* **111**, 609-662, doi:10.1175/1520-0493(1983)111<0609:ETDGMF>2.0.CO;2 (1983).
66 Chin, M. *et al.* Tropospheric aerosol optical thickness from the GOCART model and comparisons with satellite and Sun photometer measurements. *J. Atmos. Sci.* **59**, 461-483, doi:10.1175/1520-0469(2002)059<0461:taotft>2.0.co;2 (2002).
67 Colarco, P., da Silva, A., Chin, M. & Diehl, T. Online simulations of global aerosol distributions in the NASA GEOS-4 model and comparisons to satellite and ground-based aerosol optical depth. *Journal of Geophysical Research-Atmospheres* **115**, doi:10.1029/2009jd012820 (2010).
68 Kok, J. F. Does the size distribution of mineral dust aerosols depend on the wind speed at emission? *Atmos. Chem. Phys.* **11**, 10149-10156, doi:10.5194/acp-11-10149-2011 (2011).
69 Colarco, P. R. *et al.* Impact of radiatively interactive dust aerosols in the NASA GEOS-5 climate model: Sensitivity to dust particle shape and refractive index. *Journal of Geophysical Research-Atmospheres* **119**, 753-786, doi:10.1002/2013jd020046 (2014).
70 Koepke, P., Hess, M., Schult, I. & Shettle, E. Global Aerosol Data Set. (Max Planck Institute for Meteorology, Hamburg, 1997).
71 Iacono, M. J. *et al.* Radiative forcing by long-lived greenhouse gases: Calculations with the AER radiative transfer models. *Journal of Geophysical Research-Atmospheres* **113**, doi:10.1029/2008jd009944 (2008).
72 Bacmeister, J., Suarez, M. & Robertson, F. Rain reevaporation, boundary layer-convection interactions, and Pacific rainfall patterns in an AGCM. *J. Atmos. Sci.* **63**, 3383-3403 (2006).

73 Molod, A. Constraints on the Profiles of Total Water PDF in AGCMs from AIRS and a High-Resolution Model. *JOURNAL OF CLIMATE* **25**, 8341-8352, doi:10.1175/JCLI-D-11-00412.1 (2012).
74 Molod, A., Takacs, L., Suarez, M. & Bacmeister, J. Development of the GEOS-5 atmospheric general circulation model: evolution from MERRA to MERRA2. *GEOSCIENTIFIC MODEL DEVELOPMENT* **8**, 1339-1356, doi:10.5194/gmd-8-1339-2015 (2015).
75 Pérez, C. *et al.* Atmospheric dust modeling from meso to global scales with the online NMMB/BSC-Dust model - Part 1: Model description, annual simulations and evaluation. *Atmospheric Chemistry and Physics* **11**, 13001-13027, doi:10.5194/acp-11-13001-2011 (2011).
76 Badia, A. *et al.* Description and evaluation of the Multiscale Online Nonhydrostatic AtmospheRe CHemistry model (NMMB-MONARCH) version 1.0: gas-phase chemistry at global scale. *Geoscientific Model Development* **10**, 609-638, doi:10.5194/gmd-10-609-2017 (2017).
77 Klose, M. *et al.* Mineral dust cycle in the Multiscale Online Nonhydrostatic AtmospheRe CHemistry model (MONARCH) Version 2.0. *Geoscientific Model Development* **14**, 6403-6444, doi:10.5194/gmd-14-6403-2021 (2021).
78 Janjic, Z. & Gall, R. Scientific documentation of the NCEP Nonhydrostatic Multiscale Model on the B grid (NMMB). (National Center for Atmospheric Research, Camp Springs, MD, USA., 2012).
79 Hu, Y. & Stamnes, K. An accurate parameterization of the radiative properties of water clouds suitable for use in climate models. *Journal of Climate* **6**, 728-742 (1993).
80 Fu, Q., Yang, P. & Sun, W. An accurate parameterization of the infrared radiative properties of cirrus clouds for climate models. *Journal of Climate* **11**, 2223-2237 (1998).
81 Di Biagio, C., Balkanski, Y., Albani, S., Boucher, O. & Formenti, P. Direct Radiative Effect by Mineral Dust Aerosols Constrained by New Microphysical and Spectral Optical Data. *Geophysical Research Letters* **47**, doi:10.1029/2019gl086186 (2020).
82 Checa-Garcia, R. *et al.* Evaluation of natural aerosols in CRESCENDO Earth system models (ESMs): mineral dust. *Atmospheric Chemistry and Physics* **21**, 10295-10335, doi:10.5194/acp-21-10295-2021 (2021).
83 Ryder, C. L. *et al.* Optical properties of Saharan dust aerosol and contribution from the coarse mode as measured during the Fennec 2011 aircraft campaign. *Atmospheric Chemistry and Physics* **13**, 303-325, doi:10.5194/acp-13-303-2013 (2013).
84 Morcrette, J.-J., Clough, S. A., Mlawer, E. J. & Iacono, M. J. Impact of a validated radiative transfer scheme, RRTM, on the ECMWF model climate and 10-day forecasts. (ECMWF, Shinfield Park, Reading, 1998).
85 Boucher, O. *et al.* Presentation and Evaluation of the IPSL-CM6A-LR Climate Model. *J. Adv. Model. Earth Syst.* **12**, doi:10.1029/2019ms002010 (2020).
86 Hourdin, F. *et al.* LMDZ6A: The Atmospheric Component of the IPSL Climate Model With Improved and Better Tuned Physics. *J. Adv. Model. Earth Syst.* **12**, doi:10.1029/2019MS001892 (2020).
87 Bony, S. & Emanuel, K. A parameterization of the cloudiness associated with cumulus convection; Evaluation using TOGA COARE data. *J. Atmos. Sci.* **58**, 3158-3183 (2001).
88 Jam, A., Hourdin, F., Rio, C. & Couvreux, F. Resolved Versus Parametrized Boundary-Layer Plumes. Part III: Derivation of a Statistical Scheme for Cumulus Clouds. *Boundary-Layer Meteorology* **147**, 421-441, doi:10.1007/s10546-012-9789-3 (2013).
89 Brindley, H. E. & Russell, J. E. An assessment of Saharan dust loading and the corresponding cloud-free longwave direct radiative effect from geostationary satellite observations. *Journal of Geophysical Research-Atmospheres* **114**, doi:10.1029/2008jd011635 (2009).
90 Yang, E. S., Gupta, P. & Christopher, S. A. Net radiative effect of dust aerosols from satellite measurements over Sahara. *Geophysical Research Letters* **36**, L18812, doi:10.1029/2009gl039801 (2009).

91 Xia, X. & Zong, X. Shortwave versus longwave direct radiative forcing by Taklimakan dust aerosols. *Geophysical Research Letters* **36**, doi:10.1029/2009GL037237 (2009).
92 Haywood, J. *et al.* Can desert dust explain the outgoing longwave radiation anomaly over the Sahara during July 2003? *Journal of Geophysical Research-Atmospheres* **110**, doi:10.1029/2004JD005232 (2005).
93 Liou, K. N. *An Introduction to Atmospheric Radiation*. Second edn, (Academic Press, 2002).
94 Lee, L. A., Reddington, C. L. & Carslaw, K. S. On the relationship between aerosol model uncertainty and radiative forcing uncertainty. *Proc. Natl. Acad. Sci. U. S. A.* **113**, 5820-5827, doi:10.1073/pnas.1507050113 (2016).
95 Zhang, Z., Song, Q., Zheng, J. & Yu, H. Effects of surface coating on the shortwave and longwave radiative effects of dust aerosol in comparison with external mixing: A theoretical study. *Journal of Quantitative Spectroscopy & Radiative Transfer* **324**, doi:10.1016/j.jqsrt.2024.109060 (2024).
96 Li , W. *et al.* Aqueous-phase secondary organic aerosol formation on mineral dust. *National Science Review*, nwaf221, doi:10.1093/nsr/nwaf221 (2025).
97 Kok, J. F. *et al.* Mineral dust aerosol impacts on global climate and climate change. *Nature Reviews Earth & Environment* **4**, 71–86, doi:10.1038/s43017-022-00379-5 (2023).
98 O'Sullivan, D. *et al.* Models transport Saharan dust too low in the atmosphere: a comparison of the MetUM and CAMS forecasts with observations. *Atmospheric Chemistry and Physics* **20**, 12955-12982, doi:10.5194/acp-20-12955-2020 (2020).
99 Gill, T. E., Zobeck, T. M. & Stout, J. E. Technologies for laboratory generation of dust from geological materials. *Journal of Hazardous Materials* **132**, 1-13, doi:10.1016/j.jhazmat.2005.11.083 (2006).
100 Osborne, S. *et al.* Short-wave and long-wave radiative properties of Saharan dust aerosol. *Quarterly Journal of the Royal Meteorological Society* **137**, 1149-1167, doi:10.1002/qj.771 (2011).
101 Heald, C. L. *et al.* Contrasting the direct radiative effect and direct radiative forcing of aerosols. *Atmos. Chem. Phys.* **14**, 5513-5527, doi:10.5194/acp-14-5513-2014 (2014).
102 Scanza, R. *et al.* Modeling dust as component minerals in the Community Atmosphere Model: development of framework and impact on radiative forcing. *Atmos. Chem. Phys.* **15**, 537-561 (2015).
103 Klingmuller, K., Lelieveld, J., Karydis, V. A. & Stenchikov, G. L. Direct radiative effect of dust-pollution interactions. *Atmospheric Chemistry and Physics* **19**, 7397-7408, doi:10.5194/acp-19-7397-2019 (2019).
104 Tuccella, P., Curci, G., Pitari, G., Lee, S. & Jo, D. S. Direct Radiative Effect of Absorbing Aerosols: Sensitivity to Mixing State, Brown Carbon, and Soil Dust Refractive Index and Shape. *Journal of Geophysical Research-Atmospheres* **125**, doi:10.1029/2019jd030967 (2020).
105 Li, L. L. *et al.* Quantifying the range of the dust direct radiative effect due to source mineralogy uncertainty. *Atmospheric Chemistry and Physics* **21**, 3973-4005, doi:10.5194/acp-21-3973-2021 (2021).
106 Feng, Y. *et al.* Global Dust Cycle and Direct Radiative Effect in E3SM Version 1: Impact of Increasing Model Resolution. *J. Adv. Model. Earth Syst.* **14**, doi:10.1029/2021MS002909 (2022).
107 Ke, Z., Liu, X., Wu, M., Shan, Y. & Shi, Y. Improved Dust Representation and Impacts on Dust Transport and Radiative Effect in CAM5. *J. Adv. Model. Earth Syst.* **14**, doi:10.1029/2021MS002845 (2022).
108 Wang, H. *et al.* Larger Dust Cooling Effect Estimated From Regionally Dependent Refractive Indices. *Geophysical Research Letters* **51**, doi:10.1029/2023GL107647 (2024).

109 Haywood, J. *et al.* Radiative properties and direct radiative effect of Saharan dust measured by the C-130 aircraft during SHADE: 1. Solar spectrum. *Journal of Geophysical Research-Atmospheres* **108**, doi:10.1029/2002jd002687 (2003).
110 Hansell, R. *et al.* An Assessment of the Surface Longwave Direct Radiative Effect of Airborne Saharan Dust during the NAMMA Field Campaign. *J. Atmos. Sci.* **67**, 1048-1065, doi:10.1175/2009JAS3257.1 (2010).
111 Hansell, R. *et al.* An assessment of the surface longwave direct radiative effect of airborne dust in Zhangye, China, during the Asian Monsoon Years field experiment (2008). *Journal of Geophysical Research-Atmospheres* **117**, doi:10.1029/2011JD017370 (2012).
112 di Sarra, A. *et al.* Shortwave and longwave radiative effects of the intense Saharan dust event of 25-26 March 2010 at Lampedusa (Mediterranean Sea). *Journal of Geophysical Research-Atmospheres* **116**, doi:10.1029/2011JD016238 (2011).
113 Meloni, D. *et al.* Altitude-resolved shortwave and longwave radiative effects of desert dust in the Mediterranean during the GAMARF campaign: Indications of a net daily cooling in the dust layer. *Journal of Geophysical Research-Atmospheres* **120**, 3386-3407, doi:10.1002/2014JD022312 (2015).
114 Meloni, D. *et al.* Determining the infrared radiative effects of Saharan dust: a radiative transfer modelling study based on vertically resolved measurements at Lampedusa. *Atmospheric Chemistry and Physics* **18**, 4377-4401, doi:10.5194/acp-18-4377-2018 (2018).
115 Song, Q. Q. *et al.* Net radiative effects of dust in the tropical North Atlantic based on integrated satellite observations and in situ measurements. *Atmospheric Chemistry and Physics* **18**, 11303-11322, doi:10.5194/acp-18-11303-2018 (2018).